2014

Ice-water dynamics over a land-terminating sector of western Greenland

Toby Meierbachtol
The University of Montana

Recommended Citation

Meierbachtol, Toby, "Ice-water dynamics over a land-terminating sector of western Greenland" (2014). *Graduate Student Theses, Dissertations, & Professional Papers*. 4409.
https://scholarworks.umt.edu/etd/4409

ICE-WATER DYNAMICS OVER A LAND-TERMINATING SECTOR OF WESTERN GREENLAND

By

TOBY WARREN MEIERBACHTOL

Master of Science, Geosciences, University of Montana, Missoula, MT, 2007
Bachelor of Arts, Geology, Whitman College, Walla Walla, WA, 2003

Dissertation

presented in partial fulfillment of the requirements
for the degree of

Doctor of Philosophy
in Geosciences

The University of Montana
Missoula, MT

July, 2014

Approved by:

Sandy Ross, Dean of The Graduate School
Graduate School

Dr. Joel T. Harper, Chair
Department of Geosciences

Dr. Jesse V. Johnson
Department of Computer Science

Dr. William Woessner
Department of Geosciences

Dr. Marco Maneta
Department of Geosciences

Dr. Neil F. Humphrey
Department of Geology and Geophysics, The University of Wyoming

Meierbachtol, Toby, PhD, Summer 2014 *Geosciences*

Ice Dynamics over a Land-Terminating Sector of Western Greenland

Chairperson: Dr. Joel T. Harper

In this dissertation I investigate the dynamics of a land-terminating reach of the west Greenland ice sheet through three projects utilizing unique field data and modeling experiments.

In Chapter 1 I use in-situ water pressure data and numerical modeling to elucidate the conceptual model of subglacial hydrologic drainage beneath Greenland. Measurements in boreholes drilled to the ice sheet bed along a transect in the ablation zone reveal water pressures that question the stability of water-draining conduits. I apply numerical techniques to model transient evolution of subglacial conduits and show that seasonal growth of such features is unsupported in the ice sheet interior. Low potential gradients that drive energy availability to melt channel walls limit conduit growth. This elucidates the importance of other processes in facilitating seasonal development of the subglacial hydrologic system in the interior setting.

In Chapter 2 I investigate the effect of thermal boundary conditions on the thermo-mechanical state of western Greenland. I propose new boundary fields from measurements of temperature near the surface and basal heat flux beneath the ice sheet. Comparison of these observation-based fields with model-driven datasets suggests that model-derived basal heat flux is too high, and surface temperatures too low in the study area. By applying different boundary conditions to a thermo-mechanically coupled ice sheet model I show that thermal conditions at the ice/bedrock interface critically depend on the boundary conditions at both the surface and bed. Unrealistically cold conditions are induced if basal heat flux alone is driven by observations. Warmer surface conditions consistent with observations are sufficient to reintroduce melted conditions at the bed, elucidating the importance of the surface boundary in thermo-mechanical model exploration.

In Chapter 3 I address the processes responsible for inducing a region of anomalously low driving stress that is evident in west-southwest Greenland. I show that the feature corresponds to a consistent reduction in surface slope rather than a strong bedrock topographic expression. Kinematic wave experiments show that the diffusive nature of the ice sheet renders the development of such a feature infeasible from surface mass balance perturbations. Low driving stress necessitates a change in dynamics and I surmise it is this variation in basal sliding that is an important factor in inducing changes in the surface slope, and thus the driving stress.

TABLE OF CONTENTS

Chapter 1: Basal drainage system response to increasing surface melt on the Greenland Ice Sheet

Chapter 2: Impact of field-constrained boundary conditions on western Greenland's thermo-mechanical state

TABLE OF CONTENTS

Chapter 3: Dynamical controls on the driving stress anomaly in west-southwest Greenland

Appendix A: Borehole impulse test experiments

LIST OF FIGURES

Chapter 1

LIST OF FIGURES

Chapter 2

LIST OF FIGURES

LIST OF FIGURES

Chapter 3

LIST OF FIGURES

Appendix A

generally following expected background trends indicate an inability of the system to accommodate the added perturbation.

LIST OF TABLES

Chapter 1

Appendix

ACKNOWLEDGEMENTS

I am indebted to many who contributed expertise, time, energy, and support in various contexts during these past five years. My advisor, Dr. Joel Harper, has invested countless hours listening, collaborating, editing, and providing guidance as I’ve wandered the circuitous route that is a PhD. I am extremely grateful for his open-door policy and careful advising. Without Dr. Neil Humphrey’s experience and expertise our successful field campaigns would no doubt have been compromised. Dr. Jesse Johnson provided valuable insight in to numerical model development and troubleshooting, and has always been generous with his time for even non-glaciological discussions. The support of my friends and family has been critical and seen me through many dark days. My mom, dad, Elie, and Becca have always been willing scratching posts when I need an ear. Trail talk with Ed has been crucial to maintaining sanity at times. In the waning weeks of my dissertation Emerson provided some much needed calm. There’s just something about the innocence of a newborn. Sophie’s companionship has proved that dogs really are man’s best friend. Finally, and most importantly, my fiancée Heidi has been unwavering in her support and flexible in times of crisis. She has reminded me to stay grounded and always leads by example.

INTRODUCTION TO THE DISSERTATION

Until recently, general scientific consensus was that the vast spatial dimension of the Greenland Ice Sheet limited its response time to millennia, in contrast to the smaller mountain counterpart [*Truffer and Fahnestock,* 2007]. However, the past decade of research has invoked a paradigm shift with respect to Greenland's behavior and response to external forcings. The ice sheet displays accelerations on time scales as short as diurnal [*Hoffman et al.*, 2011; *Bartholomew et al.*, 2012], velocity increases propagate >100 km from the ice sheet edge [*Palmer et al.*, 2011], and marine termini can exhibit kilometer-scale changes in position over just a few years [*Howat et al.*, 2007; *Joughin et al.*, 2010]. The global implications of Greenland's behavior in response to a changing climate provide motivation for many a research article.

Less publicized, however, has been the importance of process-level developments in understanding to directly inform design decisions for long-lifespan (several hundreds of thousands of years) structures in locations susceptible to glaciation. This is of immediate significance in the northern latitude countries of Sweden, Finland, and Canada, who are responsibly planning for the long term disposal of radiotoxic material in their respective countries in deep geological repositories. Each of the aforementioned countries have experienced glaciation events over historical timescales and are designing deep geological repositories for spent nuclear fuel under the assumption that future glaciation events are likely over the time scales relevant for waste decay. As such, the impact of glaciation on the conditions surrounding the repository is of importance in considering structure integrity and contaminant transport during the design process.

Specifically, perturbations at the ice-bedrock boundary that affect the groundwater flow field and chemistry are of critical importance. In the absence of ice sheet conditions at the repository sites, Greenland provides an ideal present-day analogue to study conditions relevant to plausible future scenarios in these high-latitude countries. Transfer of processes in the Greenland setting help to reduce uncertainties and provide a stronger scientific basis for the treatment of glacial impacts on safety assessments at the repository sites [*SKB*, 2011; *NWMO*, 2012; *Posiva*, 2012].

The presence of basal water, configuration of the drainage system and pressure at which it flows have a strong influence on the ice-bedrock boundary that drives groundwater dynamics. The presence of basal water depends on the thermal regime at the bed, and hence ice temperature. Ice temperature is controlled by ice flow dynamics and conditions at/near the surface. Clearly, a holistic understanding of ice sheet processes is necessary in order to adequately constrain processes occurring at the bottom of the ice sheet and conceptualize them in such a way to inform idealized future scenarios.

In Greenland, observational constraints on the basal character and flow dynamics of the ice sheet are limited. To elucidate the structure and evolution of the subglacial hydrologic network, and the role that water plays in dictating ice dynamics in the Greenland setting, a team from the University of Montana and University Wyoming carried out annual field campaigns from 2010 – 2013. This field work formed a significant component of my dissertation research through which our team gathered water pressure, ice temperature, and surface velocity data. We collected in-situ data in boreholes which we drilled to the ice sheet bed using hot water techniques. Over the course of three seasons we drilled a cumulative total of 10 km spread across multiple drilling sites in ice up to 820 m thick. Immersion in the field provided perspective, sparked ideas, and allowed me to place data in a physical context. Thus, the field work heavily shaped the research that follows here by yielding unique data, and also by providing a sense of place and scale within which to frame my thinking.

In my dissertation I elucidate the dynamics of a land-terminating reach of western Greenland in three chapters. Because sub-, en-, and supraglacial ice sheet processes are tightly coupled, the chapters encompass work focused on the ice sheet bed, within the ice mass, and at the ice surface. Each chapter has either been published, is in review, or is in an advanced state formatted for publication.

In Chapter 1 I utilize water pressure measurements in boreholes and numerical modeling to investigate the stability of water draining conduits and propose amendments to our conceptual model of subglacial drainage through the ice sheet ablation zone. Chapter 1 has been published in Science (doi: 10.1126/science.1235905). In Chapter 2 I leverage measurements of ice temperature and basal heat flux to constrain surface and bed thermal boundary conditions by observation. I then compare these data-based fields with commonly used boundary conditions and investigate the impact of the discrepancy on the thermo-mechanical state of western Greenland from a thermo-mechanically coupled ice sheet model. Chapter 2 has been submitted to the Journal of Geophysical Research: Earth Surface, and is currently in review. In Chapter 3, I investigate processes influencing a region of anomalous driving stress in western Greenland. Driving stress is a first-order driver of ice flow dynamics. Through kinematic wave experiments I investigate the plausibility that the anomaly results from surface mass balance perturbations. I also assess the likely partitioning of ice deformation and sliding to infer longitudinal gradients in basal motion, and their role in development of the driving stress anomaly. It is formatted for submission to The Journal of Glaciology.

I have also included, as an Appendix, developing work from in-situ stress testing of the subglacial hydrological system which I term ‘impulse tests’. This work is currently under analysis and will benefit from additional testing which will build and strengthen the overall dataset. I plan to perform more impulse tests in additional Greenland field campaigns starting in July, 2014.

In addition to the work presented in these three chapters I have been fortunately involved in additional research that has resulted in publication during my tenure as a doctoral student. These publications developed from additional ice sheet modeling research on Greenland, as well as from field work performed on Bench Glacier, Alaska. The publications include:

Brinkerhoff, D J, Meierbachtol, T W, Johnson, J V, Harper, J T. 2011. Sensitivity of the frozen/melted basal boundary to perturbations of basal traction and geothermal heat flux: Isunnguata Sermia, western Greenland. *Annals of Glaciology*, **52**(59), 43-50.

Harper, J T, Bradford, J H, Humphrey, N F, Meierbachtol, T W. 2010. Vertical extension of the subglacial drainage system into basal crevasses. *Nature*, **467**(7315), 579-582.

Bradford, J H, Nichols, J, Harper, J T, Meierbachtol, T. 2013. Compressional and EM wave anisotropy in a temperate glacier due to basal crevasses, and implications for water content estimation. *Annals of Glaciology*, **54**(64), 168-178.

References

Bartholomew, I., P. Nienow, A. Sole, D. Mair, T. Cowton, and M. a. King (2012), Short-term variability in Greenland Ice Sheet motion forced by time-varying meltwater drainage: Implications for the relationship between subglacial drainage system behavior and ice velocity, *J. Geophys. Res.*, *117*(F3), 1–17, doi:10.1029/2011JF002220.

Hoffman, M. J., G. A. Catania, T. A. Neumann, L. C. Andrews, and J. A. Rumrill (2011), Links between acceleration, melting, and supraglacial lake drainage of the western Greenland Ice Sheet, *J. Geophys. Res.*, *116*(F4), 1–16, doi:10.1029/2010JF001934.

Howat, I. M., I. Joughin, and T. a Scambos (2007), Rapid changes in ice discharge from Greenland outlet glaciers., *Science*, *315*(5818), 1559–61, doi:10.1126/science.1138478.

Joughin, I., B. E. Smith, I. M. Howat, T. Scambos, and T. Moon (2010), Greenland flow variability from ice-sheet-wide velocity mapping, *J. Glaciol.*, *56*(197), 415–430, doi:10.3189/002214310792447734.

NWMO (2012), *Adaptive Phase Management - Used fuel repository conceptual design and postclosure safety assessment in crystalline rock. Pre-project report: NWMO-TR-12-16.*

Palmer, S., A. Shepherd, P. Nienow, and I. Joughin (2011), Seasonal speedup of the Greenland Ice Sheet linked to routing of surface water, *Earth Planet. Sci. Lett.*, *302*(3-4), 423–428, doi:10.1016/j.epsl.2010.12.037.

Posiva (2012), *Safety case for the disposal of spent nuclear fuel at Olkiluoto - Formulation of Radionuclide Release Scenarios 2012. Eurajoki, Finland: Posiva Oy. POSIVA 2012-08.*

SKB (2011), *Long-term safety for the final repository for spent nuclear fuel at Forsmark. Main report of the SR-Site project. SKB TR-11-01, Svensk Karnbranslehantering AB.*

Truffer, M., and M. Fahnestock (2007), Climate change. Rethinking ice sheet time scales., *Science*, *315*(5818), 1508–10, doi:10.1126/science.1140469.

CHAPTER 1

BASAL DRAINAGE SYSTEM RESPONSE TO INCREASING SURFACE MELT ON THE GREENLAND ICE SHEET

Abstract:

Surface melt water reaching the bed of the Greenland ice sheet imparts a fundamental control on basal motion. Sliding speed depends on ice/bed coupling dictated by the configuration and pressure of the hydrologic drainage system. In-situ observations in a four-site transect containing 23 boreholes drilled to Greenland's bed reveal basal water pressures unfavorable to water-draining conduit development extending inland beneath deep ice. This finding is supported by numerical analysis based on realistic ice sheet geometry. Slow melt-back of ice walls limits conduit growth, inhibiting their capacity to transport increased discharge. Key aspects of current conceptual models for Greenland basal hydrology, derived primarily from study of mountain glaciers, appear bounded to a portion of the ablation zone near the ice sheet margin.

Main Text:

Measurements on the Greenland ice sheet (GrIS) show widespread meltwater forcing on velocity, impacting marine (*1*, *2*) and terrestrially terminating regions (*2–10*) many tens of kilometers inland from the margin (*4*, *5*, *10*). During the summer melt season, velocities commonly increase up to 100% or more above winter averages (*2*, *3*, *5–10*), and can exceed 300% (*4*, *10*). However, future response of the ice sheet to enhanced surface melt intensity, longer melt seasons, extended melt zones, and increasing high-melt or rainfall events is unclear with apparently conflicting possibilities. Positive feedbacks may be limited as observations show velocity peaks in the melt season, and diminishes later in the summer while ablation increases (*3*, *10*). Further, years with high ablation display smaller average seasonal speed-ups near the ice sheet margin (*6*). Alternatively, longer surface melt seasons in a warmer climate enhance ice sheet motion due to more short term accelerations from melt pulses repeatedly overwhelming the subglacial system (*4*, *11*). The nature of changes in sliding motion impact sea level by dictating the extent to which ice is drawn to lower elevations where melt rates are high and ice is discharged through calving termini.

The degree to which meltwater input influences sliding dynamics is driven by the disparity between the rate-of-change of water input and the capacity of the subglacial drainage network (*4*, *11*, *12*). Observations on the GrIS show the basal network evolves through the melt season, with enhanced efficiency extending upwards of 50 km inland from the ice sheet margin (*13*, *14*). The mechanism driving evolution is commonly interpreted to follow the smaller mountain glacier conceptual model, whereby an inefficient network of linked cavities switches to a system of efficient channels by melting of the overlying ice roof. The sensitivity to sustained meltwater input is reduced as the inefficient network evolves to a high capacity channelized system, but short term perturbations still overwhelm even these efficient drainage features. Basal pressure measurements, which are restricted in time and space (*15–18*), and dye tracing experiments along the ablation zone (*14*) provide the only direct measurements of subglacial hydrologic conditions to date. Whereas basal pressure observations have proven indispensable for elucidating hydrologic processes in the mountain glacier setting, scarce observational datasets from the GrIS so far limit extension of these processes to the ice sheet scale with confidence. Here, using in-situ water pressure measurements in boreholes drilled along a 34 km transect in western GrIS and modeling, we test the hypothesis that basal conduit melt processes drive formation of a channelized network across the drainage regime.

During the summers of 2010 – 2012 we used hot water methods to drill 23 boreholes to the ice sheet bed at sites along an E-W transect in western Greenland (Fig. 1). Borehole sites extend inland from the margin of terrestrially terminating Isunnguata Sermia, and represent a range of settings from shallow marginal conditions with 100-150 m ice depth (hereafter referred to as S1) to 34 km deep in the interior where ice thickness is >800 m (S4) (*19*). Sites also sample a bedrock trough (S3) and adjacent shallow area located 17 km inland (S2). Prior to borehole refreezing, we performed hydrological impulse tests (*19*), and instrumented boreholes with basal water pressure sensors for long term (up to >1 year) monitoring.

We measured distinctive spatial variability in borehole water pressure behavior at the ice sheet margin (S1) compared to deeper in the interior (S2 – S4). Of the 13 holes drilled at S1, six immediately connected to the active subglacial system as evidenced by rapid water level drops when the drill intersected the bed (Fig. S1). Basal water pressures in these holes suggest a mix of distributed and channelized drainage during the summer melt season. Daily water pressure swings exceeding 70% of ice overburden (OB) (Fig. 2) indicate borehole connection to a highly efficient, channelized system (*20*). In other holes, small-amplitude variations superimposed on steady high pressure suggest limited drainage capacity (Fig. 2), which is corroborated by the slow accommodation of water introduced to holes during impulse testing. Similar variability over high mean pressures has been interpreted to reflect a distributed drainage configuration (*21*, *22*).

All 10 boreholes located 17 – 34 km from the margin experienced 50 – 125 m water level drops (12 – 17% OB equivalent (Fig. S1)) when the drill intersected the bed, indicating connection to an active drainage system. At S2 and S4, pressure records are similar to those boreholes near the ice sheet edge interpreted to be connected to a linked cavity network. Water pressures 34 km inland at S4 remained between 88 – 94% OB during the late melt season (day-of-year 200-240) with diurnal variations limited to 4% OB or less. Pressures at S2 were steadily between 82 – 92% OB with small variations of similar magnitude as S4 (Fig. 2). In the adjacent trough (S3), hydraulic connections between boreholes were evident over 20 m length scales, but long term connectivity to a broader drainage system appears to be transient. Water level behavior at S3 periodically switched from steadily near or above 100% OB, to exhibiting diurnal variations up to 14% OB. We interpret this behavior to reflect temporary establishment and loss of connections along the bed.

Consistent with existing observations to the north near Jakobshavn Isbræ (*17*, *18*), we see no direct evidence of high capacity basal melt channels in our inland (17 and 34 km from the ice sheet margin) boreholes as manifested by reduced mean pressures and large amplitude diurnal pressure variations. However, limited sample locations do not preclude the existence of such basal pathways, motivating comparison of basal pressure conditions through numerical analysis. Following previous theoretical development of steady state conduit dynamics (*23*), we model conduit conditions on the ice sheet domain under a range of constant discharge values (*19*). We find that steady conduit pressures less than 70% OB are limited to <10 km from the margin and increase towards overburden further inland (Fig. 3). Near the ice sheet margin, expected conduit pressures lower than our distributed measurements reinforce previous theory that water is driven in to these low pressure features, enhancing their stability (*11*). The reverse is true away from the margin. Pressure differentials between our inland measurements and conduit theory are diminished, and measured pressures at S4 are lower than expected in conduits. In this interior setting, water driven away from high pressure conduits would feed the distributed network represented by our measurements, resulting in conduit instability and collapse.

Steady state analysis neglects variable input as surface melt water routed to the bed through discrete moulins undergoes seasonal (*24*) and diurnal (*25*) change. We therefore extend analysis to include transient forcing by implementing a conduit melt-closure model (*19*). Creep closure from ice deformation and opening from melt-back of conduit walls determine cross-sectional area, and turbulent flow is simulated through the semi-circular conduit. We focus here on two test cases representing a conduit near the margin (3 km length) and extending to the drainage interior (40 km) to illustrate geometric effects on conduit growth via melting. We assume a pre-existing conduit and force the system with diurnally varying discharge. Melt-back of the ice walls near the ice sheet margin promotes basal conduit growth (Fig. 3) so that changes in input are rapidly accommodated, thereby preventing elevated pressures. In contrast, interior conduit melt rates are >95% slower than creep closure. Stunted conduit geometry from slow growth can only accommodate a fraction of the imposed input and at pressures largely constrained to 100% OB. The imposed input range (1–3 $m^3 s^{-1}$) requires a period of variation that is unreasonably long (90 days) to be fully accommodated by the conduit (supplementary online text).

Enhanced conduit closure under thicker ice has been highlighted as a driving difference between alpine and ice sheet subglacial hydraulics (*10*, *12*). However, our pressure records imply maximum closure rates are similar at marginal sites and in the interior. This is supported by our numerical test cases despite ice thickness at the inland setting that is 3x the margin. Instead, low basal conduit melt rates limit channel evolution at inland areas of the ice sheet. Melting of conduit walls is a function of discharge and hydraulic gradient. Steep surface slopes are common in both alpine glaciers and near the ice sheet margin, leading to large hydraulic gradients at the glacier bed and hence high basal conduit melt rates. In contrast, much of the ice sheet ablation zone away from the margin is characterized by muted surface slopes which limit conduit growth through dissipative heating effects.

Asymmetry between conduit melt-back and closure rates dictates that basal conduits can only be sustained by generally steady discharge conditions. Despite variable surface input, it is possible that modulation of discharge through basal or englacial water storage and release could facilitate near-steady basal flow. Other work suggests reversing hydraulic gradients enable an adjacent network to temporarily store water driven out of conduits during periods of high flux, and return it during times of low flow (*20*, *26*). However, that model assumes preexisting basal conduits. Our results suggest basal melt rates are too slow to fully establish a channelized network during a single summer season (supplementary online text). Further, our measurements of the basal pressure regime question interior conduit stability under steady flow conditions.

Our data and numerical experiments do not support widespread growth of a conduit network in the drainage interior by ice-wall melt processes alone. Nevertheless, velocity interpretations (*10*), proglacial stream measurements (*13*), and dye tracing experiments (*14*) provide evidence for seasonally increasing drainage efficiency away from the margin. This implies other physical processes at the bed are more important than previously recognized in regions where gradient-driven basal melting is muted. We surmise that, towards the ice sheet interior, a network of efficient, distributed pathways develops in contrast to large melt channels. Accelerated sliding through the melt season may increase pathway discharge by enlarging space on the lee sides of bed asperities, allowing such a network to transport significant quantities of water (supplementary online text). Regardless, any working model of GrIS subglacial hydrology must reconcile observations of both pressure and drainage efficiency under relaxed gradient regimes atypical of mountain glaciers.

Accurate representation of processes driving behavior of ice/water interactions at the ice sheet bed is crucial to understanding drainage system evolution and our ability to quantify the impact of surface meltwater input on ice sheet acceleration. Our results caution against the direct transfer of processes from the alpine setting to ice sheet interior where geometric differences are accentuated. Future efforts to assess drainage dynamics away from the ice sheet margin should focus on developing additional mechanisms for growing drainage system efficiency, such as sliding over bedrock. The importance of processes in this interior regime is paramount considering that surface melt extent and intensity have increased over the GrIS during the observational era (*27*, *28*) and future warming is projected to expand melt intensity towards the ice sheet interior.

References and Notes:

1. A. J. Sole *et al.*, Seasonal speedup of a Greenland marine-terminating outlet glacier forced by surface melt–induced changes in subglacial hydrology, *Journal of Geophysical Research* **116**, 1–11 (2011).

2. I. Joughin *et al.*, Seasonal speedup along the western flank of the Greenland Ice Sheet., *Science (New York, N.Y.)* **320**, 781–3 (2008).

3. I. Bartholomew *et al.*, Seasonal evolution of subglacial drainage and acceleration in a Greenland outlet glacier, *Nature Geoscience* **3**, 408–411 (2010).

4. I. Bartholomew *et al.*, Short-term variability in Greenland Ice Sheet motion forced by time-varying meltwater drainage: Implications for the relationship between subglacial drainage system behavior and ice velocity, *Journal of Geophysical Research* **117**, 1–17 (2012).

5. S. Palmer, A. Shepherd, P. Nienow, I. Joughin, Seasonal speedup of the Greenland Ice Sheet linked to routing of surface water, *Earth and Planetary Science Letters* **302**, 423–428 (2011).

6. A. V. Sundal *et al.*, Melt-induced speed-up of Greenland ice sheet offset by efficient subglacial drainage, *Nature* **469**, 521–4 (2011).

7. A. Shepherd *et al.*, Greenland ice sheet motion coupled with daily melting in late summer, *Geophysical Research Letters* **36**, 2–5 (2009).

8. H. J. Zwally *et al.*, Surface melt-induced acceleration of Greenland ice-sheet flow., *Science (New York, N.Y.)* **297**, 218–22 (2002).

9. R. S. W. van de Wal *et al.*, Large and rapid melt-induced velocity changes in the ablation zone of the Greenland Ice Sheet., *Science (New York, N.Y.)* **321**, 111–3 (2008).

10. M. J. Hoffman, G. A. Catania, T. A. Neumann, L. C. Andrews, J. A. Rumrill, Links between acceleration, melting, and supraglacial lake drainage of the western Greenland Ice Sheet, *Journal of Geophysical Research* **116**, 1–16 (2011).

11. C. Schoof, Ice-sheet acceleration driven by melt supply variability., *Nature* **468**, 803–6 (2010).

12. T. C. Bartholomaus, R. S. Anderson, S. P. Anderson, Response of glacier basal motion to transient water storage, *Nature Geoscience* **1**, 33–37 (2008).

13. I. Bartholomew *et al.*, Supraglacial forcing of subglacial drainage in the ablation zone of the Greenland ice sheet, *Geophysical Research Letters* **38**, 1–5 (2011).

14. D. M. Chandler *et al.*, Evolution of the subglacial drainage system beneath the Greenland Ice Sheet revealed by tracers, *Nature Geoscience* **6**, 195–198 (2013).

15. H. H. Thomsen, O. B. Olesen, Hydraulics and hydrology on the Inland Ice, *Rapport - Grønlands Geologiske Undersogelse* **152**, 36–38 (1991).

16. H. H. Thomsen, O. B. Olesen, R. J. Braithwaite, C. E. Boggild, Ice drilling and mass balance at Pakitsoq, Jakobshavn, central West Greenland, *Rapport - Grønlands Geologiske Undersogelse* **152**, 80–84 (1991).

17. A. Iken, K. Echelmeyer, W. Harrison, M. Funk, Mechanisms of fast flow in Jakobshavns Isbrae, West Greenland: Part I. Measurements of temperature and water level in deep boreholes, *Journal of Glaciology* **39**, 15–25 (1993).

18. M. Lüthi, M. Funk, A. Iken, S. Gogineni, M. Truffer, Mechanisms of fast flow in Jakobshavn Isbrae , West Greenland: Part III . Measurements of ice deformation , temperature and cross-borehole conductivity in boreholes to the bedrock, *Journal of Glaciology* **48**, 369–385 (2002).

19. Materials and methods are available as supplementary material on Science Online.

20. B. Hubbard, M. Sharp, I. Willis, M. Nielsen, C. Smart, Borehole water-level variations and the structure of the subglacial hydrological system of Haut Glacier d’Arolla, Valais, Switzerland, *Journal of Glaciology* **41**, 572–583 (1995).

21. A. Iken, R. A. Bindschadler, Combined measurements of subglacial water pressure and surface velocity of Findelengletscher , Switzerland : Conclusions about drainage system and sliding mechanism, *Journal of Glaciology* **32**, 101–119 (1986).

22. B. Kamb, Glacier Surge Mechanism Based on Linked Cavity Configuration of the Basal Water Conduit System, *Journal of Geophysical Research* **92**, 9083–9100 (1987).

23. H. Röthlisberger, Water Pressure in Intra- and Subglacial Channels, *Journal of Glaciology* **11**, 177–203 (1972).

24. D. van As *et al.*, Large surface meltwater discharge from the Kangerlussuaq sector of the Greenland ice sheet during the record-warm year 2010 explained by detailed energy balance observations, *The Cryosphere* **6**, 199–209 (2012).

25. D. McGrath, W. Colgan, K. Steffen, P. Lauffenburger, J. Balog, Assessing the summer water budget of a moulin basin in the Sermeq Avannarleq ablation region, Greenland ice sheet, *Journal of Glaciology* **57**, 954–964 (2011).

26. R. B. Alley, Towards a Hydrological Model for Computerized Ice-sheet Simulations, *Hydrological Processes* **10**, 649–660 (1996).

27. T. L. Mote, Greenland surface melt trends 1973–2007: Evidence of a large increase in 2007, *Geophysical Research Letters* **34**, L22507 (2007).

28. M. Tedesco, Snowmelt detection over the Greenland ice sheet from SSM/I brightness temperature daily variations, *Geophysical Research Letters* **34**, 1–6 (2007).

29. C. Allen, IceBridge MCoRDS L2 Ice Thickness. (2010).

30. T. Murray, G. K. C. Clarke, Black-box modeling of the subglacial water system, *Journal of Geophysical Research* **100**, 10231–10245 (1995).

31. A. G. Fountain, J. S. Walder, Water flow through temperate glaciers, *Reviews of Geophysics* **36**, 299–328 (1998).

32. G. Clarke, Lumped-element analysis of subglacial hydraulic circuits, *Journal of Geophysical Research* **101**, 17547–17559 (1996).

33. L. F. Shampine, M. W. Reichelt, The MATLAB ODE Suite, *SIAM Journal on Scientific Computing* **18**, 1–22 (1997).

34. K. M. Cuffey, W. S. B. Patterson, *The Physics of Glaciers* (Elsevier, Oxford, ed. 4th, 2010).

35. R. S. W. Van de Wal, W. Greuell, M. R. Van Den Broeke, C. H. Reijmer, J. Oerlemans, Surface mass-balance observations and automatic weather station data along a transect near Kangerlussuaq , West Greenland, *Annals of Glaciology* **42**, 311–316 (2005).

36. J. F. Nye, The Flow of Glaciers and Ice-Sheets as a Problem in Plasticity, *Proceedings of the Royal Society A: Mathematical, Physical Sciences* **207**, 554–572 (1951).

37. D. M. Chandler *et al.*, Evolution of the subglacial drainage system beneath Greenland's ice sheet revealed by tracers: Supplementary, *Nature Geoscience* (2013), doi:10.1038/NGEO1737.

38. U. Spring, K. Hutter, Numerical studies of jokulhlaups, *Cold Regions Science and Technology* **4**, 227–244 (1981).

39. N. Humphrey, K. Echelmeyer, Hot-water drilling and bore-hole closure in cold ice, *Journal of Glaciology* **36**, 287–298 (1990).

40. M. A. Werder, M. Funk, Dye tracing a jökulhlaup : II . Testing a jökulhlaup model against flow speeds inferred from measurements, *Journal of Glaciology* **55**, 899–908 (2009).

41. G. K. C. Clarke, Hydraulics of subglacial outburst floods: new insights from the Spring-Hutter formulation, *Journal of Glaciology* **49**, 299–313 (2003).

42. A. P. Ahlstrøm, J. J. Mohr, N. Reeh, E. L. Christensen, R. L. Hooke, Controls on the basal water pressure in subglacial channels near the margin of the Greenland ice sheet, *Journal of Glaciology* **51**, 443–450 (2005).

43. S. B. Das *et al.*, Fracture propagation to the base of the Greenland Ice Sheet during supraglacial lake drainage., *Science (New York, N.Y.)* **320**, 778–81 (2008).

Acknowledgements
We thank Dr. J. Johnson for his thoughtful review and comments that improved this manuscript. Many thanks to all those who provided field assistance. This work is funded by the Greenland Analogue Project (GAP) and NSF (OPP-ANS #0909495).

Supplementary Materials

www.sciencemag.org
Materials and Methods
Supplementary Text
Figs. S1, S2, S3, S4, S5, S6
References (30-43)

Figures:

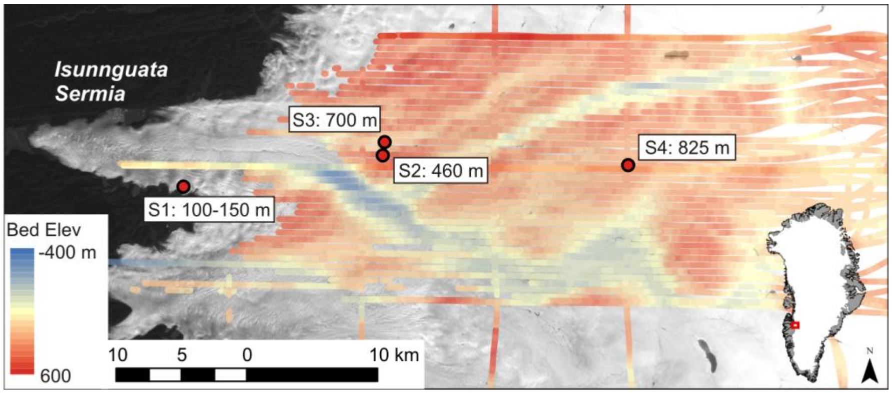

Fig. 1. Site setting with bedrock topography from ICEBRIDGE airborne radar (*29*) extending east from Isunnguata Sermia. Drill sites are denoted by red dots with site number and ice thickness for reference.

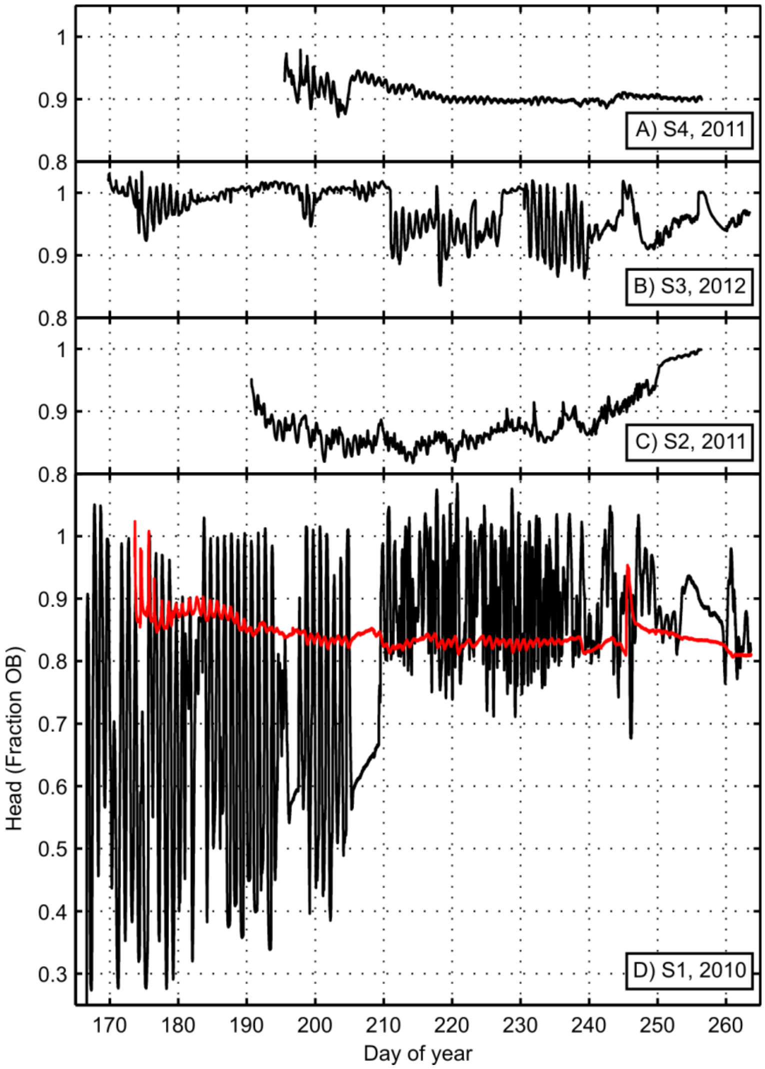

Fig. 2. Characteristic long term water pressure records at sites 1 – 4 as fraction of overburden. Site S1 (D) showed significant spatial variability with some holes showing large diurnal variations (black line) while others showed small amplitude variations at high pressure (red line). Slow water level increase during day of year 205 – 210 at S1 (black line) may represent slow closure of an efficient connection or advection of the borehole away from such a hydrologic feature. Boreholes were drilled over the course of 3 field seasons, thus presented pressure records do not all span the same time period (drill year is shown in panel box). Head as fraction of overburden pressure (h_{ob}) is calculated as $h_{ob} = \frac{h_w \rho_w}{h_i \rho_i}$ where h_w is head equivalent of water pressure measured in the borehole, h_i is ice thickness, and ρ_w and ρ_i are water and ice densities respectively.

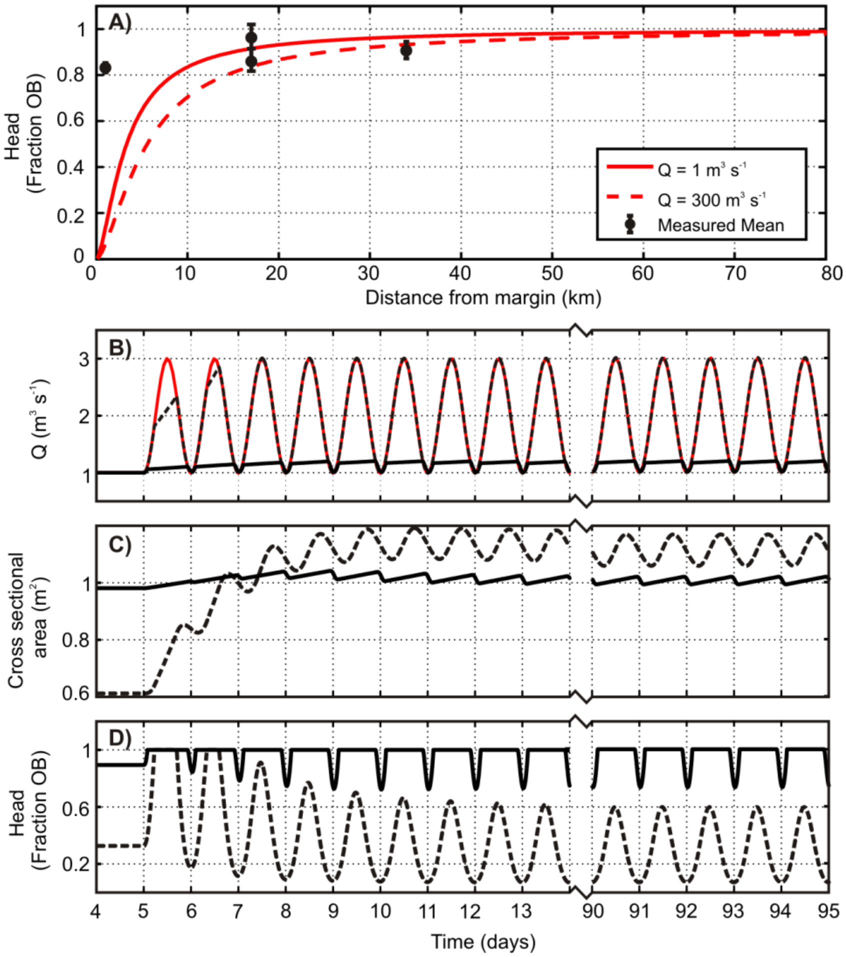

Fig. 3. Simulation results from steady state conduit analysis (A), and transient experiments (B-D). Steady state conduit simulations were performed for an envelope of discharges ranging from a low of 1 $m^3 s^{-1}$ (solid red line in (A)) to an upper limit of 300 $m^3 s^{-1}$ (dashed red line) guided by proglacial measurements (*4*). Mean pressures encompassing day-of-year 200 – 240 from distributed network measurements are shown by black dots; vertical bars denote maximum and minimum pressures during the time period. Transient experiments are forced with diurnally varying input (red line in (B)). Conduit discharge (B), cross sectional area (C), and head as fraction of OB (D) are displayed at 3 km and 40 km for the margin (dashed) and inland (solid black line) scenarios respectively. Margin and inland scenarios are assumed to be representative of conditions expected near S1 and S4.

Supporting Online Material for:

Basal Drainage System Response to Increasing Surface Melt on the Greenland Ice Sheet

T. Meierbachtol, J. Harper, N. Humphrey

Materials and Methods

Borehole Drilling Methods.

We drilled boreholes using hot water methods (see Table S1 for site locations and drilling year). Heating surface water to ~68˚ C and pressurizing it to ~8 MPa allowed drilling rates which exceeded 100 m hr^{-1}. We reduced the drilling rate as depth increased in boreholes greater than 450 m to counter heat loss through the drill hose to the surrounding deep borehole. We confirmed penetration to the ice sheet bed through three independent measures: 1) a drop in borehole water level indicates intersection with the basal hydrologic network (Fig. S1), 2) drop in load on a drill-mounted load cell indicates that the weight of the drill stem and hose down the hole is transferred from the drill rig to the ice sheet bed, and 3) water pressure spikes in the drill hose which are interpreted to result from enhanced backpressure as the drill tip approaches an immobile boundary such as frozen debris or the bed. Not all indicators occurred concurrently when approaching the bed; in some instances we measured dropping borehole water levels 30 m prior to registering a consistent pressure spike and load drop. We measured hole depth with an odometer mounted on the drilling wheel, manual inspection of tick marks on the drilling hose during drilling, and measurement of sensor cable length during pressure transducer deployment. From these three methods, we estimate the accuracy of our drill depths to be better than 1.5% of total ice thickness, or 10 m in deep boreholes.

Instrumentation Methods.

Pressure was logged at five minute intervals during summer and reduced to 30 minute intervals during winter. The resolution of the system is approximately 0.1 m of water level change. In deep boreholes, we performed in-situ absolute calibrations after installation against temporary pressure transducers referenced at the ice sheet surface. Because the depth of the holes is known to within 1.5% of ice thickness, we conservatively estimate the absolute offset of pressure records in deep boreholes to be similar in magnitude (10 m).

Accepting that boreholes act as accurate manometers representing subglacial conditions assumes that: 1) the influence of surface input to the borehole is negligible, 2) the borehole itself is connected to the subglacial system, 3) the pressure transducer is located low enough in the borehole so that creep closure or refreezing does not isolate the sensor from the basal system to which it is connected, and 4) the volume of water required for a given change in borehole water level is small compared to the volume of water in the drainage system. On the GrIS, cold englacial ice ensures that boreholes freeze closed in hours to days, eliminating the possibility of water entering the borehole at the surface. Water levels in all interior boreholes showed a rapid decline following breakthrough to the subglacial system during drilling (Fig. S1) and exhibited water level variations thereafter; supporting evidence that the borehole itself is connected to an active portion of the subglacial hydrologic network (*30*, *31*). From real-time pressure monitoring as we lowered the transducers into the boreholes during installation we estimate the maximum sensor placement above the bed to be 5 m, and likely to be no more than 2 m. Thermal profiles at all zones show temperate ice above transducers, hence closure around the sensor from refreezing is eliminated. Borehole refreezing at depth ensures that borehole pressure variations are a direct reflection of pressure changes at the bed and not influenced by volume discrepancies associated with changes in borehole water level. Thus, all four conditions are satisfied and we conclude that our pressure measurements are representative of subglacial pressure dynamics.

We performed impulse tests by perturbing the subglacial system to which boreholes were connected with injection of either a constant volume (slug test) or constant discharge (pumping test) of water at the surface. Water levels were recorded at sampling intervals no greater than 2 s prior to and during testing. Small perturbation slug tests are easily repeatable and were performed in all boreholes to investigate hydrologic system response to small water pressure perturbations. Rapid closure from refreezing in our deepest boreholes precluded the performance of longer duration pumping tests in holes.

Model Development.

We implement a conduit melt-closure model which is conceptually represented by a semicircular basal melt channel extending from atmospheric conditions at the ice sheet margin to a given distance inland where it connects to a moulin. The model set-up is guided by the lumped element formulation presented by Clarke (*32*), and is fundamentally equivalent to the channel equations presented therein. We discretize the conduit along its length to more highly resolve inland processes in light of long conduit extents (Fig. S2). Cross-sectional area change of the channel is governed by the balance between conduit growth through melt-back of the ice walls, and closure by creep processes. Water flow through the conduit (Q), cross-sectional area (S), and the pressure gradient (Ψ) are related via turbulent flow through the conduit. In the context of the present formulation, inclusion of an opening term from sliding is akin to assuming a constant linear bedrock feature running the length of the model conduit (up to 40 km). Because such a feature is highly unlikely, we omit an opening term from sliding. Equations governing cross-sectional area change and the potential gradient are given respectively as:

$$\frac{dS}{dt} = c_1 Q\Psi - c_2 N^n S \qquad (1$$

$$\Psi = c_3 Q^2 S^{-5/2} \qquad (2$$

with constants $c_1 = \frac{1-\gamma}{\rho_i L}$ and $\gamma = \rho_w c_w c_t$, $c_2 = 2A/n^n$, $c_3 = (\pi + 2)\rho_w f/(2^{5/2}\sqrt{\pi})$,

effective pressure $N = g(\rho_i h_{ice} - \rho_w h_w)$, and potential gradient $\Psi = \rho_w g\left(\frac{\partial h_w}{\partial s} + \frac{\partial z_b}{\partial s}\right)$.

Physical variables h_i, h_w and z_b refer to ice thickness, equivalent conduit pressure head in meters, and bed elevation respectively. The heat required to warm the basal water to the pressure melting point beneath thinner ice is taken in to account by the constant γ. Other physical constants and parameters are listed in Table S2.

At each conduit section ij between upglacier node j and downglacier node i with length l, flow continuity is enforced. The additional water generated from melt of conduit walls is small in comparison to the flux through the conduit and is thus neglected. Together with continuity, Eqs. 1 and 2 are recast to yield a system of differential algebraic equations (DAEs) to solve for Q, S, and conduit head h_w:

$$\nabla Q = 0 \qquad (3$$

$$\frac{dS_{ij}}{dt} = c_1 Q_{ij} \rho_w g \left(\frac{h_{w,j} - h_{w,i} + z_{b,j} - z_{b,i}}{l_{ij}} \right) - c_2 N_{ij}^n S_{ij} \qquad (4$$

$$h_{w,j} = h_{w,i} - (z_{b,j} - z_{b,i}) + \frac{l_{ij} c_3}{g \rho_w} Q_{ij}^2 S_{ij}^{-5/2}. \qquad (5$$

The effective pressure is calculated as the mean across the conduit length $N_{ij} = \frac{N_i + N_j}{2}$.

At the conduit – moulin intersection, surface input and output through the conduit are balanced to yield the head change in the moulin:

$$\frac{dh_{w,m}}{dt} = \frac{Q_{in} - Q_{out}}{S_{moulin}} \qquad (6$$

where S_{moulin} is the moulin cross-sectional area, and Q_{out} is calculated by rearrangement of Eq. 2:

$$Q_{out} = c_3^{-1/2} S_{j,m}^{5/4} g \rho_w \left(\frac{h_{w,m} - h_{w,j} + z_{b,m} - z_{b,j}}{l_{j,m}} \right). \qquad (7$$

Q_{out} sets the discharge through the conduit. We impose a maximum head value equivalent to overburden in the moulin, assuming that additional water input would result in localized uplift and transport in to the adjacent basal system instead of further increasing head values. Because we focus on isolated conduit dynamics, we do not model storage processes here. Instead, we assume any additional input leaves the system. The full system of DAEs is solved in Matlab using ODE15s, a variable order solver which uses backward differences to implement the numerical differentiation formulas (*33*). Step size in the model is variable, but limited to a maximum of 1.5 hours.

For all steady and transient simulations we impose a parabolic ice sheet surface profile (*34*) given by:

$$h = \sqrt{\frac{2\tau}{\rho g}(L - x)} \qquad (8$$

where we take the yield stress τ to be 100 kPa. We assume a horizontal bed along the length of the model domain. The resulting model surface gradient is quite similar to the 141 km long K-Transect, which is slightly south of our study region (*35*). Sensitivity testing with a synthetic ice sheet profile assuming a 1° positive bed slope following Nye (*36*) does not significantly alter results.

In transient simulations we force the conduit – moulin system with diurnally varying input ranging from 1 – 3 $m^3\ s^{-1}$. The input amplitude is guided by previous measurements (*25*, *37*), as well as by measurements made in a supraglacial stream during our 2012 field season at site S3. Additional transient simulations with variable discharge are discussed below. The model is run to steady state with a constant discharge set to the minimum value. The final results are then used as initial conditions for the transient scheme in which discharge varies.

Heat Transfer.

A fraction of frictionally generated heat in the model is required to warm basal water to the pressure melting point as overlying ice pressure diminishes towards the terminus. The remaining heat is instantaneously transferred to the conduit wall for melting. This formulation differs from the alternative Spring-Hutter thermal treatment for conduit flow, which tracks water temperature change and calculates conduit melt based on the temperature difference between ice and water, and an empirical heat transfer coefficient

(*38*). The instantaneous heat transfer assumption in our model precludes it from accounting for additional melting from temperature differences which may occur where surface water at, or near 0˚ C is routed to the bed where the pressure melting point is depressed by the overlying ice. Beneath thick ice this can result in temperature differences of up to 0.5˚ C or more. Such a temperature differential, however, would require no heat transfer to the moulin walls, which would cool melt water as it travels from the surface to bed. Previous analysis of hot water drilling shows that turbulent heat transfer in boreholes is 98% efficient over the length of deep boreholes (*39*). While this may be a maximum considering the large temperature difference between hot drill water and surrounding ice, it nonetheless suggests that heat transfer may be efficient enough to equilibrate melt water to basal surroundings by the time surface flow reaches the bed. Furthermore, implementation of a close variant of the Spring-Hutter equations has shown decreased heat transfer and slower basal conduit melt (*40*, *41*), suggesting that the instantaneous heat transfer assumption in our implementation overestimates conduit melt, and hence growth (*41*). Because we are concerned with maximum conduit melt rates and growth in the drainage interior, we conclude that our implementation is appropriate for the present exercise.

Steady State Model Sensitivity.

We assess steady conduit conditions by setting $\frac{dS}{dt} = 0$ in Eq. 1, and manipulating Eqs. 1 and 2 to achieve a single formula for the steady conduit pressure gradient:

$$\Psi = c_4^{5/7} A^{5/7} Q^{-1/7} (P_{OB} - P)^{15/7} \qquad (9$$

where $c_4 = \dfrac{2\rho_i L}{27(1-\gamma)\left(\dfrac{2^{5/4}\sqrt{\pi+2}}{\pi^{1/4}\sqrt{\rho_w f}}\right)^{-4/5}}$. Eq. 9 is fundamentally equivalent to Eq. 11 derived by Röthlisberger (*23*) using $n = 3$, with distinctions that we have here applied the derivation to a semi-circular conduit and utilize the Darcy Weisbach formula to relate discharge to head loss.

We assess the influence on the steady pressure curve of the flow rate factor (A), the Darcy friction factor (f), and the discharge (Q) through the conduit by calculating the pressure field over a range representing maximum and minimum values presented in previous literature (shown in Table S3). We find that the reference steady state conditions presented in Fig. 3 represent pressure conditions which are reasonable considering the range of published tuning parameters (Fig. S3). Steady state pressure is sensitive to the flow rate factor (A), which previous work has shown must be quite high to match measured water pressures (*21*, *23*). This may be due in part to changes in conduit geometry or channel sinuosity which act to increase steady state channel pressures (*42*). Channel sinuosity increases pressure by inducing additional energy loss through added turbulence from change in flow direction. Broad, flat subglacial channels increase the steady pressure by weakening of the tunnel arch, thus enhancing closure rates. These effects are not accommodated in our modeling and would act to increase the steady state pressure curve. With this in mind, we assume that the steady analysis presented (Fig. 3) represents low expected steady state conduit pressures.

Supplementary Text

Transient Conduit Growth Rates.

The ability of the subglacial drainage network to rapidly evolve from an inefficient, distributed system to an efficient network of melt dominated channels relies on expansion of the basal channels through melting of the ice walls. Here we investigate the time scales of conduit growth in the drainage interior by assessing conduit response to sinusoidal input discharge variations with differing periods of oscillation. We constrain our investigation to changes in background daily and seasonal flow, and do not address catastrophic lake drainage events. This is justified considering the effect of such drainage events on surface velocity appears to be highly localized in space and time (*10*, *43*), indicating a minor impact on the subglacial system.

We extend the analysis presented in the manuscript, where input discharge varies diurnally from 1 – 3 $m^3 s^{-1}$, to longer seasonal time scales of discharge variation. We also perform the analysis for an input discharge which varies from 1 – 20 $m^3 s^{-1}$ which may illustrate a seasonal variation in water flux routed through potential conduits at the bed of the ice sheet this far inland. We find that conduit growth rates are slow enough that the period of input variation must be 90 days for conduit growth to capture a discharge increase from 1 – 3 $m^3 s^{-1}$ (Fig. S4). Under diurnally varying input, the basal conduit is only able to grow to accommodate ~14% of the changing input above 1 $m^3 s^{-1}$. Experiments simulating large changes in discharge show that limited conduit expansion results in a significant discrepancy between input and basal accommodation for all periods of input variability. While the imposed discharge increases to 20 $m^3 s^{-1}$ over a 45 day interval, the basal conduit expands to accommodate just 8.6 $m^3 s^{-1}$. Similar conduit growth rates have been reported (*37*) in the absence of variable discharge.

Analysis with a single input point omits possible effects of multiple basal features convening to a larger trunk. To accommodate the aggregated effect of multiple inputs, we perform a numerical experiment whereby we impose additional discrete meltwater input points at 8, 16, 24, and 32 km inland from the margin (in addition to the input node at 40 km). Each input point is forced with a discharge curve made up of a convolution of seasonal and diurnal signals (red line in Fig. S5). The seasonal cycle of 90 days is more or less consistent with the period of temperature variation at 1000 m elevation for the extreme melt season in 2010 (*24*). Diurnal discharge variability increases to a maximum amplitude of 8 $m^3 s^{-1}$. The sum of these inputs is of the same order of magnitude as reported discharge values at the terminus of nearby Leverett Glacier (*13*), but we note that the input curve defined here is meant to be illustrative of reasonable real world conditions. The intent is not to match our observed pressure behavior or directly forecast basal conditions.

We simulate conduit growth for two differing initial discharge values to assess the sensitivity of behavior to initial cross sectional area. In the high discharge simulation the background flux at each input point is set to 1 $m^3 s^{-1}$, resulting in a cumulative discharge of 5 $m^3 s^{-1}$ at the terminus. This initial discharge is likely an upper end member estimate considering that surface inputs are eliminated during the winter period and background basal melt rates (from geothermal heat flux and frictional heating as ice slides over the bed) are low. Nevertheless, under such initial conditions slow growth of conduits requires nearly 2 months before discharge through the conduit reaches the diurnal input minimum

(Fig. S5). A simulation with low initial discharge of 0.3 m^3 s^{-1} (cumulative sum of 1.5 m^3 s^{-1} at the terminus), a value perhaps more representative of background winter flux, results in growth rates which limit conduit development over the entire simulation period. Maximum discharge reaches an order of magnitude greater than the initial condition in this low flux scenario, but only after 10 weeks of growth (Fig. S5). The effect of increasing potential gradients from enhanced discharge towards the terminus appears to be small in both experiments. This analysis suggests that in the interior region, expansion of the conduit network necessitates time scales longer than the likely seasonal evolution of input to the basal system through the melt season. Further, the low initial discharge simulation emphasizes the role of processes besides melting in enhancing efficiency when antecedent conditions are dormant.

Stability of Bedrock Roughness-Dominated Drainage.

The switch from a drainage regime driven by sliding over bedrock, to a regime where growth is driven by melt-back of the ice walls is not necessarily confined to low discharge rates. Here, using the equation for critical discharge presented by Schoof (*11*), we show that the ice sheet setting away from the margin provides local conditions which enhance the stability of bedrock roughness-dominated drainage elements. The critical discharge equation denotes the point where growth from melt of ice walls dominates over opening from sliding:

$$Q_c = \frac{u_b h}{c_1(\alpha - 1)\Psi} \qquad \text{(10}$$

where u_b is sliding velocity, h is bedrock step height, and $\alpha = 5/4$. Assuming a reasonable sliding velocity of 60 m yr^{-1}, critical discharge reaches values on the order of multiple m^3 s^{-1} for potential gradients indicative of interior ice sheet conditions **(**Figure S6**)**. Under potential gradients similar to those along the K-transect 30-40 km inland (Ψ = 150 Pa m^{-1}), drainage features dominated by sliding over a rough bed maintain stability at discharges greater than 2 m^3 s^{-1} for small roughness heights. Critical discharge values >1 m^3 s^{-1} are maintained under potential gradients more than double that presented above. We take this steady analysis as illustration that away from the ice sheet margin, local drainage through features driven by sliding processes can maintain stability under measurable discharge. Under these situations drainage pathways would take the shape of broad, low features with considerable basal coverage.

Supplementary Figures

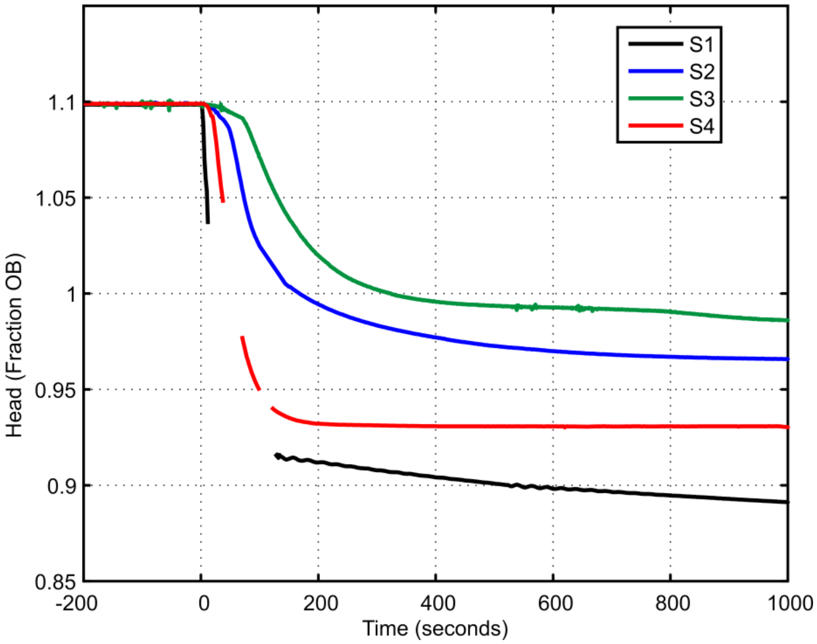

Figure S1: Example of borehole water level drop at each site in response to intersection with the basal network during drilling. Water levels remain at the ice surface during drilling, resulting in water levels above ice overburden pressure at time of intersection. Broken lines (Sites S1 and S4) result from water levels temporarily dropping below the level of the pressure transducer until sensors were reset. Time $t = 0$ sec is manually chosen at the break in slope, indicating the onset of water level drop.

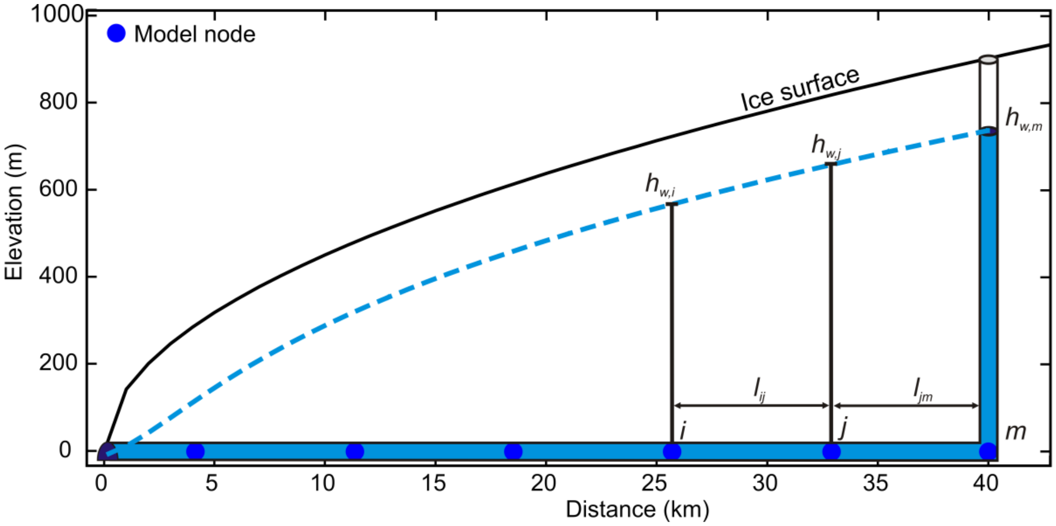

Figure S2: Schematic of model set-up with ice sheet model surface profile (black line). Conceptual conduit water pressure is denoted by the dashed blue line.

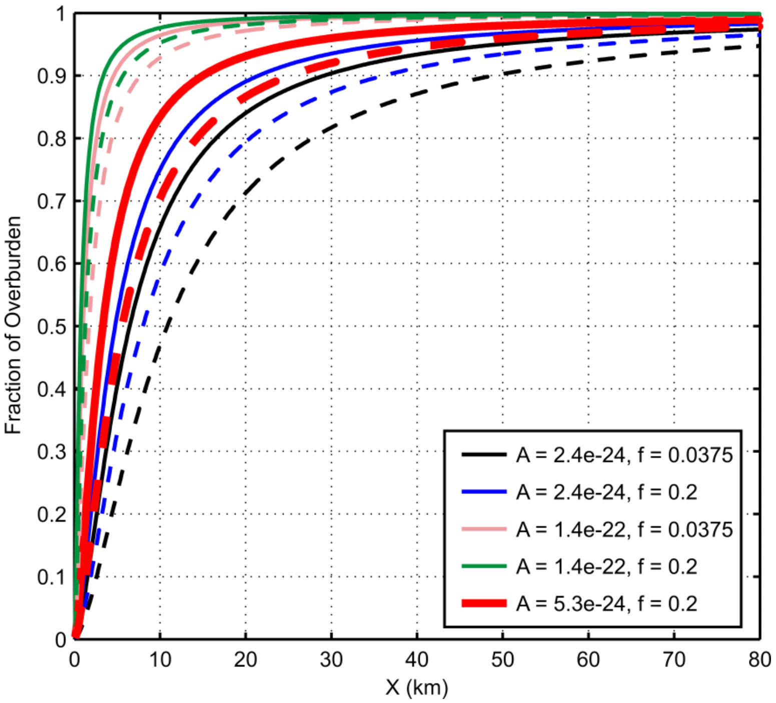

Figure S3. Steady state simulation results for a range of discharge (Q), flow rate factor (A), and friction factor (f) values. Results for maximum discharge values of 300 m^3 s^{-1} are displayed as dashed lines, and those for minimum discharge values of 1 m^3 s^{-1} are displayed as solid lines for each of the flow rate factor and friction factor combinations (various colors). Results for reference parameter values used in the manuscript are presented as thick red lines.

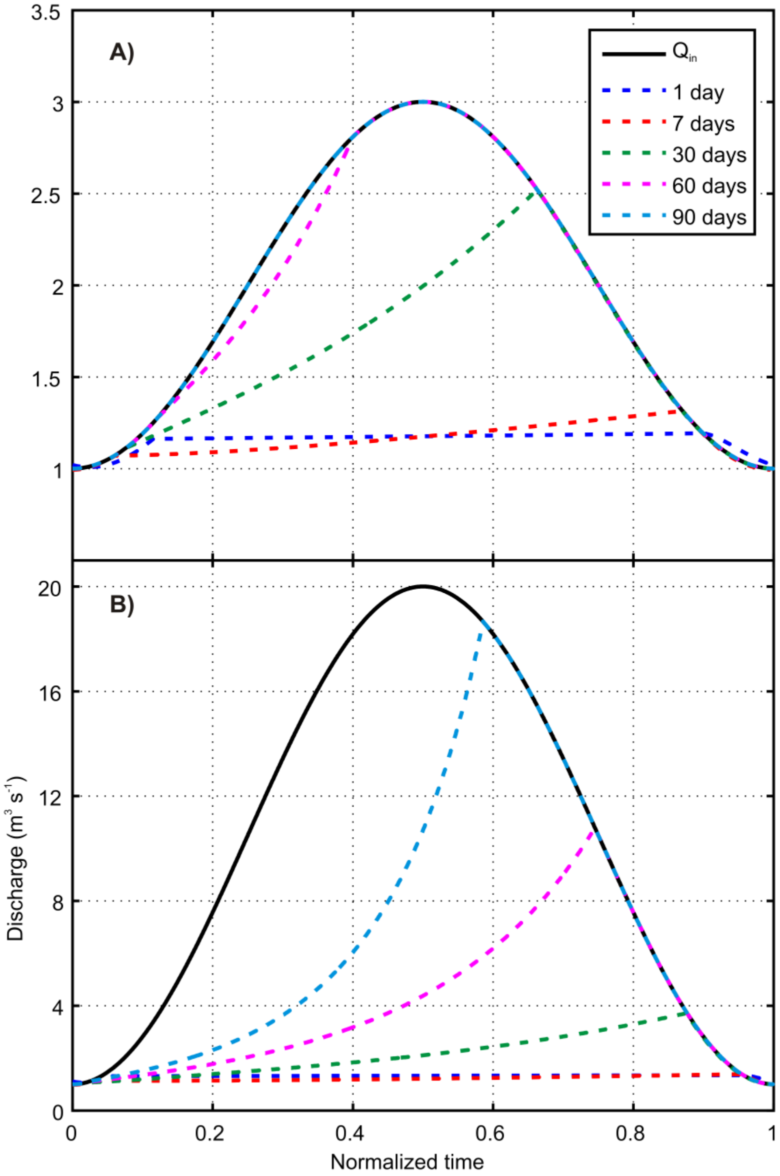

Fig. S4. Conduit discharge (dashed lines) in response to input whose magnitude rises and falls over a sweep of time periods ranging from 1 day to 90 days. A single input cycle (black line) is isolated and normalized to the input period to facilitate display of all simulations. Two sets of simulations are shown for small input variation from 1 – 3 $m^3 s^{-1}$ (A), and a larger change from 1 – 20 $m^3 s^{-1}$ (B).

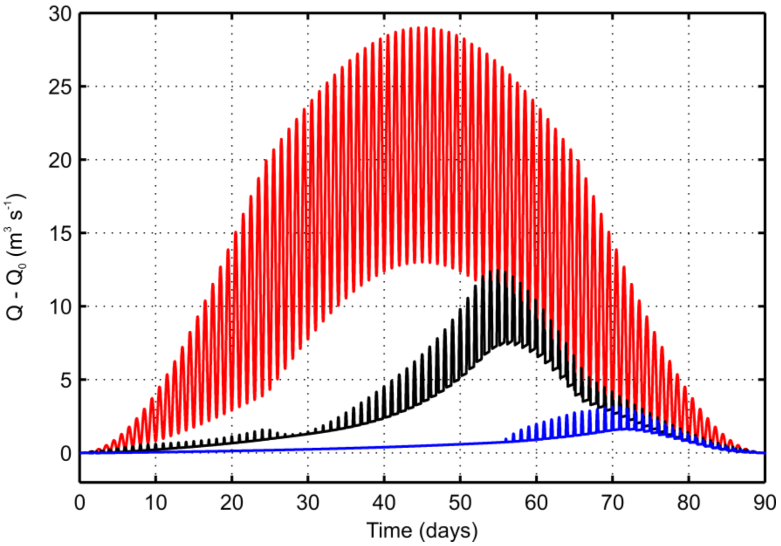

Fig. S5. Simulated seasonal discharge at each input point (red line) and resulting flux at 40 km inland for an initial discharge value of 1 m^3 s^{-1} (black line) and 0.3 m^3 s^{-1} (blue line). To facilitate presentation of both simulations, y-axis is the difference between discharge at time t, and initial discharge.

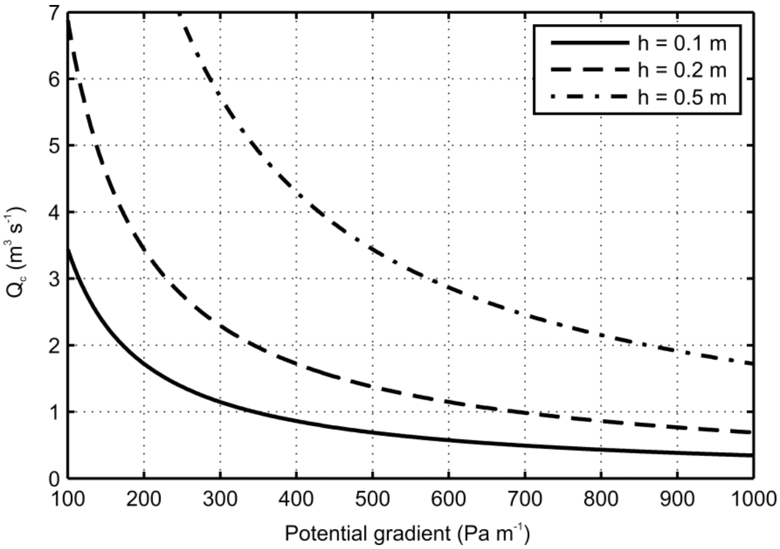

Figure S6. Critical discharge (Q_c) for bedrock step height and potential gradient conditions. Step heights ranging from 0.1 to 0.5 were chosen to illustrate the effect of increasing roughness on discharge.

Supplementary Tables

Site	Latitude	Longitude	# of Holes	Year drilled	Physical Characteristics
S1	67.1622	-50.0642	6	2010	- Nearby crevassing
	67.1670	-50.0663	5	2010	- Surface stream (>3 m^3 s^{-1}) within 200 m
	67.1593	-50.0593	2	2012	- Nearby crevassing
S2	67.1952	-49.7195	3	2011	- Topographic ridge - Multiple moulins within 500 m - Supraglacial lake within 1 km in 2012
S3	67.2042	-49.7179	4	2012	- Surface stream (1-3 m^3 s^{-1}) within 50 m
S4	67.2015	-49.2890	4	2011	- Moulin within 500 m - Multiple surface streams (<3 m^3 s^{-1}) - 3 of 4 boreholes drilled to the bed.

Table S1. Site latitudes, longitudes, number of holes drilled, and drilling year. Boreholes were drilled at three locations ~1 km apart near the margin at Site 1.

Symbol	Value	Units	Description
ρ_w	1000	kg m^{-3}	density of water
ρ_i	910	kg m^{-3}	density of ice
c_w	4.22e3	J kg^{-1} K^{-1}	specific heat capacity of ice
c_t	7.5e-8	J kg^{-1} K^{-1}	pressure melting coefficient
A	5.3e-24	Pa^{-3} s^{-1}	flow rate factor of ice
n	3	-	Glen's flow law exponent
g	9.81	m s^{-2}	gravitational acceleration
f	0.2	-	Darcy friction factor
S_m	2.0	m^2	moulin cross sectional area

Table S2. Physical parameters used in the melt-closure model.

	Discharge (Q)	Flow Rate Factor (A)	Friction Factor (f)
Low	1 (*25*)	2.4e-24 (*34*)	0.0375 (*11*)
High	300 (*13*)	1.4e-22 (*23*)	0.2 (*4*)

Table S3. High and low values for steady state parameter sweep.

CHAPTER 2

IMPACT OF FIELD-CONSTRAINED BOUNDARY CONDITIONS ON WESTERN GREENLAND'S THERMO-MECHANICAL STATE

Abstract:

Boundary conditions drive thermal behavior on the Greenland Ice Sheet, but a lack of observational constraints forces numerical models to prescribe boundary temperature and heat flux from independent model output. Here, we quantify the difference between observations and commonly used boundary condition datasets over a land terminating sector of western Greenland. Through numerical techniques we investigate the sensitivity of the modeled thermal regime to boundary adjustments, using in-situ full-thickness temperature profiles at multiple sites in the ablation zone to assess modeled partitioning of heat flow. To constrain the surface boundary, we measured near-surface temperature in two 20 m boreholes in the ablation zone from 2011 – 2013, and augment these data with existing 10 m firn temperature observations in western Greenland's percolation zone. We constrain basal heat flux using in-situ measurement in a deep bedrock hole at the study area margin, and existing heat flux assessments. Measured basal heat flux at our study area is <50% of spatially distributed models. In contrast, measured near-surface temperatures are warmer than the modeled counterpart with magnitudes exceeding 10°C. Lower heat flux induces a model cold bias compared to measured temperature profiles, and frozen basal conditions across the ablation zone. Temperate basal conditions are re-established under surface boundary adjustments. Warmer surface ice and firn can introduce three times more energy to the modeled ice

mass than is removed at the bed due to reduced basal heat flux, indicating that near-surface effects must be adequately prescribed in thermo-mechanical modeling experiments.

1 Introduction

In recent years, substantial advances have been made to deterministic models of the Greenland Ice Sheet (GrIS), motivated by the need to constrain potential changes in coming centuries. Higher-order physics have been adopted [e.g. *Larour et al.*, 2012; *Brinkerhoff and Johnson*, 2013], surface and bed geometry has been illuminated [*Bamber et al.*, 2013], and surface velocity fields provide coverage at a sufficient level to provide a target for model tuning at the full ice sheet scale[*Joughin et al.*, 2010; *Rignot and Mouginot*, 2012]. Yet, despite these advancements, the upper and lower thermal boundaries of the ice sheet remain poorly constrained by direct observations. These boundary conditions dictate the global thermal regime of the ice sheet, therefore strongly control internal deformation via the temperature-dependent flow-rate factor and transitions from frozen to melted basal conditions which govern basal sliding.

Modeling the GrIS requires prescription of the surface boundary condition, taken as the temperature at a shallow depth where seasonal variations are damped. However, observations in the near-surface layer (~10 meters (m) depth) are limited to a relatively small number of point measurements around the ice sheet, many of them only sporadic [*Benson*, 1962; *Mock and Weeks,* 1965; *Echelmeyer et al.*, 1992; *Humphrey et al.*, 2012; *Koenig et al.*, 2013]. Sparse measurements have encouraged the use of regional climate model (RCM) output to define the upper thermal boundary condition. This prescription relies on the well-established premise that the temperature at 10-15 m depth is damped to the annual surface mean [*Cuffey and Patterson*, 2010]. However, this approximation is only valid on the GrIS at high elevations in the dry snow zone [*Mock and Weeks*, 1965].

In the percolation zone where seasonal meltwater is generated, the latent heat release from refreezing of meltwater percolating to depth results in temperatures significantly warmer than the surface mean [*Echelmeyer et al.*, 1992; *Humphrey et al.*, 2012]. In the ablation zone multiple processes act to complicate near-surface temperature dynamics. Seasonal accumulation can insulate underlying ice from the winter cold wave and provide a latent heat source from refreezing of spring melt. However, this warming may be partially offset by a perceived cooling from the inability of the ice temperature to rise above 0°C in the summer months [*Hooke et al.*, 1983]. Crevasses and moulins impose a thermal influence with mixed impact. Air-filled features can induce cooling by exposing deeper ice to atmospheric conditions [*Echelmeyer et al.*, 1992], or introduce additional energy to the near-surface through increased absorption of solar radiation [*Pfeffer and Bretherton*, 1987]. When water-filled, crevasses and other macro-scale hydrologic features can provide a heat reservoir that may contribute to near-surface (or full-thickness) warming for multiple years [*Jarvis and Clarke*, 1974; *Phillips et al.*, 2010].

Thermo-mechanical ice sheet models also require prescription of the geothermal heat flux (GHF) along the basal boundary. Direct measurement of heat flow has, until recently, been limited to two sites in southern GrIS [*Sass et al.*, 1972]. Indirect model-based studies utilizing temperature records at ice core sites [*Dahl-Jensen et al.*, 1998; *Petrunin et al.*, 2013] have extended direct and indirect heat flux measurements to four point locations across the 1.71 million square kilometer (km^2) ice sheet. In the absence of direct measurements, heat flux maps are commonly prescribed in studies at the full ice sheet scale. Spatially distributed fields are generated from satellite-derived magnetic crustal thickness [*Fox Maule et al.*, 2009], or extrapolation of the global heat flux dataset based on tectonic [*Pollack et al.*, 1993], or seismic models [*Shapiro and Ritzwoller*, 2004]. However, these exhibit little consistency between one another or with independent observations. In fact, spatially uniform heat flow generally produces a better model match to observations than any of the distributed models [*Rogozhina et al.*, 2012].

The paucity of data constraining Greenland's thermal boundaries forces ice sheet models to employ boundary condition datasets which are inconsistent or neglect critical warming processes. The resulting model thermo-mechanical behavior is unlikely to reflect the current state of the GrIS, but assessment of modeled thermal biases is hindered by the lack of metrics away from the ice sheet divide [*Rogozhina et al.*, 2012; *Seroussi et al.*, 2013]. Thus, the thermal state of the majority of the ice sheet remains subject to considerable uncertainty, motivating the work here. In this study we investigate upper and lower thermal boundary conditions on the GrIS and the sensitivity of model behavior to observation-constrained boundaries. We target our study on a >14,000 km^2 region of western Greenland which has been the focus of recent ice- and bedrock borehole studies. We begin by refining thermal boundary conditions to honor novel in-situ data from these field campaigns, including ablation zone ice temperature and direct measurement of bedrock heat flux. We augment these data with firn temperature measurements and additional GHF values from observation, and assess the differences between commonly used, model-based datasets and our observation-constrained boundary conditions. Finally, we test the response of a higher-order numerical ice sheet model to our altered boundary conditions. To assess model output, we use full-thickness temperature measurements collected in a transect of deep boreholes through the ablation zone.

2 Methods

We begin the methodology with a description of the study area, the spatially distributed surface and basal boundary datasets we choose to use as ‘reference’ fields, and methods used to gather field data and generate observation-based boundary conditions. We follow this with a description of the ice sheet model and modeling experimental set-up.

2.1 Study area

We focus the study on a subsection of the western GrIS extending east from Isunnguata Sermia (IS), a land terminating outlet glacier, to the ice sheet divide (Figure 1). This study domain contains a relatively rich suite of measurements to inform modeling decisions and interpretation. The domain contains intensive airborne radar data captured through the ICEBRIDGE project and has been the focus of an intensive borehole drilling campaign [*Meierbachtol et al.*, 2013]. From 2010 - 2012, we drilled boreholes to the ice sheet bed using hot water methods at sites spanning a transect in the ablation zone where ice thickness ranged from 100 - 825 m. We measured temperature through the ice column in boreholes at 4 sites, and augmented the data with detailed near-surface temperature measurements at two of the field locations. Near-surface temperature measurements in the percolation zone have been collected ~270 km to the north of our study domain at 14 sites along the EGIG transect [*Humphrey et al.*, 2012]. Finally, recent bedrock drilling at the ice sheet margin provides unique constraints on in-situ geothermal heat flux [*Harper et al.*, 2010].

In modeling experiments, we define the model domain by extending 15 - 20 km north and south of the IS terminus. Lateral boundaries follow the ice sheet surface slope to the divide, closing the domain. Constraining the domain in this way facilitates better focus on reaches with dense observation (as opposed to forcing full ice sheet simulations) while still allowing transverse gradients throughout the domain in contrast to two-dimensional flowline modeling.

2.2 Reference datasets

To maintain consistency with previous modeling investigations, we use geothermal heat flux and surface temperature datasets provided as part of the SeaRISE project as reference boundary conditions.

The SeaRISE project offers magnetic- and seismic-based geothermal heat flux datasets [*Shapiro and Ritzwoller*, 2004; *Fox Maule et al.*, 2009]. We choose the seismic-based dataset in the present study as these heat flux values (56-65 mW m^{-2} across the study area) generally constitute the lowest values of the seismic, magnetic, or tectonic-based models common to the GrIS. Because the measurement-derived field we impose as an alternative GHF is lower than this reference dataset (see Results), interpretations based on this comparison are also valid with respect to warmer GHF products.

The reference surface temperature field is defined by the Regional Climate Model (RCM) RACMO mean annual surface temperature, which is temporally averaged over the period 1958-2007 [*Ettema et al.*, 2009]. RACMO output represents temperature at the ice/snow surface, preventing temperatures from warming above 0°C.

2.3 Measurements and observation-based boundary parameterization

2.3.1 Temperature measurements in the ablation zone

During the 2011 field campaign we drilled 20 m boreholes at two sites below the ELA using hot water methods, and instrumented these holes with data logging thermistor strings (Figure 1). We use 32 temperature sensors, spaced every 0.6 m to a maximum depth of 20 m below the surface, and capture measurements at 1 to 3 hour intervals. Temperature time series in the holes shows the thermal disturbance from drilling is effectively eliminated within 2-3 weeks of drilling. Temperature sensors and data loggers are identical to those used by Humphrey et al [2012]. We performed a zero point calibration in the field, and conservatively estimate the accuracy at 1.0°C. To account for large changes in surface elevation associated with seasonal ablation (approaching 3 meters per year (m a^{-1})) we adjust sensor depth below the ice surface using acoustic depth rangers from on-ice met stations at each site. Temperatures are then binned in 0.6 m increments. We report temperatures measured over a 15 month period from 7/2011 to 10/2013 at site GL11-S1. At the upper site, GL11-S2, instrument malfunction resulted in a 5 month measurement record from 7/2011 to 12/2011.

2.3.2 Observation-based boundary parameterization

As opposed to comparing uncertainties based on existing basal boundary datasets [*Rogozhina et al.*, 2012], or parameterizing surface temperatures based on approximations to physical processes [*Reeh*, 1991; *Phillips et al.*, 2010], we address the effects of boundary condition adjustments on ice sheet model output from an alternate approach. We compare standard boundary condition datasets with fields which we develop directly from measurements on the ice sheet. Doing so allows us to: 1) take advantage of the dense network of observations near our study area (compared to the rest of the GrIS), and 2) treat surface boundary condition changes across multiple glacier facies.

Direct measurements of GHF in bedrock boreholes and indirect measurements utilizing ice core temperatures bound our study region (Figure 1). Heat flux from temperature gradients in deep bedrock boreholes at two sites in southern Greenland ranges from 37 to 41.8 mW m^{-2} [*Sass et al.*, 1972]. A >300 m deep bedrock borehole has been drilled as part of the Greenland Analogue Project (GAP) adjacent to our model domain [*Harper et al.*, 2010]. Temperature gradients in this hole yield a GHF value of 34.8 mW m^{-2}. In 2011, an additional 700 m bedrock borehole was drilled under the same project, terminating under the ice sheet in our model domain. Measurements in this hole, the presentation and detailed analysis of which is forthcoming [*Claesson Liljedahl L. et al.*, in preparation], indicate a GHF of 27.2 mW m^{-2}. We note that GHF prescription as the mean of these two values has little effect on modeling results and interpretation, and use the lower GHF value in the deeper hole as it terminates under the ice sheet within our model domain. North of our model domain, Petrunin et al [2013] achieved tight model fits to measured temperature profiles at GISP2 and GRIP through coupling of lithospheric and ice sheet models with GHF values of approximately 60 and 61 mW m^{-2} respectively. We adopt these calculations at the ice core locations which bound our study domain to the north. In the absence of a more physically plausible method, we linearly interpolate between these five bounding values over the model domain (Figure 2).

Near-surface temperatures are limited above the ELA. Measurement availability in central-western Greenland was limited to a few measurements below 2000 m in previous efforts by Reeh [1991] to parameterize warming in the percolation zone. Since that study, 10 m temperatures were measured at 14 sites between 2007-2009 along the EGIG transect approximately 270 km north of our study area [*Humphrey et al.*, 2012]. We utilize these near-surface temperatures to parameterize warming effects in the percolation zone in our study region.

We parameterize the surface boundary temperature as a deviation from the reference case to preserve larger scale lapse rates and climatology embedded within the reference RCM. Temperature adjustments follow a heuristic, multi-part fit to honor the near-surface measurements. In order to effectively treat the difference in ELA position between the sites along the EGIG line, (estimated at 1100 m, near Swiss Camp [*Box et al.*, 2006]), and our study domain (~1550 m [*van de Wal et al.*, 2008]), we use the ELA as the reference elevation, and base the parameterization on the elevation above or below this reference point. Above the elevation of maximum temperature deviation in the percolation zone, differences between measured and reference temperatures are fit using an exponential function. Between the ELA and elevation of maximum deviation, the temperature difference between measured and the reference dataset follows a linear fit, assuming that the temperature deviation $dT = 0^{\circ}$C at the ELA.

Below the ELA we calculate the difference between our temperature measurements at depth and the reference temperature dataset and extrapolate this difference across the ablation zone using a second order polynomial from the ELA to the elevation of measurement site GL11-S1 (see Figure 1). Below this elevation, we maintain a constant temperature deviation to avoid imposing temperatures greater than 0°C. The parameterization of near-surface temperature across the entire domain is summarized by the workflow in Figure 3.

2.4 Ice Sheet Model

We implement numerical experiments using the VarGlaS ice sheet modeling framework. VarGlaS provides capabilities for three dimensional modeling of ice flow using finite elements under the premise of variational principles for the momentum balance [*Brinkerhoff and Johnson*, 2013]. The momentum balance satisfies the Blatter-Pattyn first-order equations [*Blatter*, 1995; *Pattyn*, 2003], assuming small bed slopes and negligible horizontal gradients in vertical velocity. Thermo-mechanical coupling is achieved using an enthalpy scheme. Internal heat sources in the enthalpy formulation are limited to strain heating, and additional heat is introduced at the basal boundary through frictional dissipation and geothermal heat flux. A complete description of the model formulation and numerics therein can be found in Brinkerhoff and Johnson [2013].

The surface boundary of the momentum balance is stress free, while the basal boundary employs a linear friction law with an impenetrability constraint. Zero gradients in stress are implied across the lateral boundaries and at the divide.

The surface boundary in the enthalpy scheme is a prescribed Dirichlet condition representing the mean annual near-surface temperature. Basal gradients in internal energy at the bed follow:

$$\kappa(H)\nabla H \cdot \mathbf{n} = h\beta^2 \mathbf{u_B} \cdot \mathbf{u_B} + q_{geo} - M_b \rho L \qquad (1)$$

where $\kappa(H)$ is an enthalpy-dependent diffusivity, H is enthalpy, h is ice thickness, β^2 is basal traction, $\mathbf{u_B}$ is the bed-parallel basal velocity vector, q_{geo} is geothermal heat flux, M_b is the basal melt rate, ρ the density of ice, and L is the latent heat of fusion for water.

A natural boundary along the lateral edges in the enthalpy formulation imposes an insulation condition. This condition is equivalent to Equation 1 with the right-hand side set to 0. Choosing the lateral boundaries of our model domain normal to surface elevation contours ensures model driving stress direction is tangential to these facets, minimizing thermal effects from advection across the lateral boundaries. At the ice sheet divide, we impose a 1-D temperature profile assuming a constant vertical strain rate [*Cuffey and Patterson*, 2010], and accumulation rate of $\dot{b} = 0.3ma^{-1}$ based on available GC-Net accumulation data [*Steffen et al.*, 1996].

A strength of the VarGlaS framework is the ability to assimilate observed surface velocities through adjoint-based techniques, which we use to find a steady state instance of the model. The objective function minimizes the logarithmic misfit between observed and modeled velocities subject to the forward model constraint. We choose a logarithmic cost functional to equitably distribute optimization effort across the full range of velocity magnitudes. Additionally, we address overfitting by imposing a Tikhonov regularization term which penalizes gradients in basal traction [*Gillet-Chaulet et al.*, 2012; *Seroussi et al.*, 2013]. The degree of regularization is a function of the ice sheet thickness and the tunable parameter α. This results in the following objective function to be minimized via a Quasi-Newton BFGS scheme [*Nocedal and Wright*, 2000]:

$$I = \int_{\Gamma_s} \left(\ln \frac{\left\| u_{sfc} \right\|}{\left\| u_{obs} \right\|} \right)^2 d\Gamma \ + \alpha h \int_{\Gamma_b} \left\| \nabla \beta^2 \cdot \nabla \beta^2 \right\| d\Gamma \ . \qquad (2)$$

Through the use of an L-curve analysis [*Aster et al.*, 2005], we choose $\alpha = 2$ (Figure 4). Experimentation with different degrees of regularization influences the velocity misfit but does not affect comparison of the experiments as described below. With the regularization parameter in hand, we iteratively update the momentum balance through variations in the basal traction parameter β^2 under constant viscosity and enthalpy, calculated from an initial steady state solution. Enthalpy and non-linear viscosity are updated every 50 iterations during the inversion process. Termination of the inversion is largely a qualitative process, previously referred to as the ‘recent improvement threshold’ approach [*Habermann et al.*, 2012]. Under this approach, we terminate the inversion when changes in the objective function between iterations become small. An alternative termination criteria (e.g. the discrepancy principle [*Habermann et al.*, 2012]), which takes in to account uncertainty in the surface velocity and elevation data as well as error associated with assumptions in the model formulation (e.g. first-order mechanics) may yield an improved solution but is beyond the scope of this study.

The model domain surface and bedrock topography are defined by a 1 km digital elevation model (DEM) [*Bamber et al.*, 2013]. We apply a Gaussian filter to the surface topography to eliminate locally sharp changes in the DEM’s representation of elevation. We consider this to be justified as the DEM is constructed from a combination of direct measurement and remotely sensed products over more than a decade, may contain artifacts from the merging of such data, and is prone to uncertainty from local averaging and interpolation. The unstructured model mesh is refined following the Hessian of the observed velocity field [*Brinkerhoff and Johnson*, 2013], resulting in mesh spacing ranging from <2 km to 10km. The final model mesh consists of 10 evenly spaced vertical layers and 31,108 nodal points. SAR-based velocity observations for the 2008-2009 period [*Joughin et al.*, 2010] are nearly complete over the study region and guide the mesh refinement denoted above, as well as the data assimilation target. A region of the model domain near the divide lacks velocity observations and is filled with balance velocities. We smooth the transition between observational and balance velocity to reduce numerical artifacts during assimilation.

2.5 Model Experimental Design

We perform three different modeling experiments to investigate sensitivity to thermal boundary condition adjustments. Experiment E-REF is forced at the surface and bed by the reference datasets and provides baseline results for comparison. With these boundaries we assimilate surface velocity observations to arrive at a basal traction field which minimizes the velocity misfit as described above. In order to isolate dynamic effects from boundary condition changes alone, we maintain this same traction field through each subsequent experiment. In the second experiment (E-GHF), we keep the reference surface boundary condition but change the geothermal heat flux based on available measurements. In the final experiment (E-FULL), both the surface and basal enthalpy boundaries are adjusted based on measurements. We focus on temperature output from the steady state model as a metric of comparison between these three experiments.

3 Results

3.1 Measurements

3.1.1 Geothermal heat flux

Measurements at the GAP borehole site adjacent to the model domain is less than half of the reference dataset (Figure 1). To the north, modeled GHF values at GISP and NGRIP are 10 mW m^{-2} higher than the Shapiro and Ritzwoller [2004] model, but the linearly interpolated field is everywhere lower across the model domain (Figure 2). Interpolated values range from 27 mW m^{-2} near the ice sheet margin to 49 mW m^{-2} at the divide and are, on average, 23 mW m^{-2} less than the reference field.

3.1.2 Surface temperature

Our measurements in the ablation zone show large seasonal variability in temperature in the upper 8 m at both sites and down to ~15 m depth at site GL11-S1 (Figure 5). Temperatures at 20 m depth from both sites show limited fluctuations and are significantly warmer than the reference counterpart. At lower site GL11-S1, the difference between measurement and the reference temperature is 10°C. At upper site GL11-S2 we measure a smaller temperature difference, but measured temperatures remain 5°C warmer than the reference dataset. As detailed by Humphrey et al [2012], warming in the near surface firn layer can be substantial due to latent heat release. Measured temperatures deviate from the RACMO surface reference by up to 15°C (Figure 5). Even at Crawford Point, the highest field site in the Humphrey et al study, measured temperatures deviate from the reference dataset by 3°C. Temperature differences between the reference surface temperature output and our observation-based field reach 14°C, and on average the data-constrained scheme is nearly 6°C warmer over the model domain (Figure 2).

3.2 Modeling

3.2.1 E-REF results

Results from the assimilation procedure are presented in Figure 6. High traction values generally limit modeled sliding above the ELA. Exceptions close to the divide typically correspond to areas where velocity observation uncertainty increases or where balance velocity fills observational gaps. A drop in driving stress from relaxation of surface slopes near the approximate ELA forces a reduction in basal traction and, correspondingly, a sharp increase in modeled sliding velocity. Maximum surface velocities reach >250 m a^{-1} in the ablation zone but are generally constrained to 90-110 m a^{-1}. The resulting RMSE between modeled and observed surface velocity is 3.8 m a^{-1} with a maximum deviation of 27 m a^{-1}.

The basal thermal field under reference boundary conditions shows temperate conditions across nearly the entire model domain (Figure 7). At the ice sheet divide basal conditions transition from temperate to -10°C. This variability results from the basal heat flux field, which increases from north to south along the divide, as well as ice thickness changes which vary by 300 m. Along the ice sheet margin, a rim of frozen conditions exists where ice is thin and conductive losses are greatest.

3.2.2 E-GHF results

Reducing geothermal heat flux with the observation-based field invokes strong changes in the basal thermal regime near the ice sheet divide and margin. Frozen conditions are consistent along the divide and extend towards the ice sheet margin before modeled basal ice reaches the pressure melting point (Figure 7). Near the margin, reduced heat flux increases the extent of frozen conditions compared to E-REF. Basal temperatures below the pressure melting point extend >50 km from the ice sheet terminus. The pattern of frozen and temperate conditions is strongly controlled by bedrock topography, with the coldest regions corresponding to topographic highs, and correspondingly thinner ice.

3.2.3 E-FULL results

Near the ice sheet divide, the pattern of thermal conditions at the bed resulting from data-driven surface and basal boundary conditions do not differ substantially from E-GHF results. However, because the imposed surface temperature parameterization scheme generates temperatures at the ice sheet divide slightly warmer than the reference dataset (<2°C), these warmer temperatures are realized by a slight increase in basal temperatures and corresponding expansion of temperate conditions. Approaching the ice sheet margin, changes in surface temperature invoke significant warming at the bed. Frozen conditions, with temperatures reaching -5° to -10°C at the bed under E-REF and E-GHF are largely eliminated. A closer look at temperatures through the ice column reveals propagation of surface temperature disturbances to depth (Figure 8). Much of the heat lost through reductions in basal heat flow appears to be recovered by warming at the surface.

3.3 Comparison against measured temperature profiles

We stress that the objective in comparing model results to measured temperature profiles is not to achieve a perfect match, which would amount to a tuning exercise and is not the goal of the study. A detailed account of processes necessary to achieve the measured temperature profiles has been undertaken by the authors [*Harrington et al.,* submitted]. Instead, the objective of the comparison is to support or refute the consequences of changing model boundaries by placing results in an observational context against independent measurements through the full ice column.

Model experiments under reference surface boundary temperatures (E-REF and E-GHF) consistently indicate temperatures in the upper reaches of the ice column which are substantially colder than measured (Figure 9). The depth to which this cold bias propagates varies depending on the borehole in question and the heat flux prescribed. Reducing geothermal heat flux consistent with measurements (E-GHF) forces modeled temperatures which are even colder. The model cold bias reaches values up to 7°C below the ice surface. We observe temperate conditions at the bed in all holes for which we have measurements (GL11-S1, GL12-S2, GL11-S2), yet modeled basal temperatures at these sites are -3°C or colder under E-GHF.

The added heat at the surface in E-FULL has a large impact on temperatures through the entire ice column. Compared to E-GHF, ice temperatures at each of the measurement sites are warmer by at least 3°C through the ice column. In the upper half of the ice column, removal of the cold bias from a warmer surface condition generates a closer fit to measurements, although modeled ice temperatures generally remain colder than measured. This result is expected considering the likely warming effect of macro-scale hydrologic features such as moulins and shallow crevasses [*Harrington et al., submitted*], which are not explicitly accounted for in our thermodynamic model. In the lower half of the ice column, results are mixed. The profile of the temperature curve towards the bed is quite similar to that from E-REF, despite significantly reduced basal heat flux. Model temperatures are warmer than measurements at both GL10-S3 and GL11-S2 but remain too cold at GL11-S1.

4 Discussion

We begin by assessing the limitations of the model experiments in terms of both the boundary condition parameterization and numerical model mechanics. We subsequently discuss the experiment results in the context of implications for ice sheet modeling efforts.

4.1 Assumptions and limitations

Our basal heat flux parameterization is no doubt a simplification of real-world fluxes beneath the ice sheet where local spatial variability is likely present [*Näslund et al.*, 2005; *Buchardt and Dahl-Jensen*, 2007]. However, there is no existing evidence for large spatial gradients in heat flux in our study region, and such gradients are also limited in the reference dataset, which was constructed on a 2°x2° grid. Other anecdotal evidence exists which supports the low GHF values we prescribe. While recent conclusions have suggested a thin lithosphere in central and northern GrIS [*Petrunin et al.*, 2013], interpretations of S-receiver functions suggest increasing lithosphere thickness by up to 50% further south on the ice sheet, as well as from east to west [*Kumar et al.*, 2005]. This spatial pattern is consistent with other work suggesting thicker lithosphere in central-southwestern Greenland associated with old, stable lithosphere [*Darbyshire et al.*, 2004]. Thick lithosphere is correlated with lower geothermal heat flux as it decreases the thermal gradient through a thicker bedrock layer. Additional evidence for decreased GHF values in southern GrIS stems from previous ice sheet modeling investigation by Greve [2005], who found it necessary to reduce GHF to 20 mW m^{-2} at the Dye 3 site in order to fit the modeled basal temperature to that measured in the ice core. The latter study supports our low GHF, but this result is not included in our measurement-driven field because of compounding uncertainty of past temperatures and precipitation rates on fitting Dye 3 basal conditions [*Dahl-Jensen et al.*, 1998; *Rogozhina et al.*, 2012].

The discrepancy between mean annual surface temperature from the reference RCM and measurements is clear, justifying a more plausible surface boundary that incorporates the warming effects from meltwater refreezing and other features near the surface such as crevasses. Seasonal melting in the percolation zone responsible for the warming effects parameterized in this study may exhibit variability on the order of years to decades, but model propagation of surface temperatures to depths of a few hundred meters requires centuries. This discrepancy in time scales suggests that the surface boundary in a steady state model may be more appropriately reflected by near surface warming that is more spatially broad, albeit diffuse in magnitude. However, measurements by Humphrey et al [2012] provide supporting evidence for persistent thermal perturbations, as 10 m temperature changed only a few degrees (generally small compared to the temperature deviation calculated here) over three years with very different melt conditions. Furthermore, sensitivity testing over a range of surface temperature perturbations shows an approximately linear relationship between the magnitude of perturbation and the resulting area of frozen bed conditions in the ablation zone. Thus, even small deviations from standard, model-based surface temperature datasets have a measurable impact on modeled basal conditions.

Interpretation of any model results hinges on assumptions and limitations within the numerical model. Our assumption of steady state and neglect of historical climate change is a significant but necessary constraint under the current assimilation method. Other uncertainties in the modeling experiments are present in the description of deformation, where we assume a stress exponent of $n = 3$ and have not prescribed enhanced deformation. Finally, local averaging and interpolation inherent in the surface and bed DEMs result in a geometry which introduces error in state variables.

The combined effect of these limitations may lead to a flow field and thermal profile which are inconsistent with present day observations. Unfortunately, many of the limitations described above are common to all numerical ice sheet models. Realistic treatment of constitutive processes requires in-situ measurements which are scarce. Topography over much of the current study area is constrained by dense airborne radar which is nearly unparalleled across the ice sheet. While the assumption of steady state may be alleviated by the use of a glacial spin-up, this introduces new uncertainty regarding historical temperature, mass balance, and temporal changes in basal sliding. We thus acknowledge the limitations of our numerical study, but assert that the modeling tools are commensurate with the current state of the art in ice sheet modeling practice.

4.2 Boundary condition impacts on numerical modeling

In the lower half of the ablation zone our model results using the Shapiro and Ritzwoller geothermal heat flux (E-REF) retain a rim of cold basal conditions which becomes pervasive with a decreased GHF commensurate with observations (E-GHF). This generates physically inconsistent model results, with basal slip reaching tens of m a^{-1} despite the frozen conditions. Cold based sliding has some precedence; Echelmeyer and Wang [1987] observed basal sliding at the ice-rock interface under cold conditions. Cuffey et al [1999] measured cold-based sliding at -17°C. However, the physical setting of these measurements at the ice terminus, and magnitude of observed sliding (10^{-4} – 10^{-1} m a^{-1}) are at odds with our model results, which show much faster sliding speeds far from the terminus. More importantly, direct measurement of basal temperature in our boreholes (Figure 9) and nearby observations of subglacial water issuing from the ice sheet terminus [*Bartholomew et al.*, 2011] indicate temperate basal conditions at least dominate in the lower ablation zone.

Unique basal heat flow measurement in our study area is less than half of standard datasets, but our modeling results honoring this data generate fast sliding over a frozen bed which is physically untenable. This suggests that there are one or more missing heat sources in the current model formulation. Macro-scale hydrologic features extending through the full ice thickness, such as moulins or crevasses, have been implicated to match temperature profiles elsewhere on the GrIS [*Phillips et al.*, 2010] and to explain changes in surface velocity along the EGIG transect [*Phillips et al.*, 2013]. Worldview imagery and on-the-ground investigation suggests that, while regions of crevassing are evident [*Harrington et al,* submitted], widespread crevassing through the ablation zone in our study area is not as pervasive as the previously investigated counterpart to the north. Nevertheless, while the existence of a continuous, high-density fracture network throughout our model domain is unsupported, localized crevasse fields or discrete features with large spacing likely have an integrated effect on temperature as ice is advected through or near them over time.

The frictional dissipation of heat from water flowing through an active basal drainage system may provide an additional heat source at the ice sheet bed not accounted for in the model. A strong seasonal melt cycle is present in the region, which has been the recent focus of numerous investigations on basal hydrology and impact of surface-to-bed routing of meltwater on seasonal velocity [*Sundal et al.*, 2011; *Bartholomew et al.*, 2012]. While this source no doubt releases significant heat at the ice/bedrock interface, the heat release is limited to the basal plane. Recent work has suggested that basal crevassing extends the thermal perturbation from basal water into the third dimension within the ice column [*Harrington et al,* submitted], but our model results under scenario E-GHF are consistently colder than measurements (Figure 9) through the entire ice column, suggesting more spatially distributed heating is necessary.

We do not explicitly rule out either of the additional heat sources described above, which no doubt play an important role in the heat budget of the model domain and are likely responsible for explaining key features in observed profiles [*Harrington et al,* submitted]. However, our results show that adjustment of near-surface temperatures alone in accordance with measurements is also sufficient to reverse a substantial portion of the apparent cold bias when using model-based surface temperatures. Temperature adjustments in the percolation zone propagate to depth, and while they don't have an impact on the already temperate basal conditions above the ELA, conductive heating reduces the cold temperatures from deeper in the ice sheet interior. The effect of this warming is realized in the ablation zone, where strong temperature gradients in thinner ice are reduced, and the destruction of the interior cold plug limits advective effects from ice flow around complex basal topography.

Our results reveal that the surface boundary condition is a key component of the modeled thermal budget whose importance is likely to be magnified in the southern portion of the GrIS where there is evidence for reduced heat flux from below and surface melting effects are amplified compared to elsewhere on the GrIS. Model simulations show that, integrated across the domain, the energy addition from surface boundary changes is over three times larger than the energy lost from reduced basal heat flux. As highlighted by the recent discovery of perennial liquid water under cold conditions in the percolation zone [*Forster et al.*, 2014], significant limitations remain with respect to our understanding of meltwater generation and routing processes on the ice sheet. Thermal effects do not appear to be limited to shallow depths, implying that, in addition to influencing mass balance uncertainties [*Harper et al.*, 2012], meltwater storage and refreezing may also be an important contributing factor to the ice sheet thermal profile, albeit given sufficient time scales.

5 Conclusions

In this study we have leveraged measurements near the ice sheet surface, below the ice sheet bed, and within the ice column to develop new observationally constrained boundary conditions and assess the subsequent impact of these new fields on modeled thermal behavior over a study reach in western GrIS. Measurements at the ice sheet surface and bed indicate a relative reversal in energy contribution compared to reference temperature and GHF datasets. Whereas commonly used, spatially distributed fields prescribe high heat flux and low surface temperatures through our study area, measurements reveal the opposite. Surface temperatures in both the percolation and ablation zones are measured to be 10°C warmer or more than reference output. Conversely, existing observations indicate geothermal heat flux <50% of that commonly prescribed.

The realization of boundary condition discrepancies between measurements and spatially distributed datasets in a higher order ice dynamical model indicates that the boundary conditions are first-order drivers of the ice sheet thermal profile. Reduction of geothermal heat flux alone commensurate with observation increases the modeled cold bias compared to measured temperature profiles and frozen basal conditions through the ablation zone. The recovery of warm conditions in the ablation zone under observation-based surface conditions and large internal energy addition to the domain in model simulations suggests near-surface effects cannot be ignored in thermo-mechanically coupled model experiments.

The future behavior of the Greenland ice sheet remains poorly constrained, due in part to a limited understanding of the expected basal sliding response to climate changes. In the absence of a universal sliding law, the assessment of future ice sheet behavior has been accomplished through sliding amplification experiments, whereby initial sliding conditions are multiplied by a constant amplification factor [*Bindschadler et al.*, 2013; *Nowicki et al.*, 2013]. Model-based tuning of basal traction to match observed velocities is prone to thermally induced biases which influence internal deformation, and hence sliding/deformational velocity partitioning. Our results indicate that the surface and basal boundary conditions critically dictate thermal behavior through the full ice thickness, necessitating careful consideration during such model initialization. Cold model conditions from inadequate treatment of effects near the surface may thus be manifested in the velocity regime through enhanced sliding, which is amplified in modeled future ice sheet behavior when this initial sliding condition is perturbed.

6 Acknowledgements

This work is funded by SKB-Posiva-NWMO through the Greenland Analogue Project and NSF (Office of Polar Programs-Arctic Natural Sciences grant no. 0909495). We thank L. Claesson Liljedahl and J. O. Näslund for their careful critiques which substantially improved an earlier version of the manuscript. Datasets will be published by the Swedish Nuclear Waste Management Company in Fall, 2014 at the following web address: http://www.skb.se/Templates/Standard____17139.aspx.

7 References

Aster, R. C., B. Borhers, and C. H. Thurber (2005), *Parameter Estimation and Inverse Problems*, Elsevier Academic Press, San Diego, CA.

Bamber, J. L. et al. (2013), A new bed elevation dataset for Greenland, *Cryosph.*, *7*(2), 499–510, doi:10.5194/tc-7-499-2013.

Bartholomew, I., P. Nienow, A. Sole, D. Mair, T. Cowton, S. Palmer, and J. Wadham (2011), Supraglacial forcing of subglacial drainage in the ablation zone of the Greenland ice sheet, *Geophys. Res. Lett.*, *38*(8), 1–5, doi:10.1029/2011GL047063.

Bartholomew, I., P. Nienow, A. Sole, D. Mair, T. Cowton, and M. a. King (2012), Short-term variability in Greenland Ice Sheet motion forced by time-varying meltwater drainage: Implications for the relationship between subglacial drainage system behavior and ice velocity, *J. Geophys. Res.*, *117*(F3), 1–17, doi:10.1029/2011JF002220.

Benson, C. S. (1962), Stratigraphic Studies in the Snow and Firn of the Greenland Ice Sheet. *Res. Rep. 70,* 183 pp., Snow, Ice and Permafrost Res. Estab., U. S. Army Corps of Eng., Hanover, N. H.

Bindschadler, R. A. et al. (2013), Ice-sheet model sensitivities to environmental forcing and their use in projecting future sea level (the SeaRISE project), *J. Glaciol.*, *59*(214), 195–224, doi:10.3189/2013JoG12J125.

Blatter, H. (1995), Velocity and stress fields in grounded glaciers; a simple algorithm for including deviatoric stress gradients, *J. Glaciol.*, *41*(138), 331–344.

Box, J. E., D. H. Bromwich, B. A. Veenhuis, L. S. Bai, J. C. Stroeve, J. C. Rogers, K. Steffen, T. Haran, and S. H. Wang (2006), Greenland Ice Sheet Surface Mass

Balance Variability (1988 – 2004) from Calibrated Polar MM5 Output *, *J. Clim.*, *19*, 2783–2800.

Brinkerhoff, D. J., and J. V. Johnson (2013), Data assimilation and prognostic whole ice sheet modelling with the variationally derived, higher order, open source, and fully parallel ice sheet model VarGlaS, *Cryosph.*, *7*(4), 1161–1184, doi:10.5194/tc-7-1161-2013.

Buchardt, S. L., and D. Dahl-Jensen (2007), Estimating the basal melt rate at NorthGRIP using a Monte Carlo technique, *Ann. Glaciol.*, *45*(1), 137–142, doi:10.3189/172756407782282435.

Cuffey, K. M., and W. S. B. Patterson (2010), *The Physics of Glaciers*, 4th ed., Elsevier, Oxford.

Cuffey, K. M., H. Conway, B. Hallet, A. M. Gades, and C. F. Raymond (1999), Interfacial water in polar glaciers and glacier sliding at -17 degC, *Geophys. Res. Lett.*, *26*(6), 751–754.

Dahl-Jensen, D., K. Mosegaard, N. Gundestrup, G. D. Clow, S. J. Johnsen, A. W. Hansen, and N. Balling (1998), Past Temperatures Directly from the Greenland Ice Sheet, *Science*, *282*(5387), 268–271, doi:10.1126/science.282.5387.268.

Darbyshire, F. a., T. B. Larsen, K. Mosegaard, T. Dahl-Jensen, Ó. Gudmundsson, T. Bach, S. Gregersen, H. a. Pedersen, and W. Hanka (2004), A first detailed look at the Greenland lithosphere and upper mantle, using Rayleigh wave tomography, *Geophys. J. Int.*, *158*(1), 267–286, doi:10.1111/j.1365-246X.2004.02316.x.

Echelmeyer, K., and W. Zhongxiang (1987), Direct observation of basal sliding and deformation of basal drift at sub-freezing temperatures, *J. Glaciol.*, *33*(113).

Echelmeyer, K., W. D. Harrison, T. S. Clarke, and C. Benson (1992), Surficial glaciology of Jakobshavns Isbrae, West Greenland: Part II. Ablation, accumulation and temperature, *J. Glaciol.*, *38*(128), 169–181.

Ettema, J., M. R. van den Broeke, E. van Meijgaard, W. J. van de Berg, J. L. Bamber, J. E. Box, and R. C. Bales (2009), Higher surface mass balance of the Greenland ice sheet revealed by high-resolution climate modeling, *Geophys. Res. Lett.*, *36*(12), L12501, doi:10.1029/2009GL038110.

Forster, R. R. et al. (2014), Extensive liquid meltwater storage in firn within the Greenland ice sheet, *Nat. Geosci.*, *7*, 95–98, doi:10.1038/ngeo2043.

Gillet-Chaulet, F., O. Gagliardini, H. Seddik, M. Nodet, G. Durand, C. Ritz, T. Zwinger, R. Greve, and D. G. Vaughan (2012), Greenland ice sheet contribution to sea-level rise from a new-generation ice-sheet model, *Cryosph.*, *6*(6), 1561–1576, doi:10.5194/tc-6-1561-2012.

Greve, R. (2005), Relation of measured basal temperatures and the spatial distribution of the geothermal heat flux for the Greenland ice sheet, *Ann. Glaciol.*, *42*(1), 424–432, doi:10.3189/172756405781812510.

Habermann, M., D. Maxwell, and M. Truffer (2012), Reconstruction of basal properties in ice sheets using iterative inverse methods, *J. Glaciol.*, *58*(210), 795–807, doi:10.3189/2012JoG11J168.

Harper, J. et al. (2010), *The Greenland Analogue Project Yearly Report 2010. R-11-23.*, Svensk Karnbranslehanterin AB.

Harper, J., N. Humphrey, W. T. Pfeffer, J. Brown, and X. Fettweis (2012), Greenland ice-sheet contribution to sea-level rise buffered by meltwater storage in firn, *Nature, 491*(7423), 240–243, doi:10.1038/nature11566.

Hooke, R. L., J. E. Gould, and J. Brzozowski (1983), Near-surface temperatures near and below the equilibrium line on polar and subpolar glaciers, *Zeitschrift fur Gletscherkd. und Glazialgeol.*, *19*(1), 1–25.

Humphrey, N. F., J. T. Harper, and W. T. Pfeffer (2012), Thermal tracking of meltwater retention in Greenland's accumulation area, *J. Geophys. Res.*, *117*(F01010), 1–11, doi:10.1029/2011JF002083.

Jarvis, G. T., and G. K. C. Clarke (1974), Thermal effects of crevassing on Steele Glacier, Yukon Territory, Canada, *J. Glaciol.*, *13*(68), 243–254.

Joughin, I., B. E. Smith, I. M. Howat, T. Scambos, and T. Moon (2010), Greenland flow variability from ice-sheet-wide velocity mapping, *J. Glaciol., 56*(197), 415–430, doi:10.3189/002214310792447734.

Koenig, L. S., C. Miège, R. R. Forster, and L. Brucker (2013), Initial in situ measurements of perennial meltwater storage in the Greenland firn aquifer, *Geophys. Res. Lett., 41*, 1–5, doi:10.1002/2013GL058083.

Kumar, P. et al. (2005), The lithosphere–asthenosphere boundary in the North-West Atlantic region, *Earth Planet. Sci. Lett.*, *236*, 249–257, doi:10.1016/j.epsl.2005.05.029.

Larour, E., H. Seroussi, M. Morlighem, and E. Rignot (2012), Continental scale, high order, high spatial resolution, ice sheet modeling using the Ice Sheet System Model (ISSM), *J. Geophys. Res.*, *117*(F01022), 1–20, doi:10.1029/2011JF002140.

Fox Maule, C., M. E. Purucker, and N. Olsen (2009), Inferring magnetic crustal thickness and geothermal heat flux from crustal magnetic field models, *Danish Climate Centre Report 09-09*, Danish Meteorol. Inst., Copenhagen.

Meierbachtol, T., J. Harper, and N. Humphrey (2013), Basal drainage system response to increasing surface melt on the Greenland ice sheet., *Science*, *341*(6147), 777–779, doi:10.1126/science.1235905.

Mock, S. J., and W. F. Weeks (1965), The distribution of 10 meter snow temperatures on the Greenland ice sheet, *J. Glaciol.*, 23–41.

Näslund, J.-O., P. Jansson, J. L. Fastook, J. Johnson, and L. Andersson (2005), Detailed spatially distributed geothermal heat-flow data for modeling of basal temperatures and meltwater production beneath the Fennoscandian ice sheet, *Ann. Glaciol.*, *40*(1), 95–101, doi:10.3189/172756405781813582.

Nocedal, J., and S. J. Wright (2000), *Numerical Optimization*, 2nd ed., edited by T. V. Mikosch, S. M. Robinson, and S. I. Resnick, Springer, New York, NY.

Nowicki, S. et al. (2013), Insights into spatial sensitivities of ice mass response to environmental change from the SeaRISE ice sheet modeling project II: Greenland, *J. Geophys. Res. Earth Surf.*, *118*, 1025–1044, doi:10.1002/jgrf.20076.

Pattyn, F. (2003), A new three-dimensional higher-order thermomechanical ice sheet model: Basic sensitivity, ice stream development, and ice flow across subglacial lakes, *J. Geophys. Res.*, *108*(B8), 1–15, doi:10.1029/2002JB002329.

Petrunin, a. G., I. Rogozhina, a. P. M. Vaughan, I. T. Kukkonen, M. K. Kaban, I. Koulakov, and M. Thomas (2013), Heat flux variations beneath central Greenland's ice due to anomalously thin lithosphere, *Nat. Geosci.*, *6*(8), 1–5, doi:10.1038/ngeo1898.

Pfeffer, W. T., and C. S. Bretherton (1987), The effect of crevasses on the solar heating of a glacier surface, *Phys. Basis Ice Sheet Model.*, *170*, 191–205.

Phillips, T., H. Rajaram, and K. Steffen (2010), Cryo - hydrologic warming : A potential mechanism for rapid thermal response of ice sheets, *Geophys. Res. Lett.*, *37*(L20503), 1–5, doi:10.1029/2010GL044397.

Phillips, T., H. Rajaram, W. Colgan, K. Steffen, and W. Abdalati (2013), Evaluation of cryo-hydrologic warming as an explanation for increased ice velocities in the wet snow zone, Sermeq Avannarleq, West Greenland, *J. Geophys. Res. Earth Surf.*, *118*, 1241–1256, doi:10.1002/jgrf.20079.

Pollack, H. N., S. J. Hurter, and R. Johnson (1993), Heat Flow from the Earth's Interior: Analysis of the Global Data Set, *Rev. Geophys.*, *31*(3), 267–280.

Reeh, N. (1991), Parameterization of Melt Rate and Surface Temperature on the Greenland lce Sheet, *Polarforschung*, *5913*, 113–128.

Rignot, E., and J. Mouginot (2012), Ice flow in Greenland for the International Polar Year 2008-2009, *Geophys. Res. Lett.*, *39*(11), 1–7, doi:10.1029/2012GL051634.

Rogozhina, I., J. M. Hagedoorn, Z. Martinec, K. Fleming, O. Soucek, R. Greve, and M. Thomas (2012), Effects of uncertainties in the geothermal heat flux distribution on the Greenland Ice Sheet: An assessment of existing heat flow models, *J. Geophys. Res.*, *117*(F02025), 1–16, doi:10.1029/2011JF002098.

Sass, J. H., B. L. Nielsen, H. a. Wollenberg, and R. J. Munroe (1972), Heat flow and surface radioactivity at two sites in South Greenland, *J. Geophys. Res.*, *77*(32), 6435–6444, doi:10.1029/JB077i032p06435.

Seroussi, H., M. Morlighem, E. Rignot, a. Khazendar, E. Larour, and J. Mouginot (2013), Dependence of century-scale projections of the Greenland ice sheet on its thermal regime, *J. Glaciol.*, *59*(218), 1024–1034, doi:10.3189/2013JoG13J054.

Shapiro, N. M., and M. H. Ritzwoller (2004), Inferring surface heat flux distributions guided by a global seismic model: particular application to Antarctica, *Earth Planet. Sci. Lett.*, *223*, 213–224, doi:10.1016/j.epsl.2004.04.011.

Steffen, K., J. E. Box, and W. Abdalati (1996), Greenland Climate Network: GC-Net, *CRREL 96-27 Spec. Rep. Glaciers, Ice Sheets Volcanoes, trib. to M. Meier*, 98–103.

Sundal, A. V., A. Shepherd, P. Nienow, E. Hanna, S. Palmer, and P. Huybrechts (2011), Melt-induced speed-up of Greenland ice sheet offset by efficient subglacial drainage: Supplementary Information, *Nature*, *469*(7331), 521–4, doi:10.1038/nature09740.

Van de Wal, R. S. W., W. Boot, M. R. van den Broeke, C. J. P. P. Smeets, C. H. Reijmer, J. J. a Donker, and J. Oerlemans (2008), Large and rapid melt-induced velocity changes in the ablation zone of the Greenland Ice Sheet., *Science*, *321*(5885), 111–113, doi:10.1126/science.1158540.

8 Figures

Figure 1:

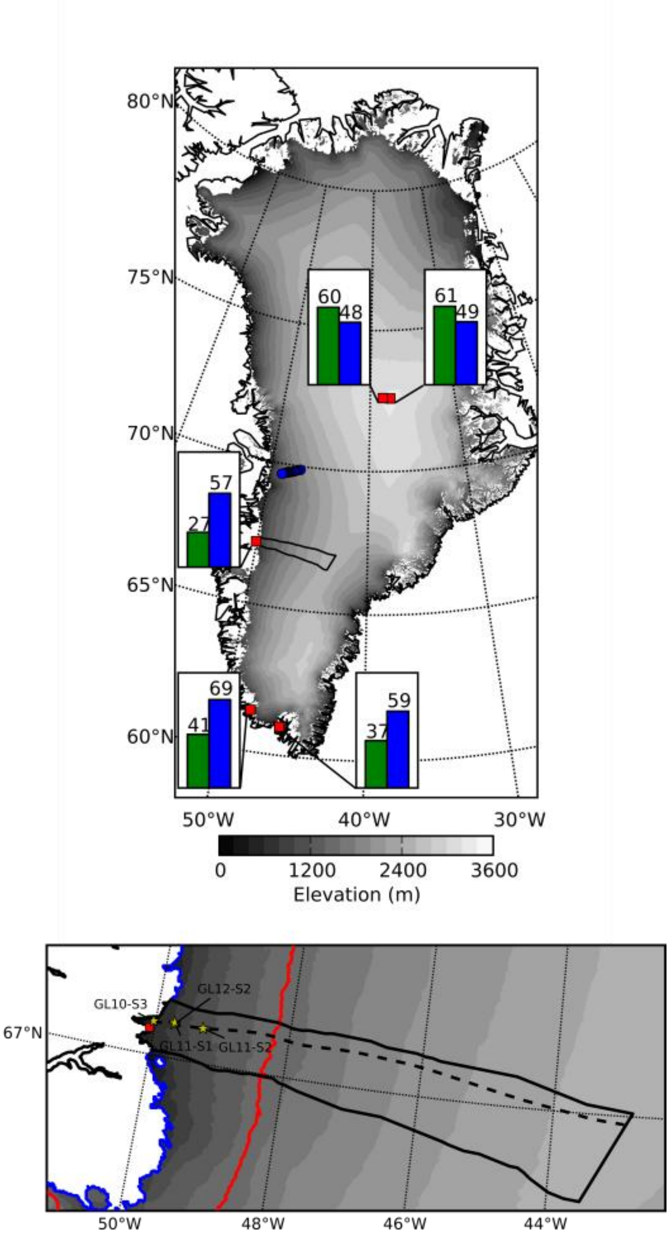

Figure 1: Study area in the context of the Greenland ice sheet. Model domain is outlined by the solid black line. Red squares show locations of geothermal heat flux measurements. Blue circles show locations of 10 m firn temperatures used for surface temperature adjustments. Bar charts display a comparison of Shapiro and Ritzwoller [2004] modeled geothermal heat flux (blue) against available direct and indirect measurements of heat flux (green), with heat flux values given in mW m^{-2}. Yellow stars in the inset show the locations of boreholes drilled during the 2010-2012 field seasons. Red line in the inset outlines the approximate ELA at 1550 m elevation. Dashed line in the inset shows the profile transect upon which Figure 8 is based. Surface elevation field is from Bamber et al [2013].

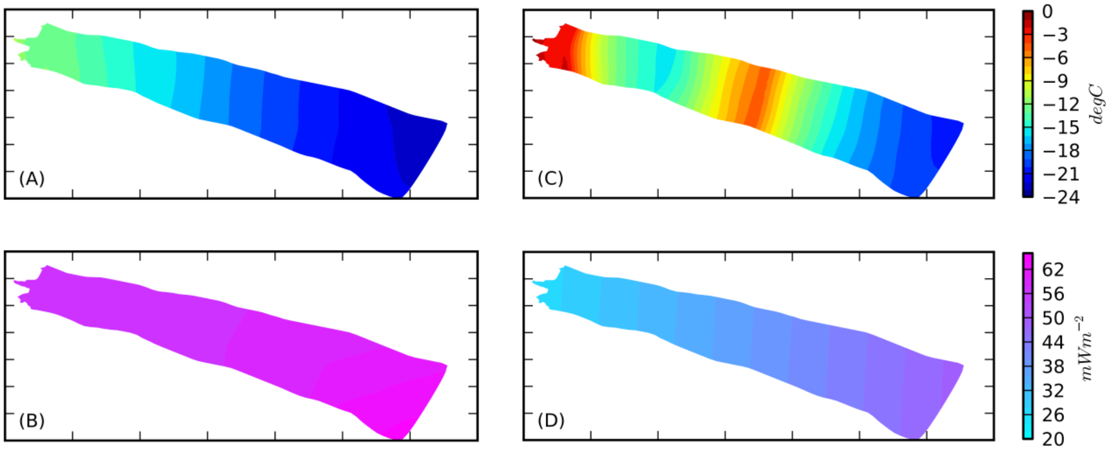

Figure 2: Reference boundary conditions (A and B) from the SeaRISE Project, and observation-driven boundary conditions (C and D). Surface temperatures are shown in (A) and (C), and geothermal heat flux fields are displayed in (B) and (D).

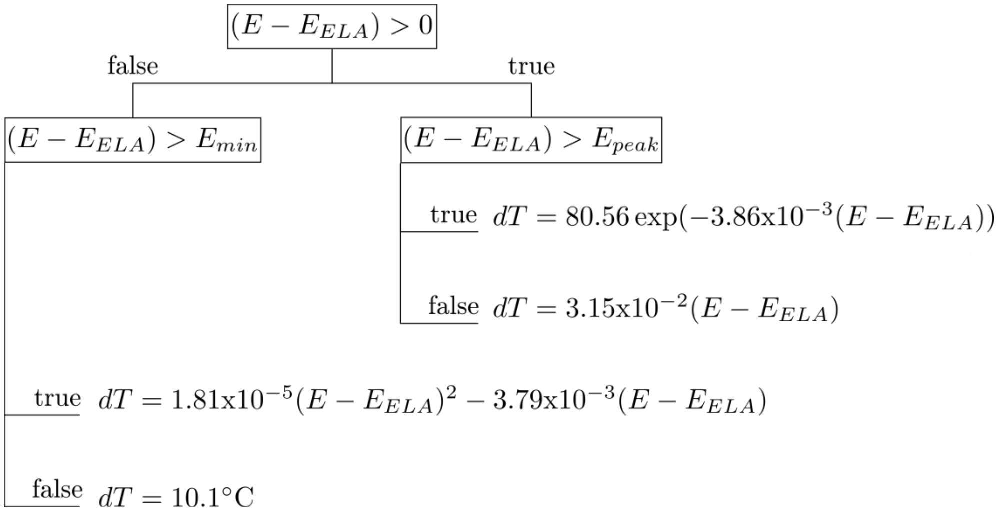

Figure 3: Workflow used for parameterizing the thermal surface boundary condition based on measurements. E is elevation, E_{ELA} is the elevation of the ELA as described in the text, $E_{\min}$ is the elevation of site GL11-S1, and E_{peak} is the elevation of peak temperature deviation, taken from the temperature measurements in the percolation zone (Figure 5). The resulting temperature deviation from the reference dataset is given by dT.

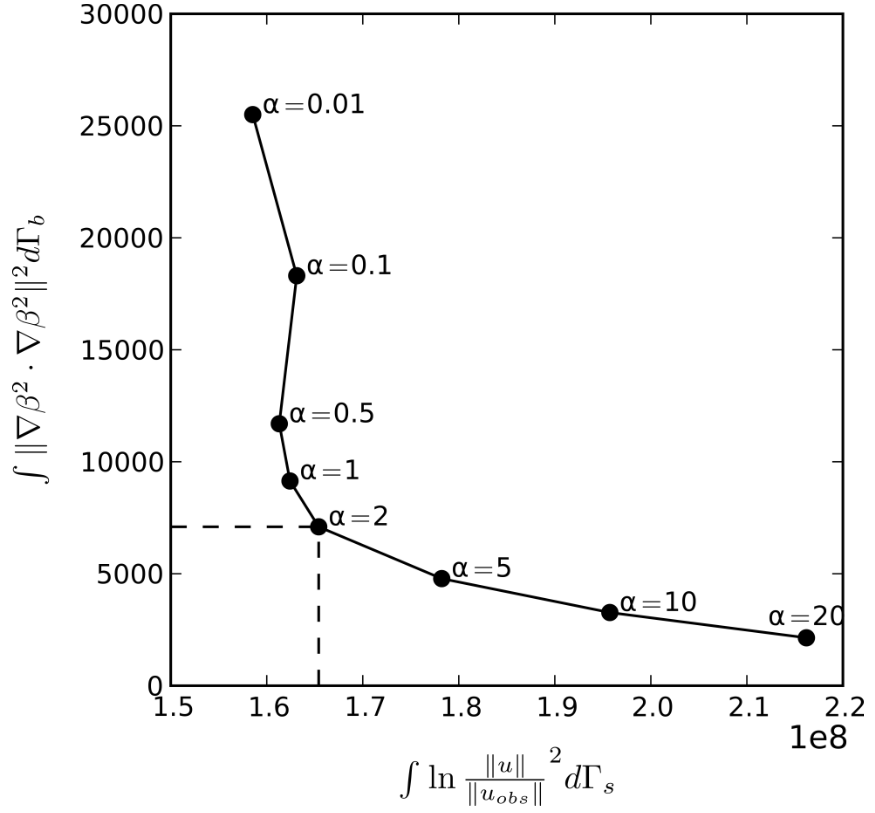

Figure 4: Results from the L-curve analysis used to constrain the regularization parameter α. A break in slope occurs at $\alpha = 2.0$, representing a reasonable compromise between the model norm ($\int_{\Gamma_b} \left\|\nabla\beta^2 \cdot \nabla\beta^2\right\|^2 d\Gamma$) and misfit norm ($\int_{\Gamma_s} \ln \frac{\|u_{\mathrm{mod}}\|}{\|u_{obs}\|}^2 d\Gamma$).

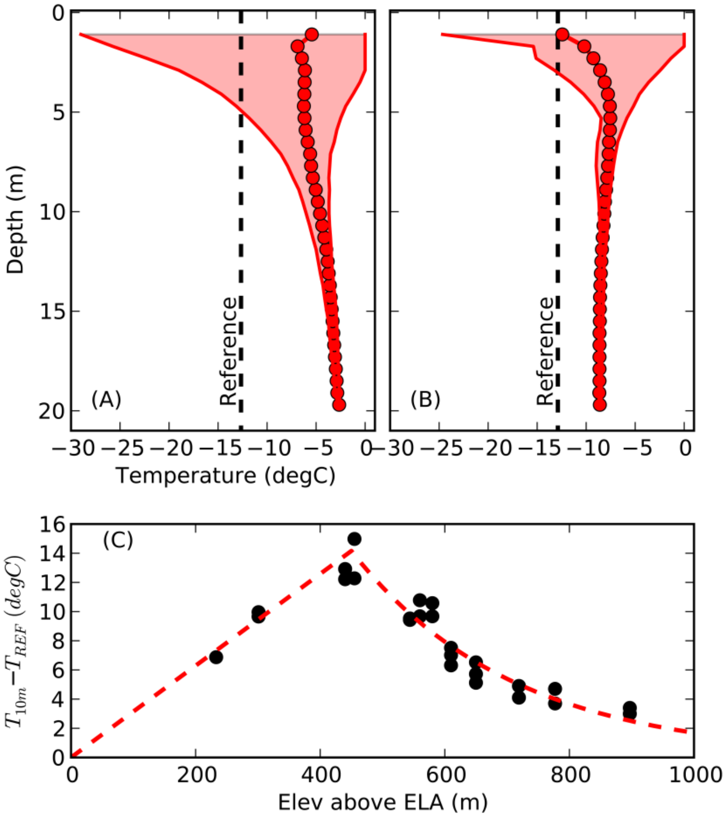

Figure 5: Measured temperatures used to construct the surface temperature field. Ablation zone measurements are shown at sites GL11-S1 (A) and GL11-S2 (B). Red dots show the ablation-corrected mean temperature over the measurement period, bounded by maximum and minimum measurements. Vertical, dashed black line shows the reference surface temperature at the location of the measurements. Difference between 10m temperatures measured by Humphrey et al [2012] and RACMO surface temperature is shown in (C) as a function of elevation above the ELA. Red curve shows the 2-part fit we use to scale temperature deviation to our model domain.

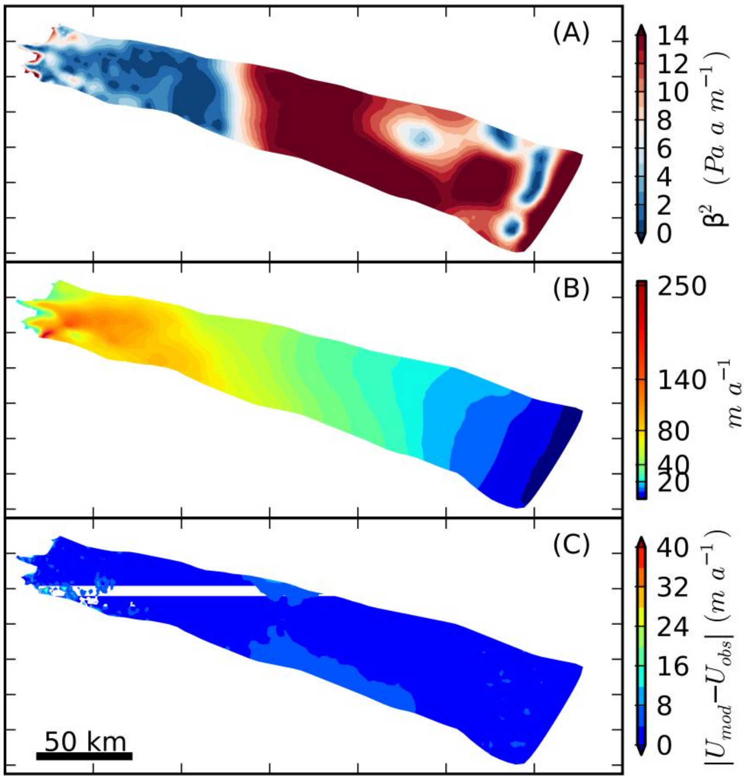

Figure 6: Results from the assimilation procedure to invert for β^2 (A). The resulting modeled surface velocity field is shown in (B) and the absolute difference between modeled and measured surface velocity is displayed in (C).

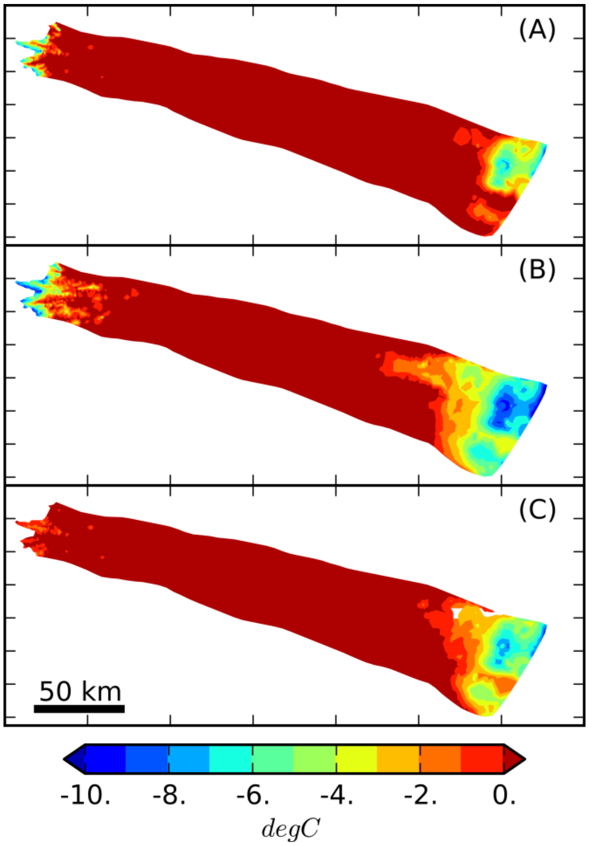

Figure 7: Modeled basal temperature results from the reference case E-REF (A), E-GHF (B), and E-FULL (C), with surface and basal boundaries constrained by data. Color bar is consistent across all three panels.

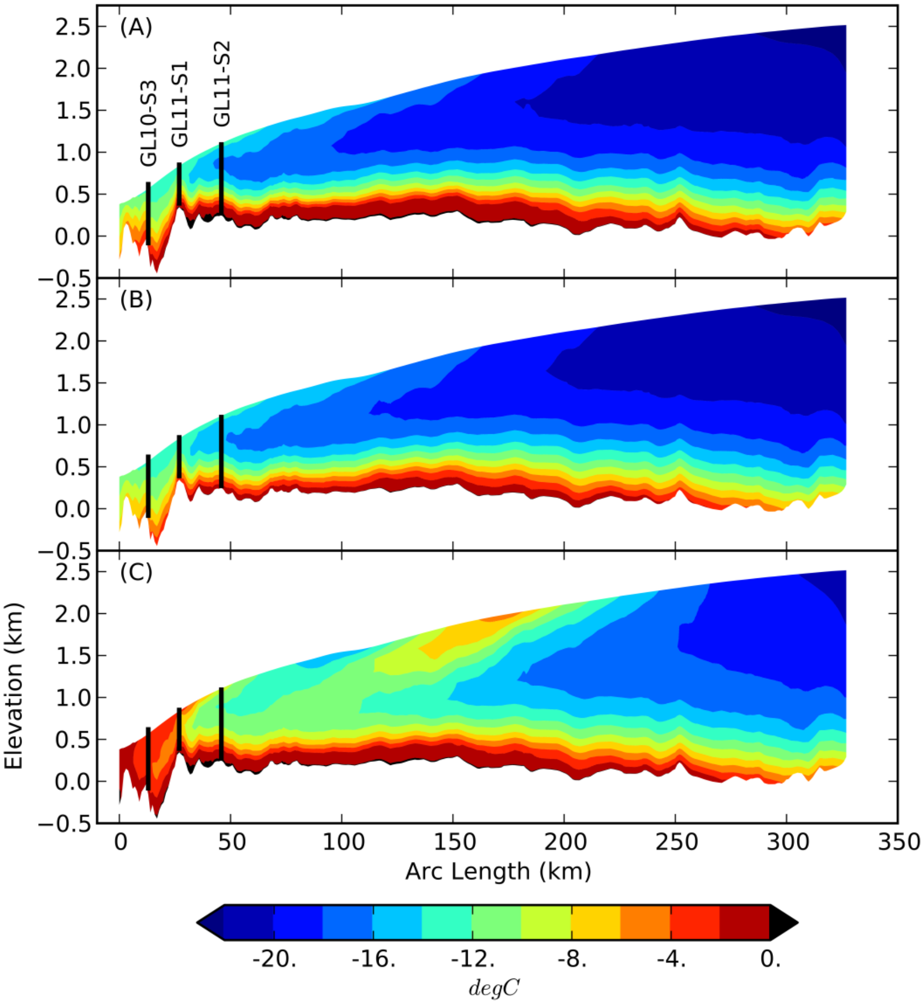

Figure 8: Temperature fields along a transect (see Figure 1) resulting from E-REF (A), E-GHF (B), and E-FULL (C). The color bar is consistent for each panel. Vertical bars denote locations, surface elevations, and bed elevations of boreholes shown in Figure 1.

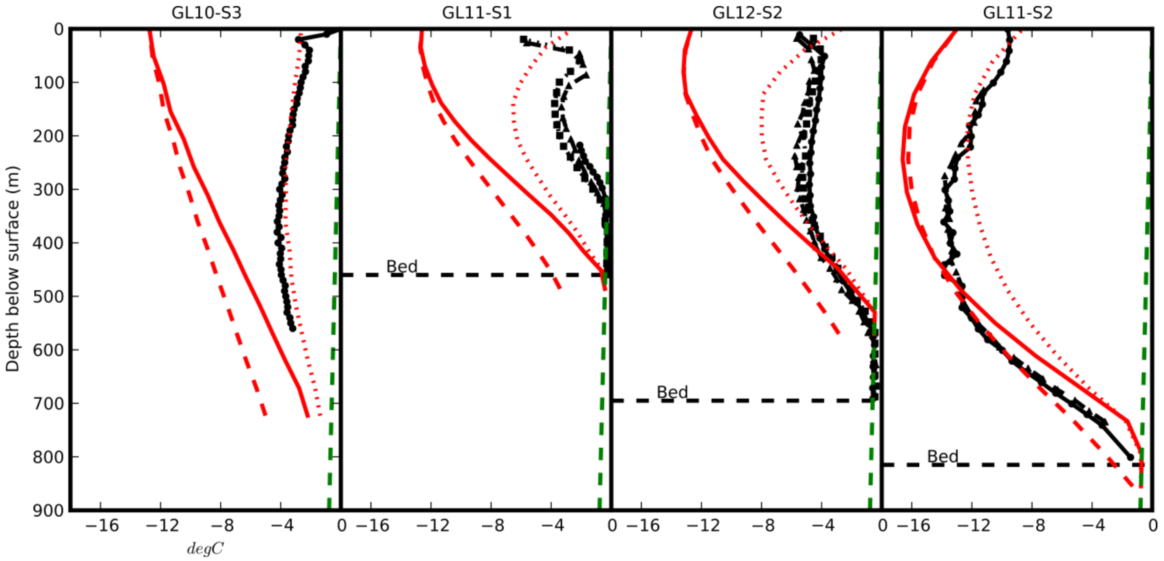

Figure 9: Measured and modeled temperatures at 4 sites in the ablation zone (see Figure 1). One to three temperatures strings were installed at each site, and are shown by black circles, squares, and triangles. Modeled temperatures from E-REF, E-GHF, and E-FULL are shown as solid, dashed, and dotted red lines respectively. Measured depth to the ice sheet bed during drilling is indicated by the horizontal, dashed black line (the bed was not reached in hole GL10-S3). The approximate pressure melting temperature is shown as the dashed green line.

CHAPTER 3

DYNAMICAL CONTROLS ON THE DRIVING STRESS ANOMALY IN WEST-SOUTHWEST GREENLAND

Abstract:

The west-southwest sector of Greenland is marked by a region of low driving stress associated with inflections in the ice sheet's surface profile. The driving stress anomaly (DSA) has a first-order influence on the partitioning between deformational and sliding motion. Previously, the DSA has been hypothesized to result from a bedrock plateau, but recent and more detailed radar bed imaging does not reveal a clear link between bedrock topography and the DSA's surface expression. Here we investigate alternative processes related to surface mass balance and ice flow dynamics which may explain this feature. Kinematic wave analysis indicates that transient surface perturbations rapidly recover over decades whereas the DSA has apparently been stable for longer. Further, the diffusive nature of the ice sheet precludes the possibility that the DSA results from remote or local perturbations in surface mass balance. Assessment of ice deformation suggests that observed surface speeds must be attributed to increasing basal motion across the DSA. We hypothesize that longitudinal variations in basal sliding are critical in the formation of the DSA by drawing down the surface elevation to maintain mass conservation. The colocation of the DSA with the equilibrium line altitude (ELA) suggests that introduction of surface-derived meltwater to the ice sheet bed provides a potential mechanism for initiating changes in basal motion.

INTRODUCTION

In recent years field research has focused on western Greenland (GrIS) to investigate the role of seasonal melt in forcing sliding perturbations (e.g. van de Wal and others, 2008; Bartholomew and others, 2012; Doyle and others, 2014). This sector of the ice sheet is largely land-terminating and undergoes considerable seasonal melting with measured ablation rates exceeding 5 m a^{-1} in places (van de Wal and others, 2012). This region is therefore a logical test bed to study the forcing and response between surface meltwater, basal hydrology, and ice dynamics without complications from marine effects. The interior of west-southwest (W-SW) Greenland, however, contains a driving stress reduction that is anomalous relative to the regional profile of the ice sheet (Figure 1). The gravitational driving stress is of primary order in dictating ice sheet motion. Further, changes in ice thickness and surface slope which define the driving stress are critical controls on subglacial hydrological dynamics as they influence the potential gradient driving water flow (Cuffey and Patterson, 2010). The direct coupling between driving stress and ice flow dynamics thus warrants investigation of the processes governing the driving stress anomaly within this test bed study region of the GrIS.

The reach of anomalously low driving stress in W-SW GrIS was originally identified, along with the northeast ice stream, to be unique features of the GrIS (Bamber and Layberry, 2001; Layberry and Bamber, 2001). Low driving stress in the northeast counterpart was attributed to a drop in basal topography, inception of streaming flow, and flattening of the ice sheet surface. The contrasting physical setting in W-SW GrIS without a dominant ice stream led the authors to attribute the low driving stress to a high (1000 m elevation), flat bedrock plateau (Layberry and Bamber, 2001).

Surface slope and thickness defining the ice sheet driving stress are complicated functions of processes not limited to basal topography alone. The magnitude of basal sliding complicates the surface expression of basal topography, enhancing the transmission efficiency and adjusting the phase shift at the surface to varying degrees depending on the wavelength of the basal disturbance (Gudmundsson, 2003; Raymond and Gudmundsson, 2005). Spatial variations in basal motion, manifested primarily as slipperiness perturbations, have also been shown theoretically to influence surface topography in the absence of a basal expression (Gudmundsson, 2003; Raymond and Gudmundsson, 2005). Such variability in stick-slip motion has recently been implicated in describing short wavelength driving stress anomalies on Greenland (Sergienko and others, 2014).

In addition to processes at the ice sheet bed, perturbations in surface processes may impose a control on the ice sheet's profile. The ice sheet is unlikely to ever attain a true steady state as it continuously adjusts to changes in mass balance and external forcings. Anomalous perturbations in surface mass balance could manifest themselves as transient waves in the surface profile of kinematic type (Nye, 1960, 1963a; b). Considering the large spatial extent of the ice sheet and relatively sparse (in both space and time) observational record, such a surface mass balance anomaly may not be clearly discernible from measurement.

Here we investigate each of the above mechanisms and assess their plausibility as a governing process forming the DSA. We revisit the original hypothesis by Layberry and Bamber (2001) with updated basal topography to address the likelihood that it results primarily from a consistent topographic high. Using kinematic wave theory, we investigate the ice sheet response to perturbations in mass balance to test the hypothesis that such surface anomalies can form directly from variations in accumulation and ablation. Finally, through comparison of a spectrum of reasonable deformational velocities with velocity observations through the DSA, we assess the plausibility that basal sliding and spatial gradients in ice dynamics are responsible for this anomalous region of the ice sheet.

DATASETS

We investigate regional changes in driving stress and causal forcings using recently updated surface and bedrock topography digital elevation models (DEMs) from Bamber et al (2013). The new DEMs are informed by airborne radar flightlines which, while of variable density over the ice sheet, generally show dense coverage over the W-SW study area (Bamber and others, 2013). In particular, a focused campaign as part of project ICEBRIDGE has elucidated surface and bedrock topography along the northern sector of the study domain, extending inland of Isunnguata Sermia, at a nearly unprecedented resolution. The DEM postings are at 1 km. Surface slope calculations from the surface DEM are averaged over 20 ice thicknesses.

We use raw ICEBRIDGE flightlines to confirm the feature does not result from DEM processing techniques and address the direct relationship between the surface feature and bedrock topography (Allen, 2010). Spacing between measurements along individual flight transects is nominally 15 – 30 m.

The surface velocity datasets utilized in the study come from INSAR-derived measurements by Joughin et al (2010). We use the 2008-2009 winter velocity posting. The dataset is provided at 500 m resolution. In flowline exercises, velocity observations that appear compromised in the interior are replaced with plane strain calculations, assuming the surface velocity is composed entirely of deformation. The transition from INSAR-derived to plane strain calculated velocity is chosen heuristically.

FEATURE CHARACTERISTICS

As a whole the ice sheet generally displays a regional driving stress profile which increases from the divide towards the margin (Figure 1). In contrast, W-SW GrIS displays a driving stress profile which slowly increases from the divide to the beginning of the DSA 60 – 100 km from the margin, where it is punctuated by a sharp decrease up to nearly 50% (Figure 2). The DSA occurs in two distinct reaches extending approximately 250 km north from a latitude of ~65°N (Figure 1, 2). Its north-south (N-S) trend is perpendicular to the regional flow direction. The spatial extent of decline is 30 – 60 km after which it increases again towards the margin.

Driving stress minima through the DSA are of similar magnitude as reaches >150 km inland. Yet, despite the consistent driving stress decline through this reach of the ice sheet, INSAR velocity observations show mixed behavior. The lowest velocities through the DSA tend to follow bedrock highs and not necessarily the lowest driving stress. Large reaches of the DSA show continually increasing velocities despite the low driving stress. Flowlines through multiple outlets show continually increasing velocity from the ice sheet interior towards the margin, and in some instances the drop in driving stress corresponds with a sharp velocity increase.

The DSA was previously attributed to a high bedrock plateau (Layberry and Bamber, 2001), however recent updates to the bedrock DEM do not support this hypothesis. The onset of the DSA occurs across a spectrum of basal topography. Different reaches of the southern half of the DSA correspond to rough topography, a topographic bench, and an apparent low, flat basal plain (Figure 2). To the north, the DSA initiates along variable basal topography which is lower than the southern counterpart. The absence of a consistent, high bedrock plateau is clear. While processing techniques between flightlines defining the bed DEM may render a picture of the topography which is incomplete at the level necessary to definitively rule out basal relief, individual flight lines themselves indicate the surface feature with no corresponding expression at the bed (Figure 3).

In contrast to the bedrock topography, the DSA shows a consistent relationship with a reach of reduced surface slope. DSA inception is marked by a change in ice sheet curvature where surface slopes decrease by up to 50% over a 20 – 25 km reach (Figure 2). This change marks a deviation from a theoretical parabolic profile which adequately fits the observed ice surface over many reaches of western Greenland (Supplemental Material). The close association of the DSA with changes in the ice sheet surface slope motivates investigation of processes influencing the ice sheet surface slope in the absence of a dominant basal topographic control.

PROCESSES INFLUENCING THE SURFACE PROFILE

Here we address two hypotheses that may influence the surface profile. We first assess the hypothesis that the surface slope anomaly on the ice sheet is a transient manifestation of surface mass balance perturbations. We also investigate the extent to which ice dynamics may be responsible for the surface perturbation.

Surface Mass Balance Perturbations

We investigate the likelihood that surface profile anomalies can result from mass balance perturbations using kinematic wave theory. Originally developed and applied to flood propagation and traffic flow (Lighthill and Whitham, 1955), kinematic waves were modified for the glacier setting by Weertman (1958) and Nye (1960, 1963a; b) to assess glacier change and response time from climate perturbations. Fields of interest, mainly surface height and flux changes, are addressed in terms of perturbations from an initial reference state. Two assumptions drive the kinematic wave formulation for ice flow: 1) flux is a function of thickness and surface slope ($q = f(h,\alpha)$), and 2) perturbations to the ice sheet are small with respect to the reference state. These assumptions allow linearization of the perturbed ice flux via Taylor series expansion. Consequent substitution in to conservation of mass yields the kinematic wave equation for ice:

$$\frac{\partial h_1}{\partial t} = a_1 - h_1 \frac{\partial C_0}{\partial x} - \left(C_0 - \frac{\partial D_0}{\partial x} \right) \frac{\partial h_1}{\partial x} + D_0 \frac{\partial^2 h_1}{\partial x^2}. \tag{1}$$

In Equation 1, h_1 is the ice thickness perturbation from a reference state, a_1 is the surface mass balance perturbation, and $C_0 = \left(\frac{\partial q}{\partial h} \right)_0$ and $D_0 = \left(\frac{\partial q}{\partial \alpha} \right)_0$ are advection and diffusion coefficients respectively, with α the surface slope. Variables with the subscript $_1$ are perturbed from their reference states. The subscript $_0$ refers to the reference state of the profile, and thus C_0 and D_0 encapsulate the physics driving ice flow in a reference state.

Commonly investigated along a single dimension (van de Wal and Oerlemans, 1995; van der Veen, 2001; Rémy and Legrésy, 2004), transient behavior in perturbed surface height depends on the advection and diffusion parameters (C_0 and D_0) which are static in time but can be spatially variable and must be prescribed along the modeled flowline. We calculate these constants following the empirical approach of Van der Veen (2001), who first implemented this method in assessing the response of Petermann Glacier to climate perturbations. Substitution of velocity given by the shallow ice approximation and differentiation (detailed in Appendix A) yields empirically based distributions of C_0 and D_0:

$$C_0 = (n+2)u_0 \tag{2}$$

and:

$$D_0 = \frac{nq_0}{\alpha_0} \tag{3}$$

determined from observation. In Equations (2) and (3), n is Glen's flow exponent, taken to be 3, and reference velocity, discharge and surface slope are given by u_0, q_0, and α_0 respectively.

In kinematic wave experiments we define the reference state along a flowline in W-SW GrIS which we take to be representative of the region (Figure 1, 4). INSAR surface velocity measurements define the reference velocity (u_0) along the profile, and thus the advection parameter (C_0) (Figure 4, 5). Prescription of the diffusion parameter is complicated somewhat by the fact that the reach already displays the surface slope anomaly and is thus in the perturbed state. We alleviate this complication by assuming that an idealized profile based on perfect plasticity is a reasonable representation of the reference state (Figure 6). We use surface slopes from this idealized profile to define D_0 along the flowline (Figure 5).

Comparison of an idealized profile with the observed also provides a zeroth order metric of the size of surface perturbation we seek to investigate. This comparison indicates that along the DSA, the surface profile deviation occurs over an approximately 60 km reach and displays a maximum vertical deviation on the order of many tens to 100 m (Figure 6). The objective of the kinematic wave experiments is to test the plausibility of inducing surface perturbations with a similar aspect ratio from surface mass balance anomalies. Perhaps most likely are scenarios whereby remote perturbations in surface conditions sweep across the region of interest as a transient wave.

We explore remote surface mass balance perturbations as increases near the ice sheet divide, decreases near the ice sheet margin, and a combination across the full length of the profile. Additionally, we test local perturbations in surface mass balance as an extreme scenario to assess the magnitudes of perturbation necessary to induce changes in the surface profile. Finally, as a means of assessing the stability of the observed surface anomaly, we investigate the time scales of decay for an initially perturbed surface in the absence of a mass balance anomaly. In contrast to the previous experiments which probe causality of surface adjustments from mass balance perturbations, in this experiment we neglect causation and instead use the a priori assumption of existence to explore transient behavior of such a feature.

With diffusion and advection coefficients prescribed across the profile line (Figure 5), we solve Equation (1) using fully implicit Backward Euler techniques to improve stability. The 1-D grid size is 100 m and the time step is 1 year. Unless stated otherwise, experiments are run for 5,000 years.

Ice dynamics

The primary objective in investigating ice dynamics is to assess the degree to which longitudinal variations in deformation and sliding are likely to exist. We concern ourselves primarily with ice sheet sliding and gradients therein because the surface profile has been theoretically shown to be sensitive to such variability (Gudmundsson, 2003).

In order to assess the partitioning of surface motion in to sliding and deformation, the ice deformation component needs to be constrained and the remaining difference is attributed to sliding. This is made difficult by the dependence of deformation on ice temperature and other rheological factors such as impurity content and crystal orientation that are spatially heterogeneous and poorly constrained throughout the GrIS. Ice temperature measurements in the study reach are limited to a single profile at the ice sheet divide Dye 3 (Gundestrup and Hansen, 1984), and profiles within the ablation zone (Harrington and others, *Temperature distribution and thermal anomalies along a flowline of the Greenland Ice Sheet,* in review). Rheological factors impacting ice deformation are even more poorly constrained, limited to mechanical tests on cores (Shoji and Langway Jr., 1985) and modeling from inclinometry surveys at Dye 3 (Dahl-Jensen and Gundestrup, 1987).

In light of the compounding uncertainties surrounding temperature and rheological enhancement factors, rather than use a flow model of increasing complexity (e.g. Meierbachtol and others, *Impact of field-constrained boundary conditions on western Greenland's thermo-mechanical state*, in review), we investigate deformational velocity alone under a spectrum of conditions using the shallow ice approximation. Our assumption of isothermal conditions is a simplification of the ice sheet state, and shallow ice deformational velocity calculations are limited in considering gravitational driving stress alone. Yet, this simplification is justified over much of the ice sheet interior where the driving stress is likely to be balanced by drag at the bed (van der Veen, 2013).

The intent of deformation calculations is not to exactly to reproduce present ice behavior; such a task would be unconstrained with any state-of-the-art model as a result of factors not limited to those discussed above. Instead, the objective is to investigate the suite of temperatures and rheological enhancement factors necessary to meet velocity observations in order to elucidate reaches where either large changes in ice properties are necessary or additional mechanisms of motion (e.g. sliding) are likely.

We assume a range of vertically isothermal temperatures and calculate the rheological enhancement necessary to achieve the measured surface velocity following rearrangement of the vertically integrated shallow ice approximation:

$$E = (n+1)\left(2\overline{A}(T)h\right)^{-1}\tau_d^{-n}u_{obs} \tag{4}$$

where E is a rheological enhancement factor, $\overline{A}(T)$ is a vertically averaged, temperature-dependent flow rate factor, h is the local ice thickness, and n is the flow exponent which we take to be three. We perform this calculation along the same reference flowline used in the kinematic wave experiments. Calculation of the range of enhancement factors necessary to match the velocity observations under the limiting assumptions permits logical assessment of the divergence between surface velocities and potential deformational velocity under static enhancement factors. It also allows a first-order assessment of the rheological softening necessary to match observations across the DSA in order to inform sliding inferences.

RESULTS

Surface Mass Balance Perturbations

Kinematic wave experimental results are subject to uncertainty stemming from the parameterization and smoothing of advection and diffusion coefficients along the profile as well as from the use of an idealized profile in the diffusion parameterization. Sensitivity testing with less smoothing of constants C_0 and D_0 indicates that the effects from noisier prescriptions have little impact on the perturbed height results. The magnitude of D_0, up to $4\text{x}10^7$ m^2 a^{-1} over the length of the profile, is corroborated by previous work in Greenland (van der Veen, 2001), and Antarctica (Rémy and Legrésy, 2004). Considering that local asperities in slope are more likely to diffuse under thick ice with a corresponding higher driving stress than a thinner ice equivalent, we believe the spatially variable coefficients to be physically justified. Even so, experimentation with a spatially constant diffusion parameter of the same of order magnitude (~$3\text{x}10^7$ m^2 a^{-1}) as previous research only confirms interpretation from the results below.

Remote mass balance forcing

Results from a mass balance perturbation applied near the margin are illustrated in Figure 7 (A, D). In response to a 0.2 m a^{-1} decrease in mass balance (i.e. a 0.2 m a^{-1} increase in ablation near the terminus), the perturbed surface approaches a steady state after 5,000 years. A maximum surface height drop of ~11 m occurs near the terminus and gradually propagates inland towards the divide.

A surface mass balance increase near the divide is manifested in an increase in profile elevation along the entire transect (Figure 7 B, E). After 5,000 years surface height has increased from 18 m at the terminus to over 45 m close to the divide. Despite the reasonably sharp change in surface mass balance, which is imposed as a logistic curve over 35 km, the aspect ratio of the perturbed height is tens of meters over many hundreds of kilometers.

In response to a mass balance perturbation which varies from -0.2 to 0.2 m a^{-1} over a distance of 25 km (Figure 7, panel C), the initial height response is an increase inland of the mass balance perturbation intercept, and a decrease below it (Figure 7, panel F). However, advection draws the mass balance increase towards the margin, and after some hundreds of years the surface elevation recovers in reaches experiencing a mass balance decrease. A new steady state is established after 5,000 to 10,000 years, and while the vertical magnitude of surface perturbation approaches the metric (~70 m), this change occurs over the entire profile.

Local mass balance forcing

Profile adjustment in response to a localized surface mass balance forcing with an amplitude approaching -5 m is presented in Figure 8. A surface mass balance perturbation of this shape and amplitude lacks observational justification, but represents an extreme scenario to test the ability of a surface perturbation to be induced from even unrealistic changes in accumulation or ablation. Twenty years from the inception of mass balance perturbation, the surface elevation decreases by up to 10 m, and the lateral extent of perturbation is over 100 km. The asymmetry of the surface height perturbation grows with time, as does the aspect ratio. To induce a vertical perturbation on the order of 60-70 m requires a horizontal scale of many hundreds of kilometers.

Initial thickness perturbation

Results from the decay of a Gaussian surface disturbance with a maximum thickness perturbation of ~65 m show rapid dissipation of the feature. The disturbance recovers by over 50% in the first 5 years of simulation, with mass conservation satisfied by lowering of the shoulders away from the initial disturbance (Figure 9). After twenty years the disturbance has recovered from its initial peak to a minimum elevation of -23 m below reference, and measurable drawdown >1 m has extended 85 km inland from the location of peak disturbance. Over this time interval the local elevation trough is advected 12 km towards the terminus.

Ice Dynamics

Plane strain calculations show that 200 km inland of the margin, surface velocity measurements are achieved with isothermal ice temperatures ranging from -8 to -5 °C under observation-guided enhancement factors between 2 – 3 (Dahl-Jensen and Gundestrup, 1987) (Figure 10). In the absence of deformation enhancement, deformation does not satisfy surface measurements even under temperate conditions. If the observation-based enhancement factors are assumed spatially constant, the increase in surface velocity is accommodated by a gradual increase in temperature until approximately 20 km from the beginning of the DSA. The inception of decreasing driving stress forces a sharp rise to temperate conditions.

The beginning of the DSA along the reference flowline is accompanied by a continued increase in measured surface speed which is at odds with the drop in driving stress. In order to achieve observed surface speeds, the ice column must soften by an order of magnitude or more over <20 km (Figure 10). If a constant enhancement value ($E = 3$) is assumed, the disparity between calculated deformational velocity and the velocity at the surface reaches 50 m a^{-1} through the DSA even when conditions are fully temperate (Figure 10).

The 30 km below the DSA to the ice margin is characterized by oscillating rheological enhancement as a result of rough bedrock topography, and hence large changes in ice thickness. The large disparity between driving stress and surface velocity in the 8 – 10 km nearest the margin results from thin ice <100 m thick at the extreme terminus.

DISCUSSION

Surface Mass Balance Perturbations

Our kinematic wave experiments with flow parameters tailored to the study area demonstrate the role of diffusion in dictating the spatial response of topography to surface mass balance perturbations. Mass redistribution resulting from surface processes occurs predominantly through decay as opposed to an advective kinematic wave, which is corroborated by previous synthetic analysis of transient surface response using perturbation methods (Gudmundsson, 2003). Under such strong diffusion, the horizontal scale required (hundreds of kilometers) to achieve a vertical surface disturbance up to 100 m in the vertical is an order of magnitude larger than that observed (tens of kilometers) across the DSA.

As displayed in the initial perturbation experiment, slope-driven diffusion enhances the initial response to a perturbed surface so that rates of elevation change are driven almost entirely by diffusion rather than advection. High rates of change (on the order of meters per year) and short recovery time scales of decades indicate that such perturbations would be quickly eliminated. The absence of large surface elevation change measured by satellite-derived laser altimetry in land-terminating western Greenland (above 65° N) suggests the region is not in the early stages of rapid recovery from a transient perturbation (Pritchard and others, 2009). Thus, spatial and temporal considerations strongly suggest that diffusion precludes the DSA from being a transient anomaly resulting from mass balance disturbances. Rather, it is most probable that the feature is a manifestation of processes within the ice or at the bed.

Ice Sheet Dynamics

The growing mismatch between high velocities and low driving stress at the DSA is clear, but the mechanism(s) responsible for this discrepancy are not readily apparent. Anomalously low ice thickness from errors associated with surface and bed DEMs could bias calculated driving stress and deformational velocity. However, achieving the observed velocity through deformation under such low surface slopes would require ice thickness up to 40% (many hundreds of meters) greater than the DEM. Errors of this magnitude are larger than those reported over the DSA and unsubstantiated in this region of relatively high flightline density (Bamber and others, 2013).

Our results show matching velocity observations by deformation with such low driving stress would require order-of-magnitude ice softening, but this lacks physical justification. Large scale change in rheology requires rapid realignment of crystal orientation or fabric development which has little observational basis. Achieving ice softening at the necessary magnitudes from increased water content is unsupported by laboratory experiments (Duval, 1977). A more tenable mechanism for recovering the measured velocity along the DSA is therefore an increase in basal sliding.

The location of the anomalous reach in the context of the glaciological facies is suggestive of potential physical mechanisms permitting high velocity despite the low driving stress. The northern reaches of the DSA occur along an elevation band which aligns closely with the measured long-term mean ELA (van de Wal and others, 2012) (Figure 2). While mass balance measurements are unavailable to the south, output from the regional climate model MAR (Tedesco and others) shows the 55 year mean ELA is also colocated with the DSA (Figure 2). The association of the DSA with the ELA in the study area infers dynamical change from the introduction of seasonally-generated surface meltwater to the bed. Remotely sensed, late-summer ice surface accelerations provide anecdotal evidence for sliding enhancement related to meltwater forcing in the high elevation reaches of the ablation zone (Palmer and others, 2011).

Assuming plane strain, an increase in vertically averaged velocity must be met by surface drawdown in order to satisfy mass conservation. Based on the above, we surmise that an increase in depth averaged velocity from enhancement in basal motion near the ELA has a corresponding impact on the surface profile and thus is a key process in the formation of the DSA. Such longitudinal sliding variations were implicated to explain surface variations and deformation of internal radar reflectors at Byrd Station, Antarctica (Whillans and Johnsen, 1983).

Previous works have suggested that the majority of the GrIS requires a strong sliding component to meet observed velocities (Rignot and Mouginot, 2012; Sergienko and others, 2014). Our analysis, however, indicates that under reasonable assumptions of temperature and rheology derived by observation (Gundestrup and Hansen, 1984; Shoji and Langway Jr., 1985; Dahl-Jensen and Gundestrup, 1987), it is plausible that deformation is the dominant component of motion above the DSA. This does not imply that basal slip is absent above the feature, but rather suggests that a transition from deformation-dominated motion to a regime with a greater fraction of sliding occurs across the DSA. Our hypothesis requires only that spatial gradients in sliding influence the surface profile, but does not necessarily assume purely no-slip behavior above the ELA.

Basal sliding likely increases at the inception of the DSA, and we hypothesize that these longitudinal gradients in basal motion may impact driving stress alone. However, it is probable that the complexity of ice flow dynamics precludes exclusive control of the DSA from a single physical process. Basal melt rates and the fraction of the bed at temperate conditions may affect the integrated basal water supply and hence the propensity for sliding. The location of the ELA up to 100 km inland of the ice margin could also render a greater reach of W-SW GrIS sensitive to meltwater-related dynamics than other regions of the ice sheet with a lower ELA close to the ice sheet edge. The complicating role of additional factors underscores the spatial heterogeneity of the GrIS and warrants further research not only to definitively constrain the regional perturbation in driving stress, but also to better understand why this type of anomaly is limited to W-SW GrIS.

CONCLUSIONS

We find that the region of anomalously low driving stress in W-SW GrIS, previously interpreted to be controlled by a bedrock plateau, is more strongly associated with inflections in the ice sheet surface profile leading to low surface slope. While the absolute magnitude of slope change is small (tenths of a degree), the fractional change is substantial and induces correspondingly large driving stress perturbations. The close association of driving stress with surface slope, and the lack of a consistent bedrock expression inducing such a change, motivate the investigation of other processes responsible for the anomalous region.

Kinematic wave experiments along a profile through the DSA illuminate the diffusive nature of the ice sheet response to surface mass balance perturbations. Mass balance changes propagate through diffusive decay as opposed to advective transport, limiting surface curvature stability. Diffusion rapidly eliminates initial surface perturbations over a period of decades. We thus conclude that the observed surface expression is not a transient response to regional surface mass balance anomalies.

Reduction in driving stress correlative with increasing surface velocity across much of the DSA necessarily dictates that a large change in ice flow dynamics take place. We surmise this change in dynamics is a key process manipulating the surface profile, and hence the DSA. The proximity of reduced driving stress with respect to the ELA suggests that the inception of meltwater penetration to the bed could be a plausible mechanism initiating such a dynamical shift. If correct, the potential modulating effect of meltwater-related sliding on driving stress presents a negative feedback that should be considered by future research on this heavily studied region of the ice sheet.

REFERENCES

Allen C (2010) Updated 2014. IceBridge MCoRDS L2 Ice Thickness. Boulder, Colorado USA: NASA DAAC at the National Snow and Ice Data Center.

Bamber JL, Griggs JA, Hurkmans RTWL, Dowdeswell JA, Gogineni SP, Howat I, Mouginot J, Paden J, Palmer S, Rignot E and Steinhage D (2013) A new bed elevation dataset for Greenland. *Cryosph.* **7**(2), 499–510 (doi:10.5194/tc-7-499-2013)

Bamber JL and Layberry RL (2001) A new ice thickness and bed data set for the Greenland ice sheet 1 . Measurement , data reduction , and errors. *J. Geophys. Res.* **106**(D24), 33773–33780

Bartholomew I, Nienow P, Sole A, Mair D, Cowton T and King M a. (2012) Short-term variability in Greenland Ice Sheet motion forced by time-varying meltwater drainage: Implications for the relationship between subglacial drainage system behavior and ice velocity. *J. Geophys. Res.* **117**(F3), 1–17 (doi:10.1029/2011JF002220)

Cuffey KM and Patterson WSB (2010) *The Physics of Glaciers.*, 4th edn. Elsevier, Oxford

Dahl-Jensen D and Gundestrup NS (1987) Constitutive properties of ice at Dye 3 , Greenland. *Phys. Basis Ice Sheet Model.* (170), 31–43

Doyle SH, Hubbard A, Fitzpatrick AW, van As D, Mikkelsen AB, Pettersson R and Hubbard B (2014) Persistent flow acceleration within the interior of the Greenland ice sheet. *Geophys. Res. Lett.* **41**(3), 1–7 (doi:10.1002/2013GL058933.Received)

Duval P (1977) The role of the water content on the creep rate of polycrystalline ice. *IAHS Publ.* **118**, 29–33

Gudmundsson GH (2003) Transmission of basal variability to a glacier surface. *J. Geophys. Res.* **108**(B5), 2253 (doi:10.1029/2002JB002107)

Gundestrup NS and Hansen BL (1984) Bore-hole survey at Dye 3, south Greenland. *J. Glaciol.* **30**(106), 282–288

Joughin I, Smith BE, Howat IM, Scambos T and Moon T (2010) Greenland flow variability from ice-sheet-wide velocity mapping. *J. Glaciol.* **56**(197), 415–430 (doi:10.3189/002214310792447734)

Layberry RL and Bamber JL (2001) A new ice thickness and bed data set for the Greenland ice sheet 2. Relationship between dynamics and basal topography. *J. Geophys. Res.* **106**, 33781–33788

Lighthill MJ and Whitham GB (1955) On kinematic waves I . Flood movement in long rivers. *Proc. R. Soc. Lond. A. Math. Phys. Sci.* **229**(1178), 281–316

Nye JF (1960) The response of glaciers and ice-sheets to seasonal and climatic changes. *Proc. R. Soc. Lond. A. Math. Phys. Sci.* **256**(1287), 559–584

Nye JF (1963a) The response of a glacier to changes in the rate of nourishment and wastage. *Proc. R. Soc. Lond. A. Math. Phys. Sci.* **275**(1360), 87–112

Nye JF (1963b) On the theory of the advance and retreat of glaciers. *Geophys. J. R. Astron. Soc.* **7**, 431–456

Palmer S, Shepherd A, Nienow P and Joughin I (2011) Seasonal speedup of the Greenland Ice Sheet linked to routing of surface water. *Earth Planet. Sci. Lett.* **302**(3-4), 423–428 (doi:10.1016/j.epsl.2010.12.037)

Pritchard HD, Arthern RJ, Vaughan DG and Edwards L a (2009) Extensive dynamic thinning on the margins of the Greenland and Antarctic ice sheets. *Nature* **461**(7266), 971–5 (doi:10.1038/nature08471)

Raymond MJ and Gudmundsson GH (2005) On the relationship between surface and basal properties on glaciers, ice sheets, and ice streams. *J. Geophys. Res.* **110**(B08411), 1–17 (doi:10.1029/2005JB003681)

Rémy F and Legrésy B (2004) Antarctic ice sheet shape response to changes in outlet flow boundary conditions. *Glob. Planet. Change* **42**(1-4), 133–142 (doi:10.1016/j.gloplacha.2003.11.005)

Rignot E and Mouginot J (2012) Ice flow in Greenland for the International Polar Year 2008-2009. *Geophys. Res. Lett.* **39**(11), 1–7 (doi:10.1029/2012GL051634)

Sergienko OV, Creyts TT and Hindmarsh RC a. (2014) Similarity of organized patterns in driving and basal stresses of Antarctic and Greenland ice sheets beneath extensive areas of basal sliding. *Geophys. Res. Lett.* **Accepted** (doi:10.1002/2014GL059976)

Shoji H and Langway Jr. CC (1985) Mechanical properties of fresh ice core from Dye 3, Greenland. *Geophys. Monogr.* **33**(39-48)

Tedesco M, Fettweis X, Alexander P and Green G MAR Greenland Outputs 1958-2013. , CCNY Digital Archive

Van der Veen CJ (2001) Greenland ice sheet response to external forcing. *J. Geophys. Res. Atmos.* **106**(D24), 34047–34058

Van der Veen CJ (2013) *Fundamentals of Glacier Dynamics.*, 2nd edn. CRC Press, Boca Raton, FL

Van de Wal RSW, Boot W, van den Broeke MR, Smeets CJPP, Reijmer CH, Donker JJ a and Oerlemans J (2008) Large and rapid melt-induced velocity changes in the ablation zone of the Greenland Ice Sheet. *Science* **321**(5885), 111–113 (doi:10.1126/science.1158540)

Van de Wal RSW, Boot W, Smeets CJPP, Snellen H, van den Broeke MR and Oerlemans J (2012) Twenty-one years of mass balance observations along the K-transect, West Greenland. *Earth Syst. Sci. Data* **4**(1), 31–35 (doi:10.5194/essd-4-31-2012)

Van de Wal RSW and Oerlemans J (1995) Response of valley glaciers to climate change and kinematic waves: a study with a numerical ice-flow model. *J. Glaciol.* **41**(137), 142–152

Weertman J (1958) Traveling Waves on Glaciers. *IASH* **47**, 162–168

Whillans IM and Johnsen SJ (1983) Longitudinal Variations in Glacial Flow : Theory and Test using Data from the Byrd Station Strain. *J. Glaciol.* **29**(101), 78–97

FIGURES

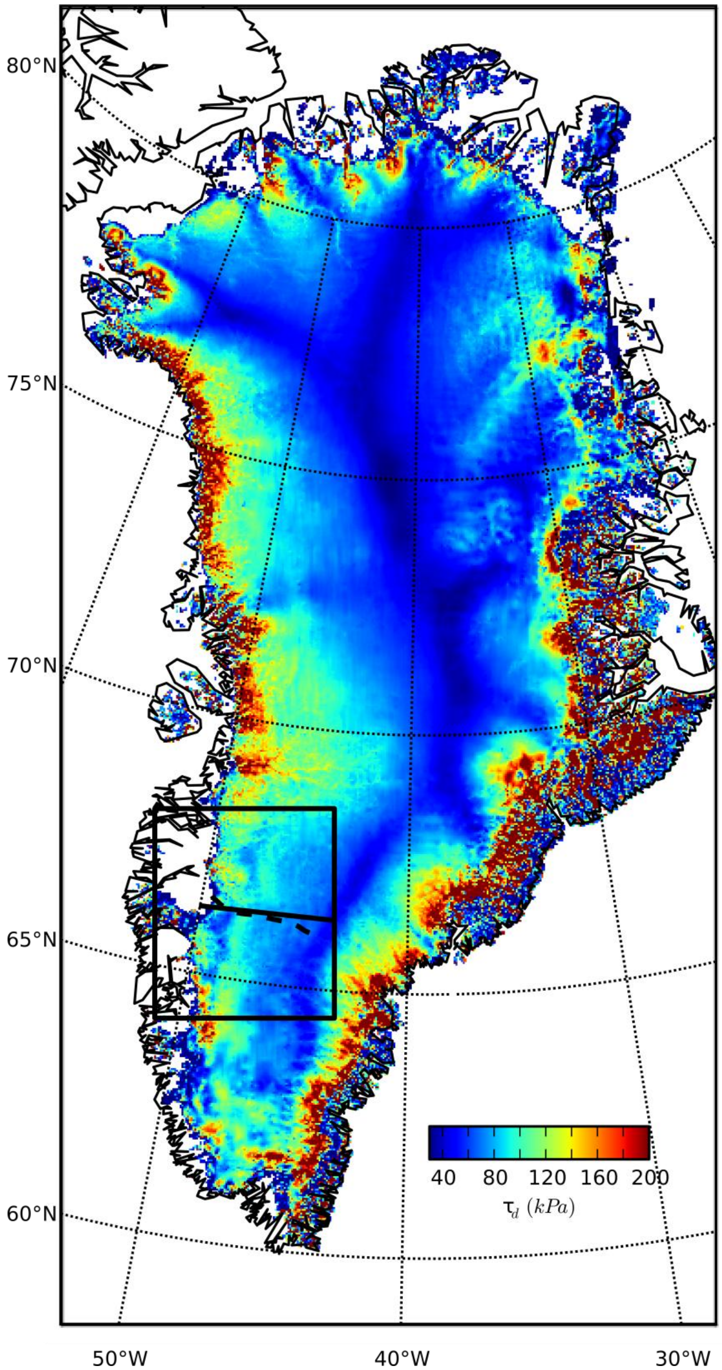

Figure 1: Driving stress for the Greenland ice sheet. ICEBRIDGE flight line in Figure 3 is illustrated as the solid black line. Dashed black line is a flowline extending inland from the ice sheet terminus. The DSA is bracketed by the black box, which denotes the extent of panels in Figure 2.

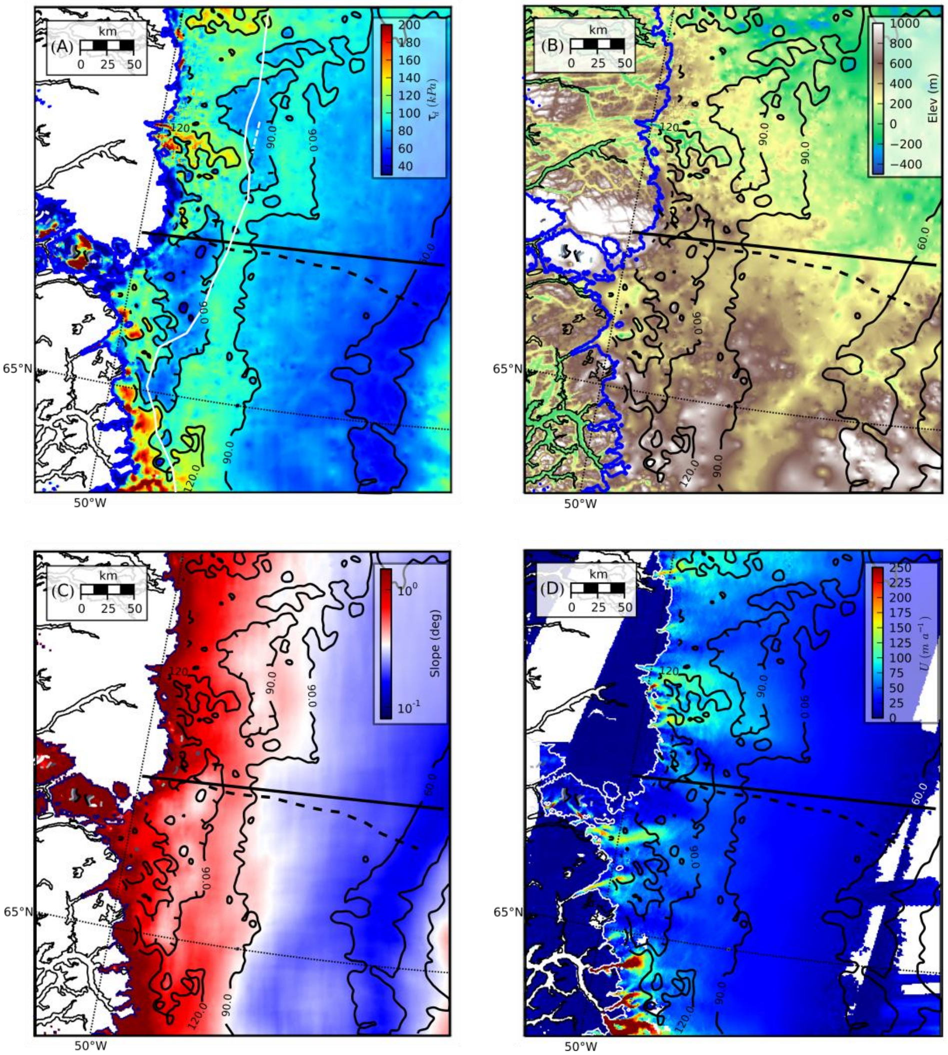

Figure 2: Driving stress (A), Bamber et al (2013) bedrock topography (B), surface slope averaged over 20 ice thicknesses (C), and 2008-2009 INSAR-derived winter surface velocity (Joughin et al, 2010) (D) over the W-SW GrIS sector. Driving stress contours at 60, 90 and 120 kPa are shown in each panel. Hatch marks on contour lines indicate the direction of decreasing driving stress through the DSA. Solid white line in (A) shows the 55 year mean ELA output from MAR. Dashed white line in (A) is the mean ELA from van de Wal et al (2012). Dashed and solid black lines indicate the same flowline and ICEBRIDGE flight profiles displayed in Figure 1.

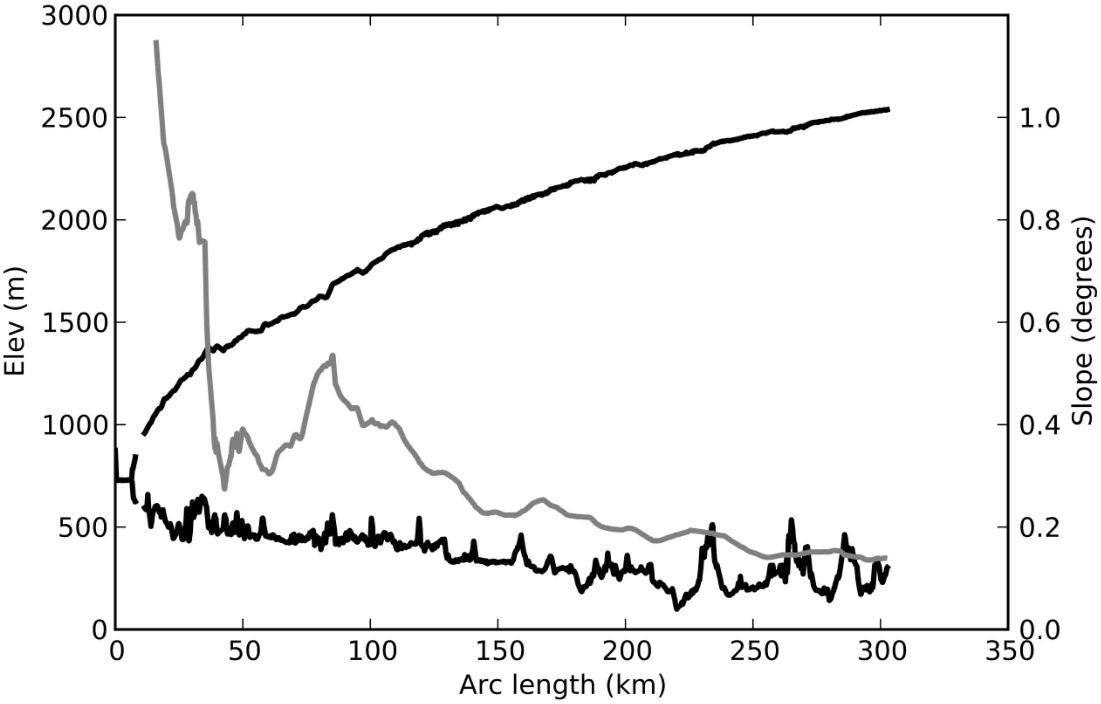

Figure 3: ICEBRIDGE flight line corresponding to the solid black line in Figure 1. Surface and bed topography are shown in solid black. Surface slope, averaged over 20 ice thicknesses, is displayed in gray.

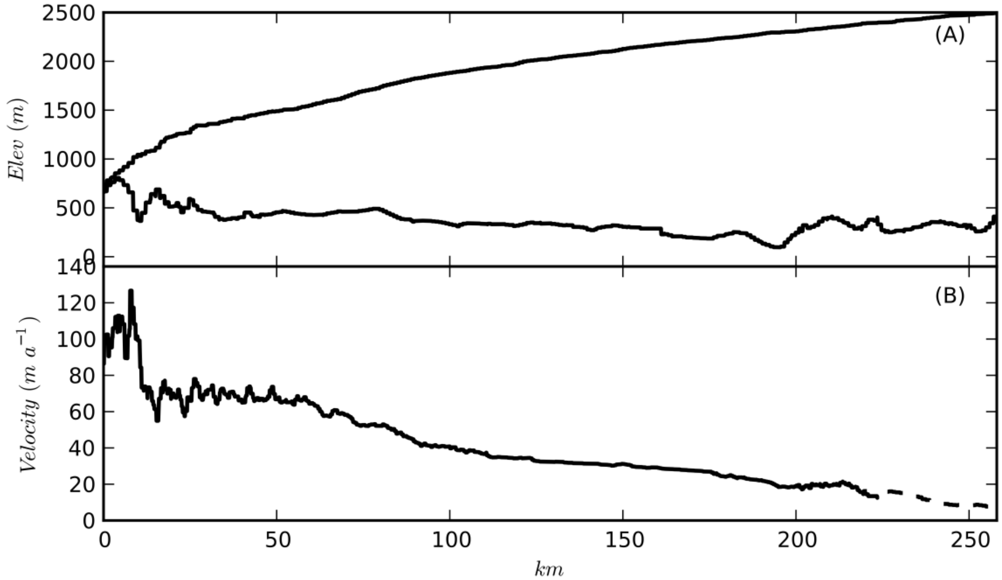

Figure 4: Surface and bedrock topography (A) and surface velocity (B) along the flowline denoted by the dashed black line in Figure 1. INSAR measurements define the velocity profile until the visual integrity is compromised. Thereafter, velocities are calculated assuming plane strain and displayed in (B) as the dashed line.

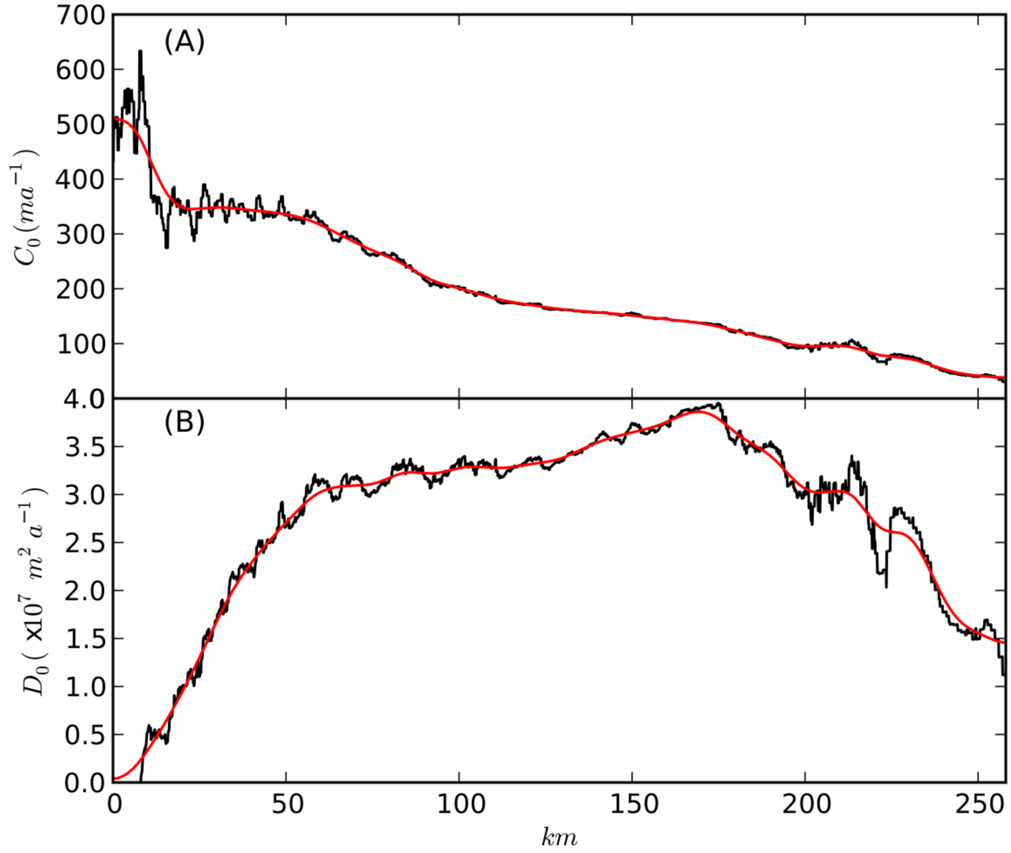

Figure 5: Advection (A) and diffusion (B) coefficients calculated based on the topography and velocity profiles in Figures 6, and 4 respectively. Solid black line shows the raw calculation, and red lines are smoothed values used in experiments.

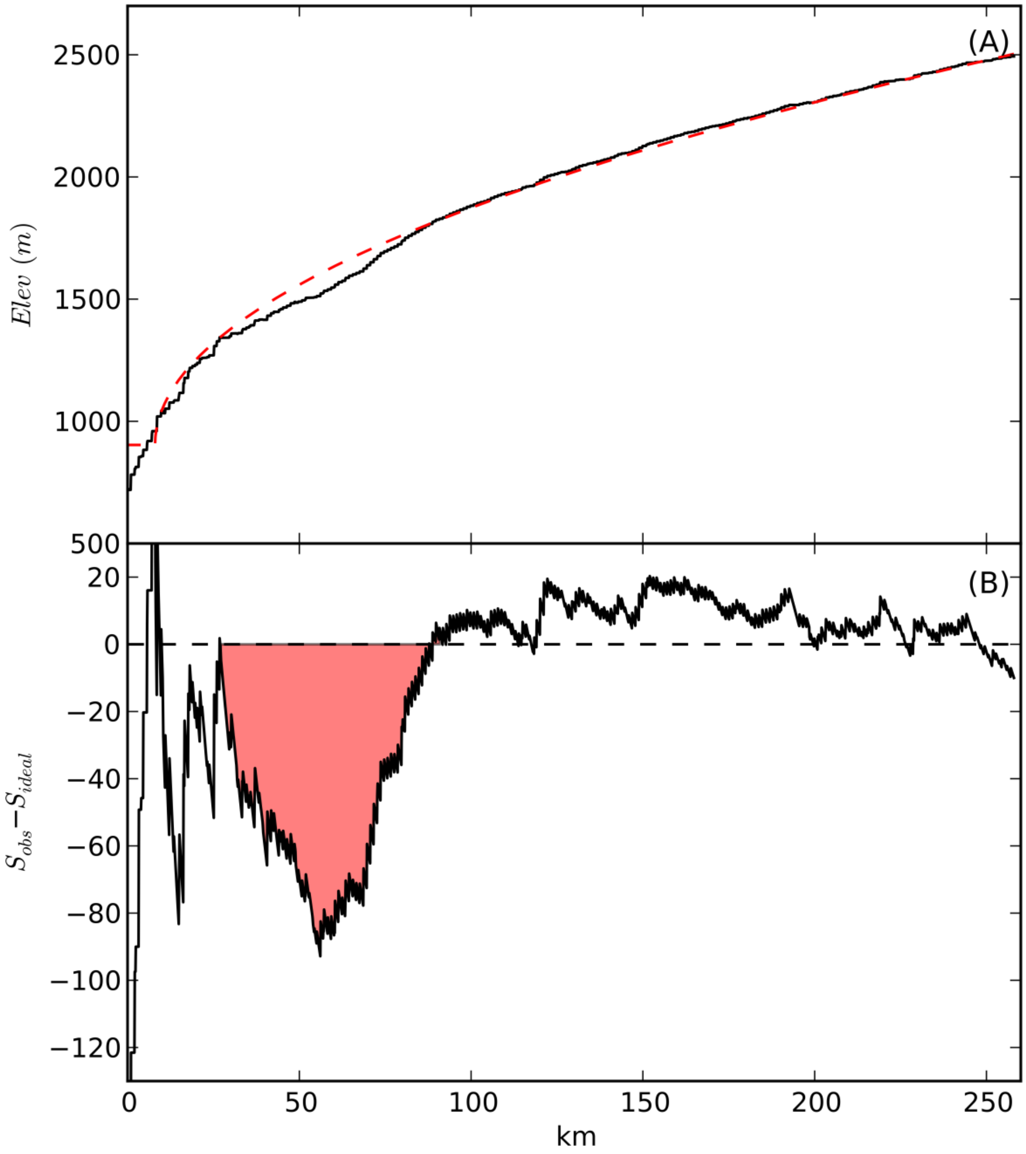

Figure 6: Comparison of observed and idealized profiles along the flowline shown in Figure 1. Observed surface elevation is shown in solid black in (A) and the idealized equivalent is displayed as dashed red line. The difference between the two profiles is displayed in (B), with the perturbation corresponding to the surface anomaly in question is shaded in red.

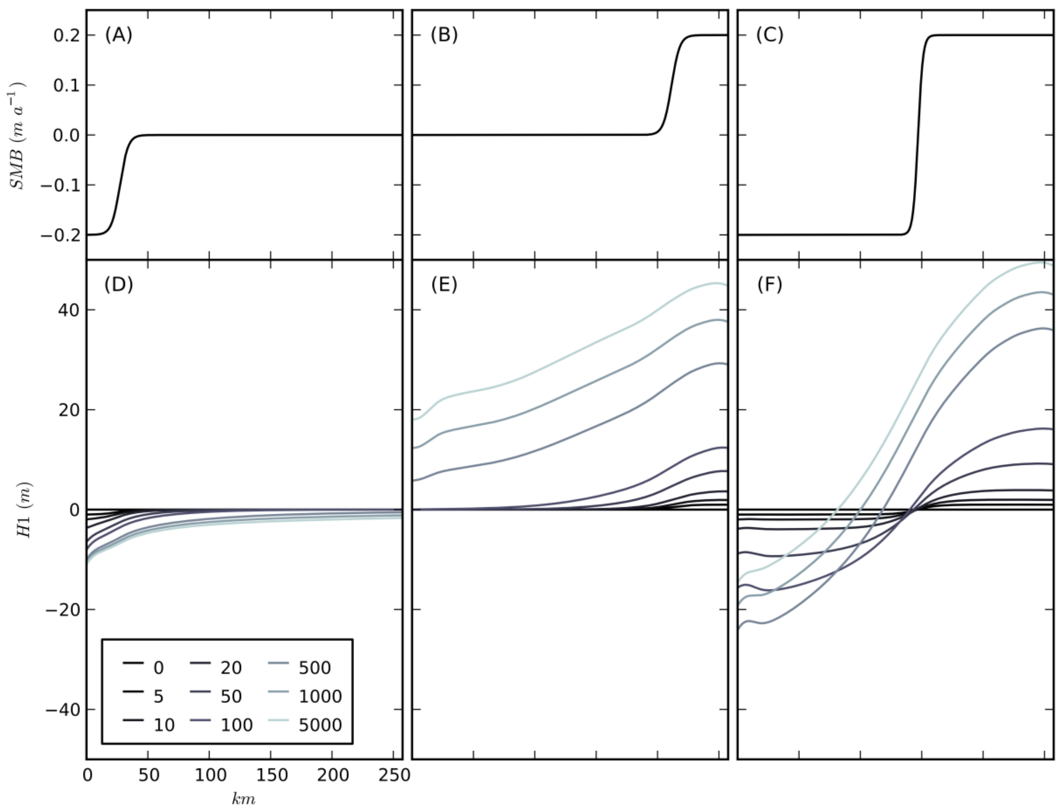

Figure 7: Results from three separate remote surface mass balance perturbation experiments. Surface mass balance perturbations are defined by logistic functions shown in the top row (panels A, B, and C) with equal y-axis scales in each panel. Surface height perturbation responses at snapshots in time are shown in the bottom row (panels D, E, and F). Color scale corresponds to years from the initiation of mass balance perturbation and is shown in the legend. Panels A and D correspond to a mass balance perturbation representing increased ablation near the ice sheet margin. Panels B and E correspond to an increase in accumulation near the ice sheet divide. Panels C and F display results from an increase in accumulation from the ice sheet divide to a distance of 100 km, after which the perturbation sharply decreases for the remainder of the profile.

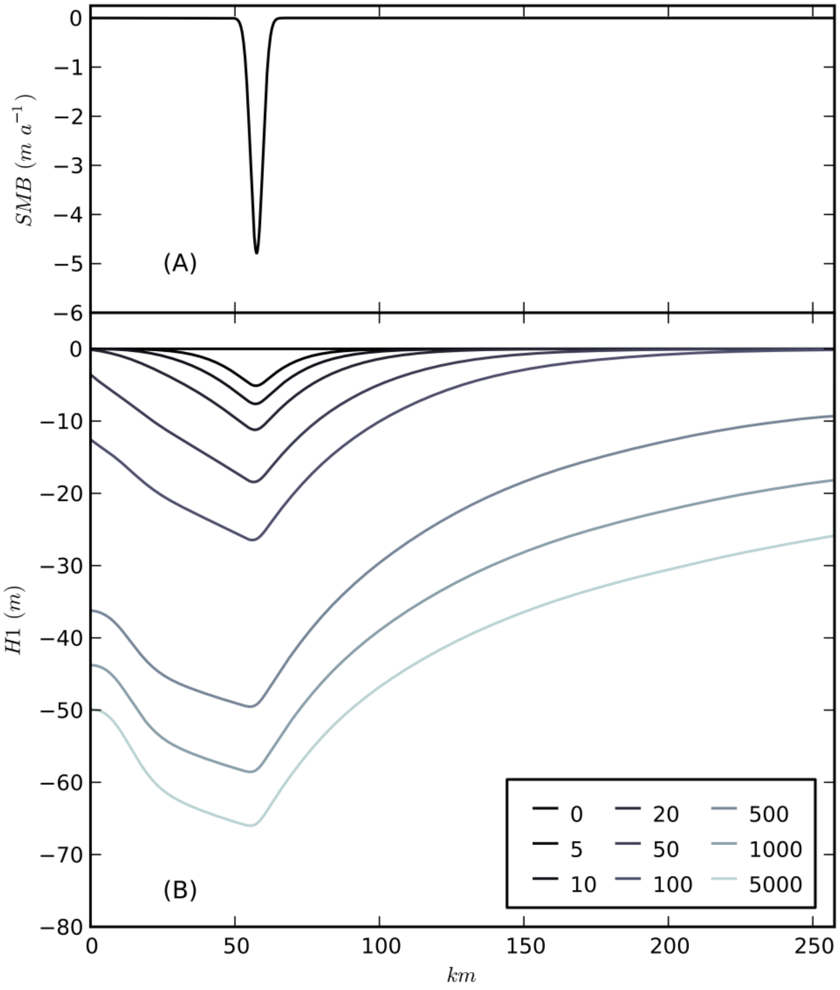

Figure 8: Results from the local surface mass balance perturbation experiment. Surface mass balance is a Gaussian pulse reaching a minimum value of -5 m a^{-1} (A). The surface height response is shown at different snapshots in time in (B). The color scale shows the time (in years) from start of the surface mass balance perturbation, and is shown in the legend.

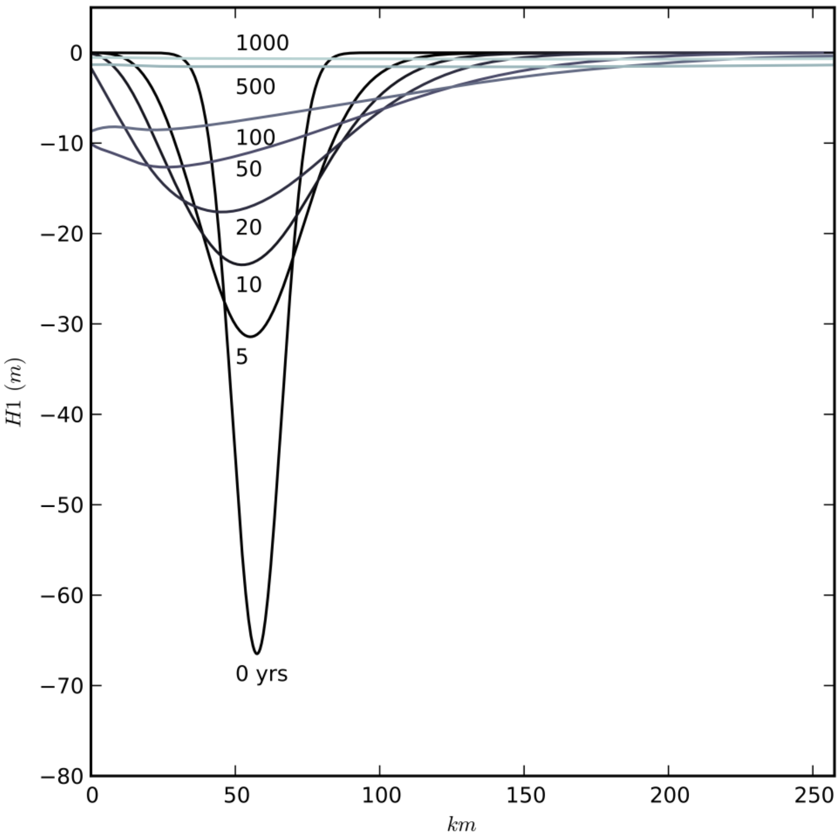

Figure 9: The recovery of an initially disturbed surface profile in the absence of a surface mass balance anomaly. Curves show the perturbed height at different snapshots in time from the initial state at 0 years to 1000 years.

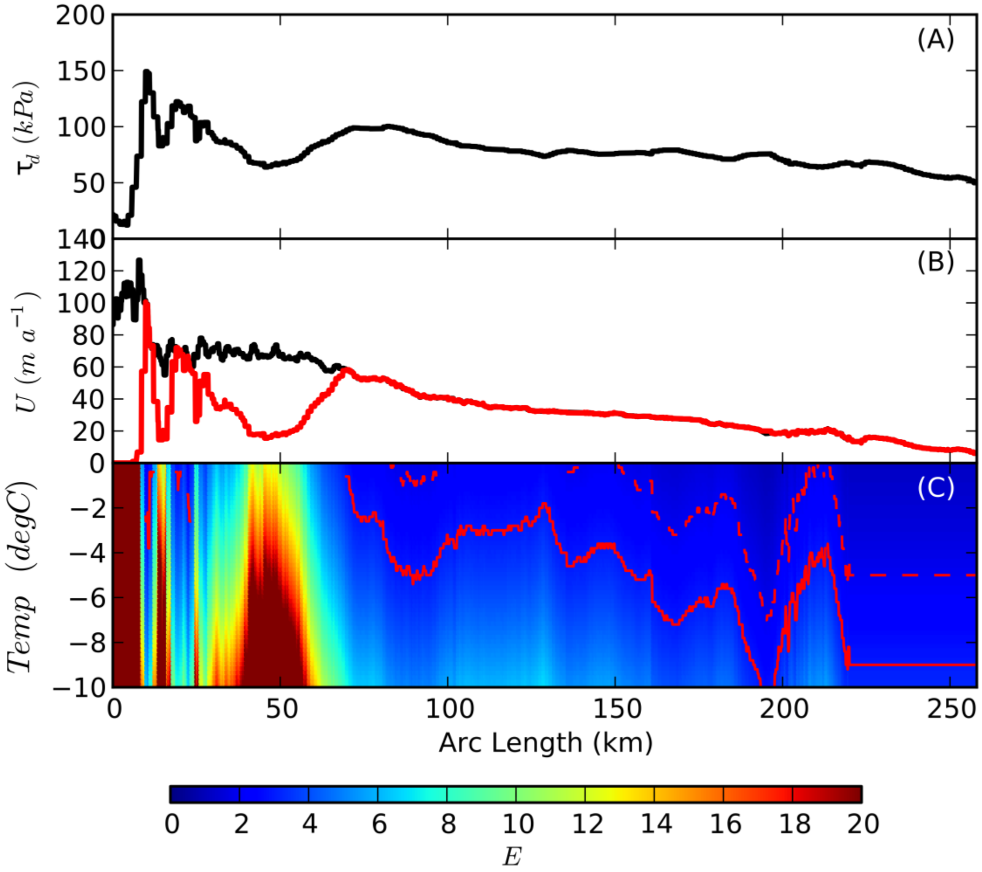

Figure 10: Dynamical calculations along the flowline in Figure 1. Driving stress is shown in (A). INSAR-derived velocity (black line) and plane strain velocity (red) are shown in (B). Plane strain velocity is calculated following a constant enhancement factor E=3 and the temperature profile shown as the solid red line in (C). Across the DSA, temperate conditions are imposed. Panel C displays the necessary rheological enhancement factor in order to match the given measured surface velocity in (B) under isothermal temperature (y-axis). Color bar indicates the enhancement factor magnitude. Solid and dashed red contours indicate the lines of constant enhancement factor at E=3 and E=2 respectively. Flat contours beyond 220 km result from the fact that surface velocity is calculated from plane strain in the absence of velocity observations.

SUPPLEMENTAL MATERIAL

Comparison of Parabolic Surface Profiles to Observed Greenland Surface Elevation

We address the anomalous surface profile through the DSA by comparison against a theoretical parabolic profile of the form:

$$h(x) = C(L - x)^{0.5}, \tag{S1}$$

where L is the length of the profile and $C = \sqrt{\frac{2\tau_{yield}}{\rho g}}$ with the yield stress given by τ_{yield}, gravitational acceleration g, and ice density ρ. Here we compare the parabolic profile to four additional, randomly selected flowlines along western GrIS. The locations of the flowlines on the ice sheet are displayed in Figure S1.

Figures S2 – S7 (corresponding to flowlines A – D in Figure S1) indicate differences between observed surface topography and theoretical. A flowline through the DSA is indicated in Figure S6. North of the DSA, differences between the observed surface and theoretical profile are generally less than 50 m. A consistent trend in the deviation between observed and theoretical surface profiles is evident in Figure S2, and may result from complications associated with the marine-terminating nature of the flowline. In contrast to the flowline through the DSA (Figure S6), observed surface deviations from theoretical that are greater than ~50 m generally coincide with sharp changes in bedrock topography of magnitude 500 m or more (eg. Figure S3 at 90 km or Figure S4 at 25 – 50 km). The large surface deviation coincident with the DSA is of broader extent, and the magnitude of deviation is equal to or greater than the maximum deviation in the other displayed profiles. This is particularly notable considering the lack of complex bedrock topography in the flowline through the DSA.

South of the DSA, the observed surface profile displays behavior which strongly deviates from theoretical. Large scale changes in surface topography are evident below ~1800 m elevation. Limited bedrock topography suggest that this behavior may be related to large scale bedrock relief on the order of 800 m through the profile.

Empirical Evaluation of Advection and Diffusion Parameters

In the empirical approach to calculating advection and diffusion parameter we implement the shallow ice approximation to solve for the reference velocity (u_0):

$$u_0 = \frac{2A}{n+1}\left(\rho g \sin \alpha_0\right)^n h_0^{\,n+1} \tag{S2}$$

where A is the isothermal flow rate factor, ρ is ice density, and g is the acceleration due to gravity. Substitution of Equation (A1) in to the relation for discharge $q_0 = u_0 h_0$, and differentiation with respect to h yields:

$$C_0 = (n+2)u_0 \tag{S3}$$

where u_0 is the reference velocity along the profile length. Equation (A2) indicates that kinematic waves travel down-glacier at a speed equal to 5 times the reference velocity for the commonly assumed case where $n = 3$. Similarly, substitution and differentiation with respect to α yields:

$$D_0 = \frac{nq_0}{\alpha_0}, \tag{S4}$$

an expression for the diffusion coefficient which can be determined from observation.

To develop advection and diffusion relations using the observation-based framework, we extract topography and surface velocity along a typical flowline through a reach of western Greenland which displays the anomalous surface feature (Figure 1, 4). We assume an idealized surface profile along the flowline following perfect plasticity (Cuffey and Patterson, 2010):

$$h_0(x) = C(L-x)^{0.5}, \tag{S5}$$

where L is the length of the profile and $C = \sqrt{\frac{2\tau_{yield}}{\rho g}}$ is a constant chosen as 3.2 to be a best fit match over the observed surface profile. This corresponds to a yield stress (τ_{yield}) of 46 kPa. This yield stress is low compared to calculated driving stress values, likely as a result of the flat bed assumption in the perfect plasticity model. Nevertheless, in the present case we are interested in the deviation of the observed profile from a plausible idealized surface. Experimentation with alternative artificial prescriptions of the surface incorporating bedrock topography continue to show a strong deviation at the DSA. No synthetic geometry will perfectly match the observed away from the DSA and we choose the perfect plasticity assumption with low yield stress as it provides a best-fit match over the bulk of the profile, and hence provides realistic surface slopes close to observation. Prescription of the synthetic surface with an alternative idealized model has a negligible impact on the results.

With velocity measurements, surface topography and slope from the idealized scenario, we calculate the advection and diffusion constants across the profile from equations (A2) and (A3). To alleviate the introduction of artificially high gradients resulting from the amplification of noise in the data we apply a Gaussian filter with a standard deviation (σ) of 5 km to the advection and diffusion profiles. This yields smoothed representations of the advection and diffusion parameters describing the reference state of flow across the profile. Conceptually, these profiles are logical with respect to the ice sheet. In the ice sheet interior, thick ice and low surface slopes mean diffusion strongly influences the surface profile. Towards the ice sheet margin, thinning ice, increasing slopes, and increasing velocity amplify the importance of advection at the expense of diffusion. However, because surface velocities along the profile fail to exceed ~120 m a^{-1}, the advection coefficient remains relatively small compared to previous work (van der Veen, 2001).

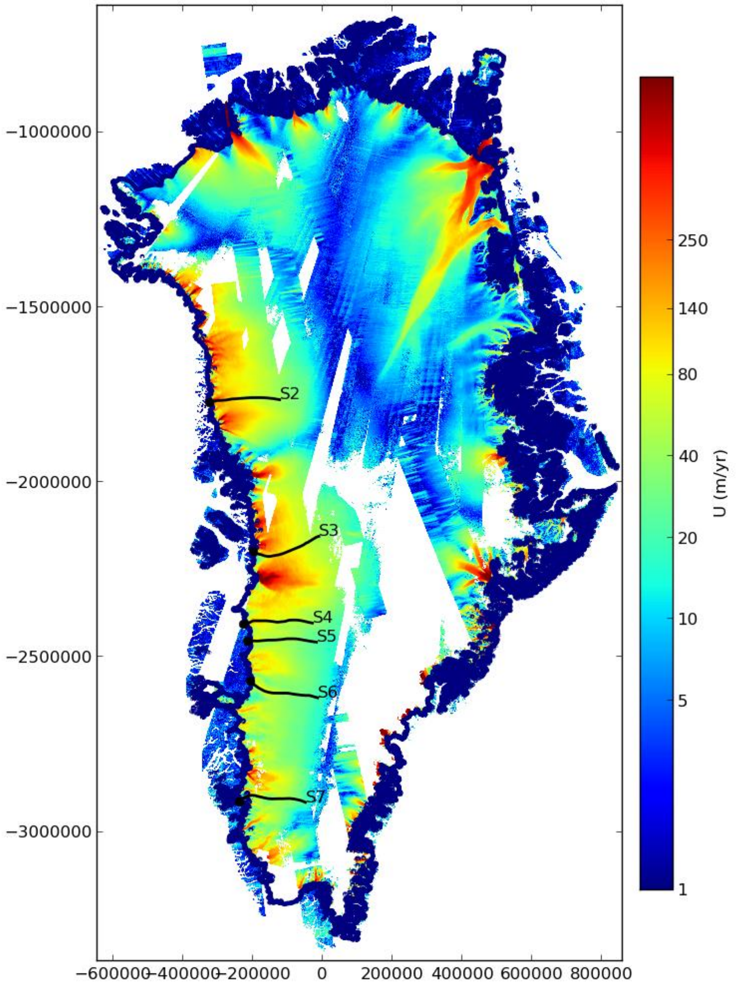

Figure S1: Locations of the flowlines shown in Figures S2 – S6 overlain on 2008-2009, INSAR-derived surface velocity.

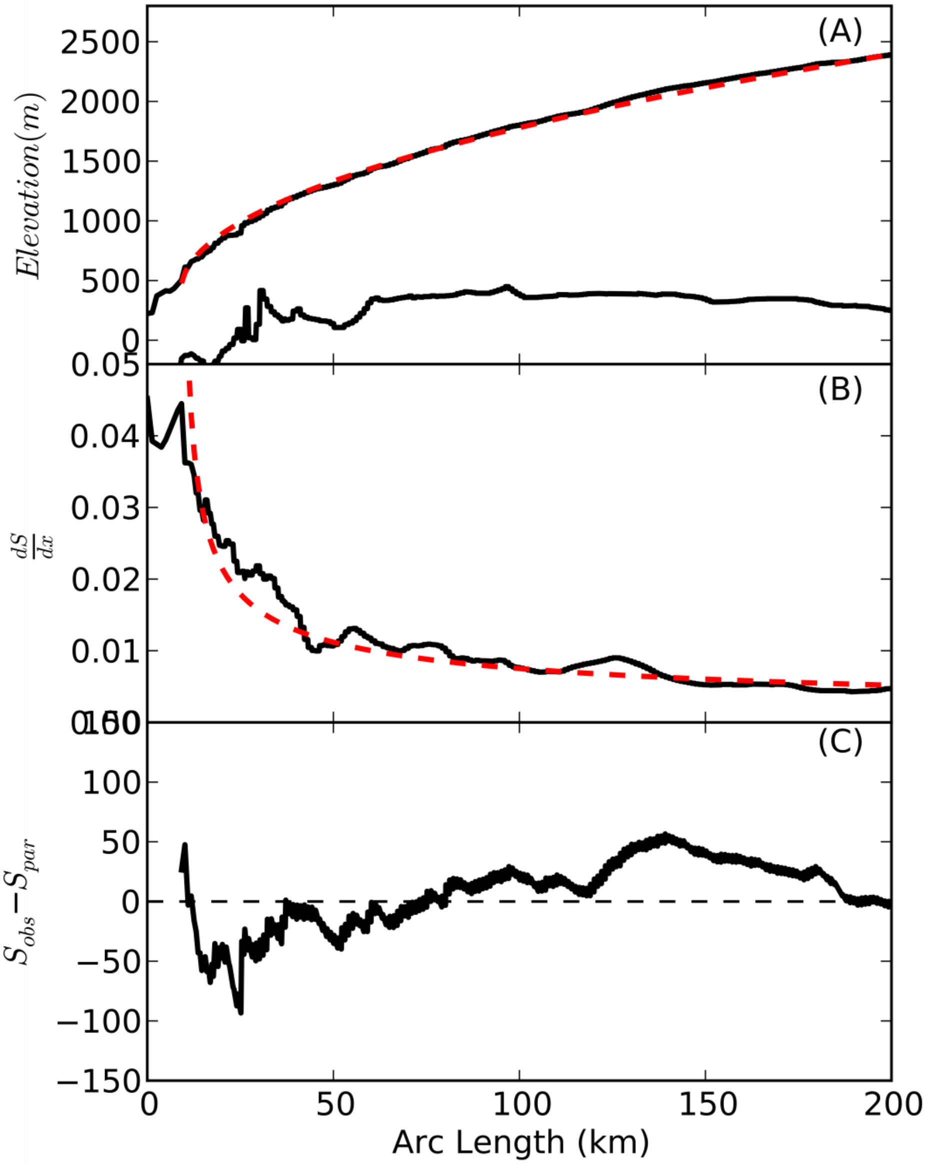

Figure S2: Surface and bed elevation (A), Surface slope (B), and the difference between observed and theoretical profiles (C) corresponding to flowline S2 in Figure S1. Red dashed lines in panels (A) and (B) correspond to theoretical parabolic topography. Solid black lines are observed surface and bed topography in panel (A), and surface slope in (B).

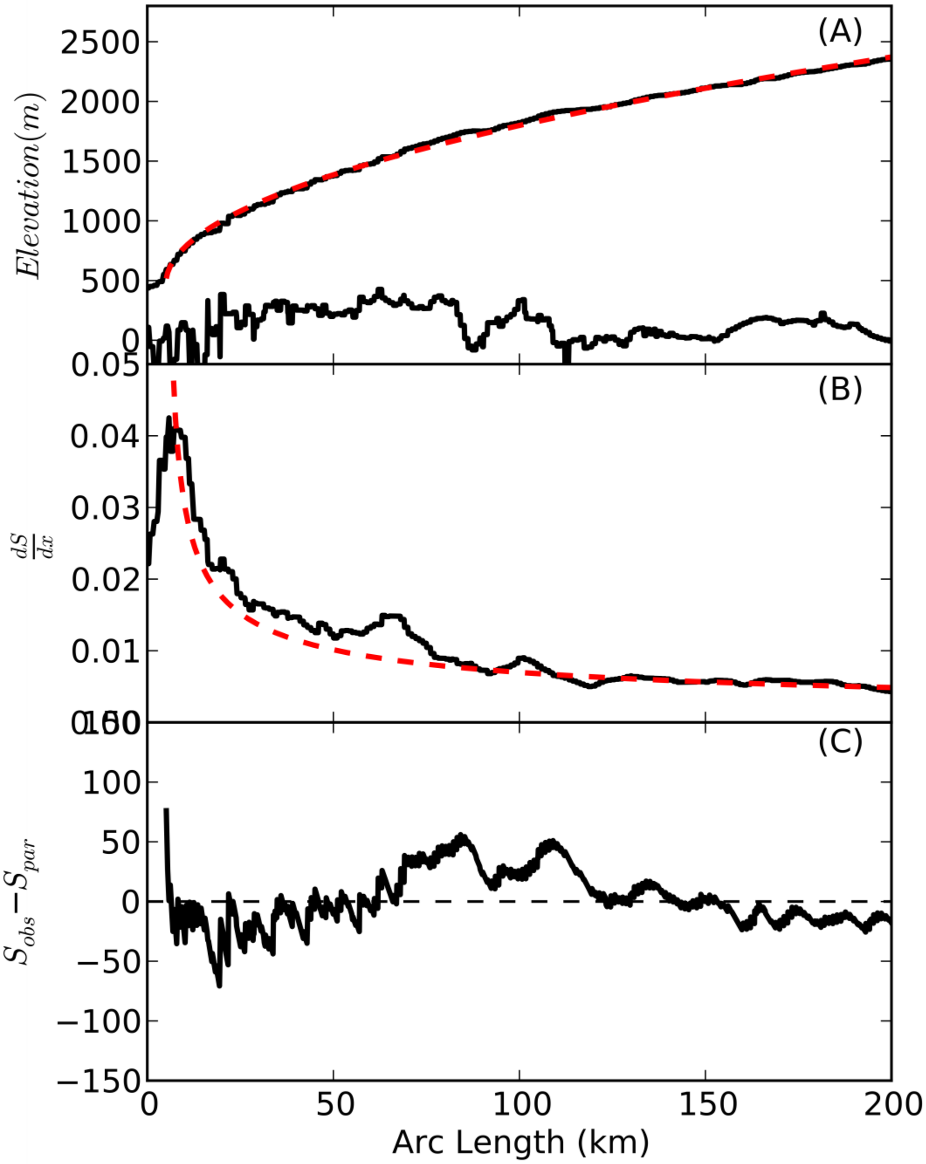

Figure S3: Same as Figure S2, but for profile S3.

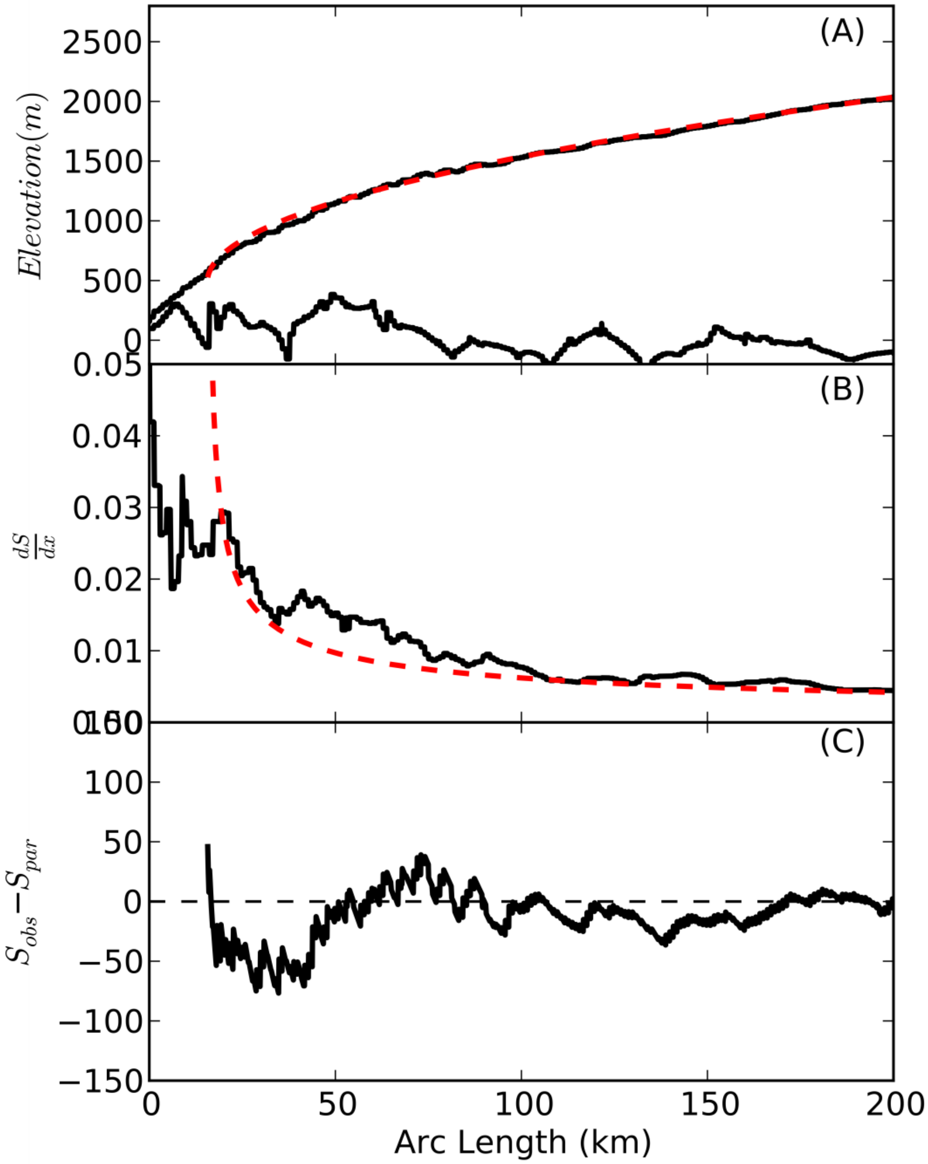

Figure S4: Same as Figure S2, but for profile S4.

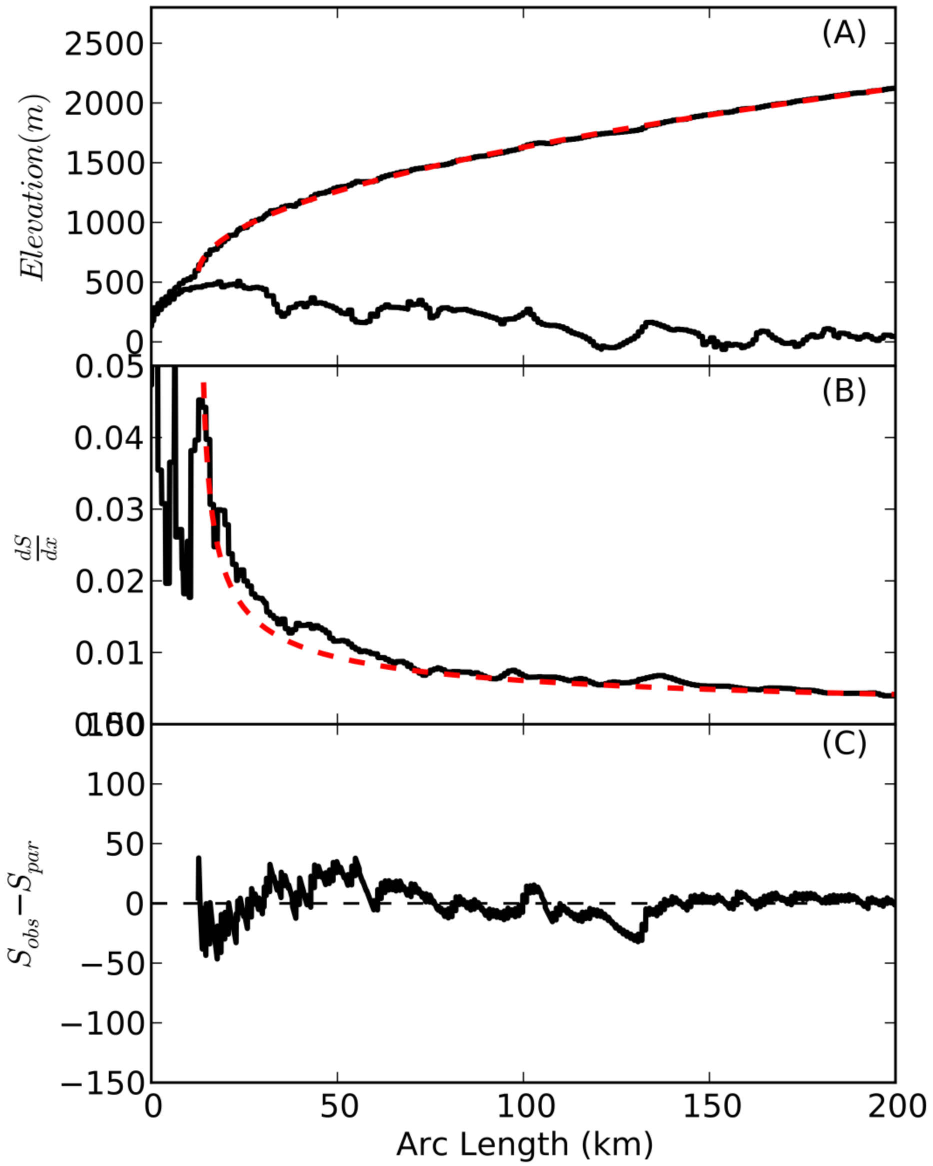

Figure S5: Same as Figure S2, but for profile S5.

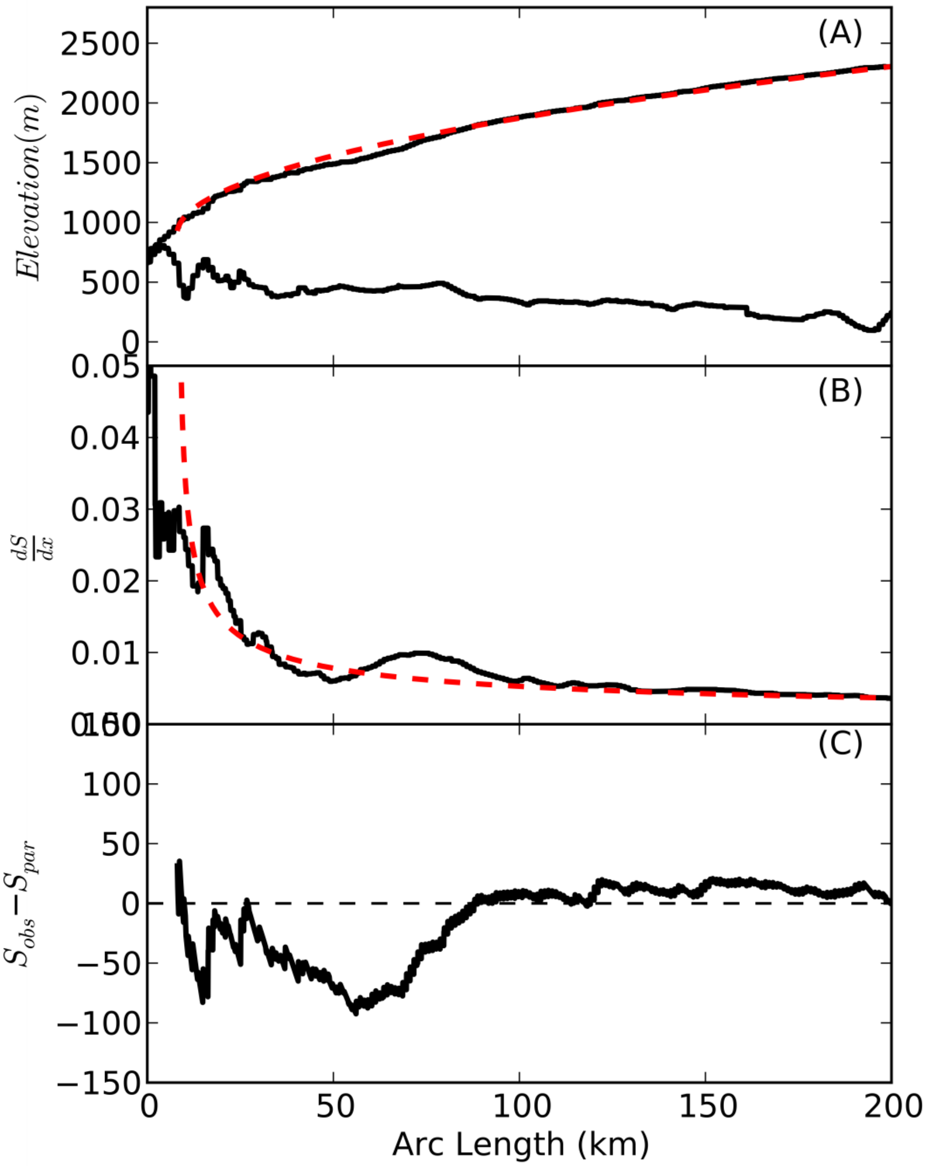

Figure S6: Same as Figure S2, but for profile S6.

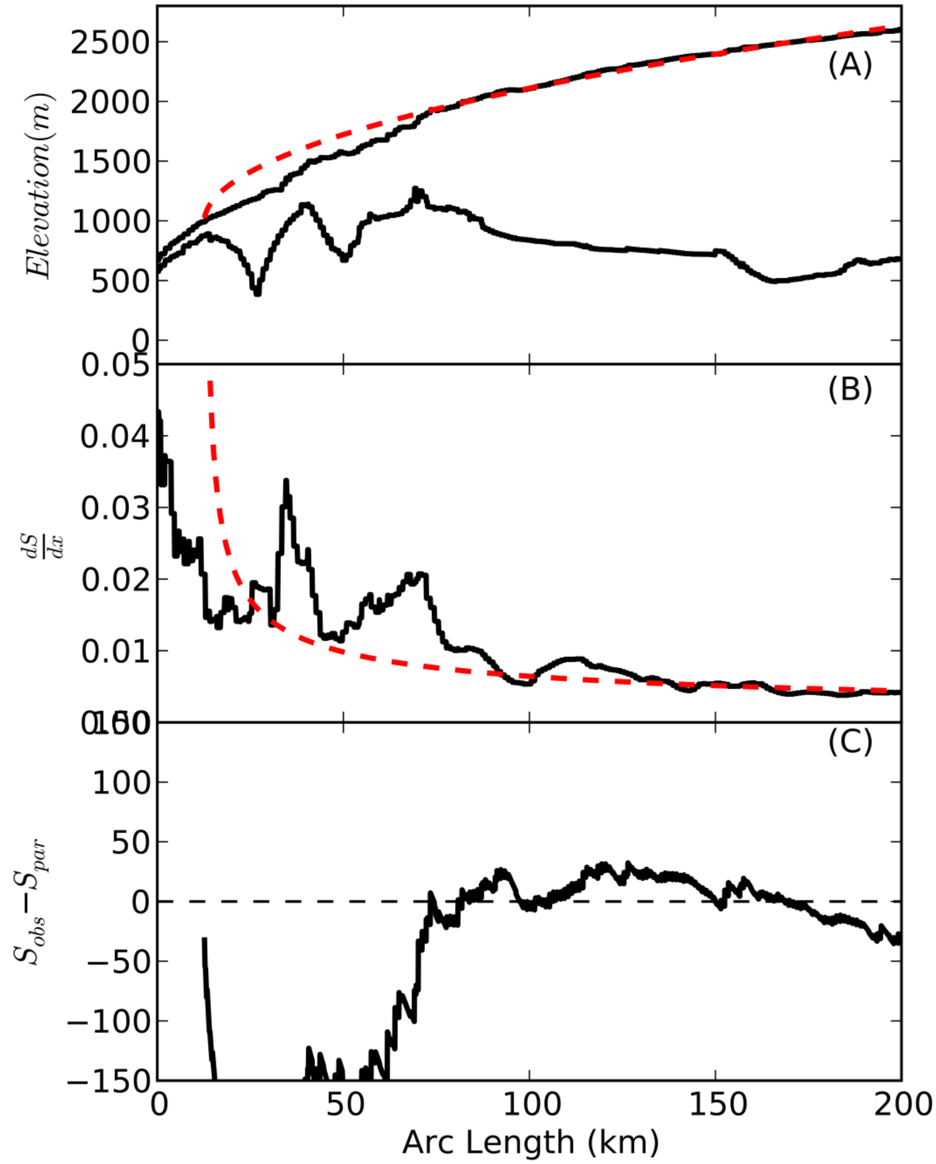

Figure S7: Same as Figure S6, but for profile S7.

APPENDIX A

BOREHOLE IMPULSE TEST EXPERIMENTS

Introduction

This chapter presents results and discussion from hydraulic impulse tests performed in boreholes drilled on the GrIS. Impulse tests were conducted to satisfy four scientific objectives pertinent to building a conceptual model of the GrIS subglacial hydrologic system:

1) Assess hydrologic connectivity along the ice sheet bed at small (hole-to-hole) spatial scale.
2) Investigate the hydraulic capacity of the basal system and time/space variability there-in.
3) Elucidate processes by which the basal hydrologic system accommodates flux perturbations.
4) Identify englacial water transport pathways.

In summary, significant spatial heterogeneity at the site scale (10s of m) was evident in test responses across all drilling sites. These dynamics were manifested in differential connectivity between boreholes in response to testing and variable capacity to accommodate flux perturbations at the ice sheet bed. This consistent heterogeneity suggests that water flow is concentrated in discrete elements along the ice sheet bed as opposed to flow through a widespread sediment layer. Rapid transient effects in response to continued perturbation during testing show that subglacial drainage elements with a reduced hydraulic capacity can rapidly evolve to accommodate variations in flow along the bed. The time scales for such evolution preclude enlargement of existing features by meltback of the overlying ice roof. Instead, rapid readjustment of local drainage elements may take place through mechanical processes. This enlargement of features along the bed enhances flow capacity, facilitates connection with adjacent regions of the basal hydrologic system, and may temporarily increase the fraction of bed in contact with basal water. In this way active recovery and a drop in basal pressure can accompany basal flow perturbations in the absence of a dominant melting component.

Methods

Borehole impulse tests perturb the basal hydrologic system by artificially raising the borehole water level. Three types of impulse tests were performed in boreholes drilled to the bed during the three field seasons, each of which differs in magnitude and duration:

1) Drilling breakthrough tests: Borehole drilling results in a hole which is water-filled to the surface during drilling and introduces a short duration, high magnitude (11% above overburden pressure) impulse to the basal system upon intersection. Drilling breakthrough tests measure the borehole water level in response to initial intersection with the basal system.
2) Slug tests: Slug tests are repeatable, low magnitude, short duration impulse tests in which a set volume of water is rapidly injected into the borehole and the subsequent water level recovery is documented.
3) Injection tests: Injection tests are long duration impulse tests in which water is pumped into the test hole at a continuous rate for a set period of time.

In this section we describe the instrumentation necessary to carry out such tests and provide methodology for experiment conduction.

Instrumentation

Borehole water levels were measured using pressure transducers emplaced at specified depths in boreholes. Voltage output by transducers was converted to meters of water above the sensor following field calibrations described below. If necessary, depth to water was calculated by subtracting the sensor water level output from the depth of the sensor below the ice surface, which was measured by meter marks on the transducer cable.

In 2010, Omega PX26-015GV pressure transducers with a pressure range of 0-15 pounds per square inch (psi), equivalent to 0-10.54 m of water above the pressure transducer, were used in all impulse experiments. In 2011, Omega PX209-060GI pressure transducers with a pressure range of 0-60 psi (0-42.18 m of water equivalent above the pressure transducer) were used in impulse experiments. The same 0-60 psi pressure transducers were used in 2012, with one additional 0-200 psi pressure transducer used for the large magnitude (>100 m) water level changes during drilling breakthrough tests. Pressure transducers logged voltage output in the 0 – 2000 mV range to a Campbell CR-10X datalogger at 4 digit precision, thus the lowest possible output resolution was 1 mV. This corresponds to approximately 0.05% of the pressure transducer output range, resulting in lowest end-member water level resolutions of 0.005, 0.02, and 0.07 m for the 15, 60, and 200 psi pressure transducers respectively. Depending on the anticipated time before data download, pressure transducers logged data at either 1 second or 2 second intervals. All pressure transducers were calibrated in the field using a 4 – 6 point calibration by lowering sensors to known depths below the water surface, and measuring voltage for one minute at each depth. Transducers were kept cold to reduce erroneous fluctuations arising from thermal equilibration.

Pressure transducers were soldered to the ends of 250 m lengths of Cat-5 cable, which was wired to the CR-10X datalogger at the ice surface. Cat-5 cable was manually marked at 1 m increments to facilitate depth to water calculations described above. To ensure a weather proof connection, the pressure transducer and solder joint were housed in PVC pipe and potted in clear epoxy.

When conditions permitted, water levels were measured in multiple boreholes during impulse experiments. This was achievable in shallow holes near the margin which remained open for a number of days. However, rapid borehole closure in cold ice at deep sites generally precluded measurement in multiple holes. All pressure transducers output to a central data logger, eliminating timing offsets.

Drill Breakthrough Tests

During drilling pressure transducers were placed in the borehole to monitor changes in water level occurring from intersection with englacial features and the basal hydrologic system. Water level changes before the drill reached the ice sheet bed were interpreted to result from intersection with an englacial hydrologic feature. Thus, identification of hydrologic transport or storage features in englacial ice required that water level monitoring persist through the entire drilling process.

Pumping Tests

A set discharge was injected in to a test hole during pumping tests by pumping water from nearby surface streams. This was achieved using a single sump pump or combination of pumps in parallel. Injection discharge was measured prior to and after testing by measuring the time to fill a series of 5 gallon buckets. Discharge varied between 1.26×10^{-3} – 4.98×10^{-3} m^3/s between tests but was consistent in pre- and post-test measurements. Borehole water levels were measured prior to testing for as long as possible (but at least 10 minutes) to determine background trends.

Slug Tests

Borehole slug tests were performed by rapid injection of a set volume of water in to the borehole. Test volumes were typically 150 – 170 liters (L), although some tests were performed using a smaller 75 L volume to test borehole response to perturbations of varying magnitude. The injection method of rapidly pouring water in to the hole from the surface took fewer than 10 seconds. As with pumping tests, background water levels were measured prior to testing.

Challenges

Temporary instrument installation for impulse testing was complicated by the propensity for sensors to freeze to borehole sidewalls. While measures were taken to limit sensor freeze-in, some data loss occurred as a result of water levels dropping below the level of sensor placement after freezing.

In addition to sensor freezing, a significant worry in performing tests was the tangling of multiple cables in a single borehole. This concern guided the methodology of slug and pumping tests. Such tests are commonly performed by submergence of a sealed cylinder in the case of slug tests, and by extracting water from the borehole in the case of pumping tests. However, these methods were logistically unfeasible in the field.

Results

Over the course of the three field seasons, 41 slug tests, 10 pumping tests, and 23 drilling breakthrough tests were conducted at the margin, interior, and interior trough sites. Data set summaries are presented in Tables A-1, A-2, and A-3 for drilling breakthrough, pumping, and slug tests respectively. Below, results for each of the three impulse test types are reported. The chapter concludes with a brief discussion synthesizing the data.

Drilling Breakthrough Tests

At the ice sheet margin six of 13 holes showed a water level decline when the bed was reached. Water levels declined by as much as 25% of ice overburden pressure (head drop of 32.6 m) in response to bed intersection. Decay times in breakthrough tests at the margin were long, taking up to 2 hours for complete drawdown. In contrast, all boreholes drilled in the inland settings showed a water level drop when the drill intersected the bed. The magnitude and rate of water level decline in boreholes varied between holes and sites. In the inland sites, water levels dropped to levels corresponding to 92 – 96.5% of ice overburden pressure (55 – 124 m). Drilling breakthrough responses in the inland trough site also showed water level drops ranging from 52 – 72 m, but in this thicker ice the borehole water level stabilized near or above ice overburden pressures. Drawdown times in the inland setting were much more rapid than the margin counterpart. The longest response time was 18 minutes, and water levels drew down in an as little 2 minutes before reaching new equilibrium. Assuming a constant borehole radius of 0.11 m, the subglacial system was able to accommodate up to 4.7 m^3 of water in response to drawdown during a breakthrough event. Peak discharge rates during drawdown reached 0.08 m^3/s.

The spatial variability measured during drilling breakthrough events suggests that the borehole water introduced during intersection with the bed is accommodated not by large scale radial flow, but by discrete drainage elements within the basal network. For example, while drilling hole GL11-1C, water levels in holes GL11-1A and GL11-1B were monitored. In response to intersection with the basal system the water level in GL11-1C drew down 75.4 m over the course of one minute, establishing an equilibrium at ~92% of overburden pressure (Figure A-1). Coincident with this large impulse, the water level 27 m away in GL11-1B rose by ~0.77 m, and exhibited damped oscillations as it recovered to equilibrium. Hole GL11-1A, located 29 m from GL11-1C, showed no response.

Borehole connection with englacial hydrologic features was observed in four boreholes, manifested as water level drops in the drill hole prior to reaching the ice sheet bed. Englacial feature intersection was limited to holes at the ice sheet margin. Figure A-2 shows borehole water level behavior during drilling GL10-2C. Three separate intersection events at elevations of 485, 483, and 472 m (corresponding to 79, 81, and 92 m below the ice surface) occurred as evidenced by sharp water level declines. The borehole water level stabilized at 5 m below the surface prior to dropping again when the drill intersected the ice sheet bed, suggesting that at least one of the englacial connections was an active hydrologic pathway. In other instances, intersection of englacial features in the drill hole induced a water level response in an adjacent borehole, indicating that these englacial features are not isolated entities. The presence of englacial hydrologic features provides an additional dimension to the ice sheet hydrologic system. In boreholes which exhibit an englacial connection, impulse test responses are a convolution of water transport through the subglacial drainage system as well as through an englacial fracture network. Drilling test results show that impulse tests in boreholes drilled away from the ice sheet margin are uncomplicated by englacial fracture flow. This does not necessarily preclude the existence of such englacial flow features, but we note that the persistence of an extensive englacial fracture network in the ice sheet interior is made difficult by cold englacial temperatures.

Pumping Tests

Two general water level type curves were observed in response to pumping in boreholes. In instances where the hydraulic capacity of the basal system was sufficient to accommodate the pumping perturbation, the borehole response was minor. Water levels rose slightly (less than 2 m) in response to pumping, reaching a plateau until pumping was terminated. This type response is displayed in a pumping test performed in hole GL12-2B (Figure A-3). In response to a pumping perturbation of 3.26×10^{-3} m^3/s, borehole water levels rose 0.8 m and quickly plateaued after less than 2 minutes of pumping. The water level remained approximately static until pumping was terminated after 24 minutes.

In contrast, an alternate type curve displayed a larger magnitude water level rise in response to pumping. This rise in borehole water level slowly plateaued and began to recover while pumping continued. The rate of water level recovery was consistently slower than the initial rise, resulting in an asymmetric rise and fall during pumping. In some instances continued water level recovery resulted in borehole water levels dropping below the pre-test level while pumping was maintained. This is exemplified in a pumping test performed in borehole GL11-1A (Figure A-3). In response to a pumping rate of

1.38×10^{-3} m^3/s, the borehole water level rose 5 m over the initial 4 minutes. The water level then plateaued and declined for the remaining 65 minutes of the test. When pumping was terminated, the water level had dropped over 12.5 m below the pre-test level.

Consistency in borehole responses was observed, as both type curves described above were measured in pumping tests performed at the inland and inland trough sites. As with drill breakthrough test responses, significant spatial variability was documented at the site scale. At both the inland and inland trough sites, boreholes less than 30 m apart showed both type responses. Heterogenous connections between holes were also evident in tests, as long term pumping did not guarantee the establishment of connections with adjacent boreholes.

Slug Tests

Three general types of borehole water level behavior were observed in response to slug testing:

1) Overdamped water level response characterized by a long, gradual water level decay towards equilibrium following injection.
2) Underdamped water level response characterized by oscillatory water level behavior about the pre-test water level.
3) Hybrid type response characterized by oscillatory water level behavior imprinted over a slow, overdamped recovery.

Examples of the three type responses are presented in Figure A-4. Of the 14 different boreholes which received slug tests across the three study regions, four boreholes showed consistent overdamped responses, five holes responded in an underdamped manner, and five holes displayed hybrid type behavior. All type responses were measured at each of the three field regions. The period of oscillation in underdamped tests increased through the three study regions, generally following the square root of the ice thickness. In contrast to the rapid recovery of oscillating water levels, recovery times in boreholes which responded to slug tests in an overdamped manner commonly exceeded one hour. Over these long time scales, the recovery curve was complicated by background water level changes which could exceed 10 m.

Slug tests in different boreholes at the same site location showed significant spatial variability at the site scale (10s of m). It was not uncommon to measure both underdamped and overdamped responses to slug tests in different boreholes less than 30 m apart. This behavior was consistent in both the margin, inland, and inland trough regions. Coincidentally, all boreholes which displayed minor water level rise in pumping tests also responded to slug perturbations in an underdamped fashion. Further, boreholes which exhibited the larger magnitude, asymmetric water level response to pumping behaved in an overdamped manner when perturbed with a slug test.

Repeat testing in boreholes suggested that while a complete mode shift from underdamped to overdamped (or vice versa) was unlikely, the response behavior was prone to adjustment depending on the background water level at time of testing. This temporal variability is highlighted by three slug tests performed over a four day period in borehole GL11-1A (Figure A-5). Slug test S1 performed in the borehole, shortly after drilling, showed isolated behavior; 100 minutes after injection the water level recovered by less than 25% of the initial slug magnitude (~0.85 m). Two days later, a second slug test S2 in the same borehole showed a rapid recovery in response to the slug. The water level recovered 100% of the initial slug magnitude and continued to drop below the expected natural water level. In a third slug test S3 the following day, water level behavior in the borehole showed a gradual recovery which followed the expected background trend, suggesting an inability of the system to accommodate the injected water package. Background water level at the time of test S2 was 802 m, over 2.5 m greater than test S3, and 15 m greater than test S1. The rapid recovery in test S2 may likely have been facilitated by enhanced connectivity during the period of higher water level which approached overburden level (estimated to range from 795.5 – 808.5 m).

Synthesis

The spatial variability among all three types of impulse tests conducted supports the conceptual model that at the local scale water may flow largely through discrete elements in the basal hydrologic network as opposed to more diffusive, laminar flow through a homogenous till layer. Boreholes <30 m apart commonly exhibited opposing type responses to slug testing. Large magnitude pressure pulses associated with drilling breakthrough tests exhibited the capacity to influence water levels in some adjacent boreholes, but not others. Long duration pumping tests in boreholes showed heterogeneous connectivity to adjacent boreholes. This variability was generally consistent across all drilling sites.

The dynamic nature of connections and rapidly changing background conditions limit the utility of standard hydrogeological transmissivity calculations. Such an analysis assumes steady background conditions, radial and laminar flow, and a homogenous, isotropic medium. These assumptions are all violated on the ice sheet domain. Further, rapid accommodation of pumping perturbations and active recovery during pumping suggests that the system is driven by processes which are not accounted for in standard analytical techniques. This rapid transience means the effective transmissivity could vary by orders of magnitude over very short time scales (minutes in the case of pumping tests). As a result of these violations and additional processes, transmissivity values would be subject to considerable uncertainty and would only be representative of a small spatial area for an instant in time. While calculation of transmissivity is of limited utility, borehole response to pumping provides information regarding the flow capacity of basal drainage elements and the processes by which perturbations are accommodated. The minor borehole response to pumping in boreholes GL11-1C and GL12-2B suggests that the background flow through the system to which these holes are connected is likely to be large compared to the injection rate ($1.38 – 3.26\text{x}10^{-3}$ m^3/s). This is also supported by the rapidly recovering underdamped slug test responses in these holes.

Adjacent to transmissive features, other boreholes showed resistant connections with limited capacity to transmit water as evidenced by slow draining overdamped slug test responses and gradual water level drops following drilling breakthrough. Yet, the hydrologic efficiency of the drainage elements to which these boreholes are connected is quite transient. In response to pumping perturbation, the efficiency of these drainage elements is capable of evolving over short time scales (5 – 30 minutes) to accommodate the injection and more, as evidenced by the active recovery while pumping is continued. This evolution is unable to be explained solely by enlargement of existing connections from meltback of the overlying ice roof. Presumably, a mechanical component may be invoked to increase connectivity at the bed and facilitate increased basal flux. This is supported by repeated slug tests, which showed an enhanced ability to accommodate the perturbation when background water levels were closest to overburden levels. In this setting, the additional head perturbation induced by the slug may act to increase connectivity to other regions of the bed by mechanical separation, facilitating faster water level recovery. In the natural setting this provides a means of short term expansion of the subglacial network and increased water coverage at the bed during periods when flux overwhelms the existing subglacial system.

Near the ice sheet margin drilling breakthrough tests and borehole video (not presented here) confirm the presence of englacial features which may act as water storage reservoirs or active transport pathways. While inland boreholes provide a limited sample size, and surface-to-bed water routing moulins are prevalent throughout the ablation zone, no evidence for an extensive englacial fracture network was evident in drill breakthrough tests away from the margin.

Figures

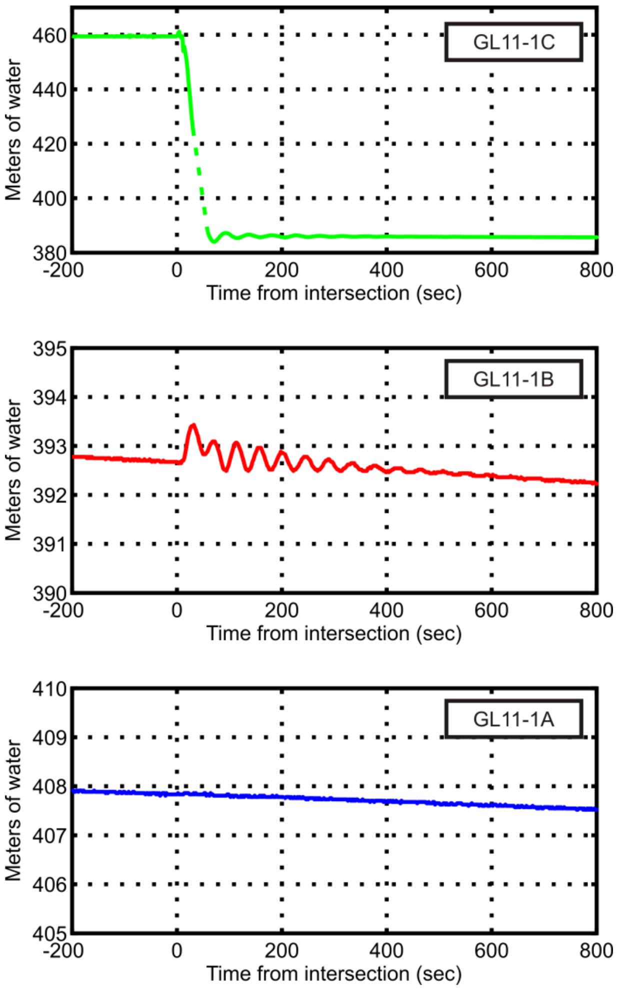

Figure A-1: Drill breakthrough response in borehole GL11-1C. In response to the water level drop in GL11-1C, adjacent hole GL11-1B showed a water level rise of ~0.77 m and exhibited damped oscillations towards equilibrium. In contrast, hole GL11-1A, which was located 29 m from the drill hole, showed no response. Note the difference in y-axes between subplots.

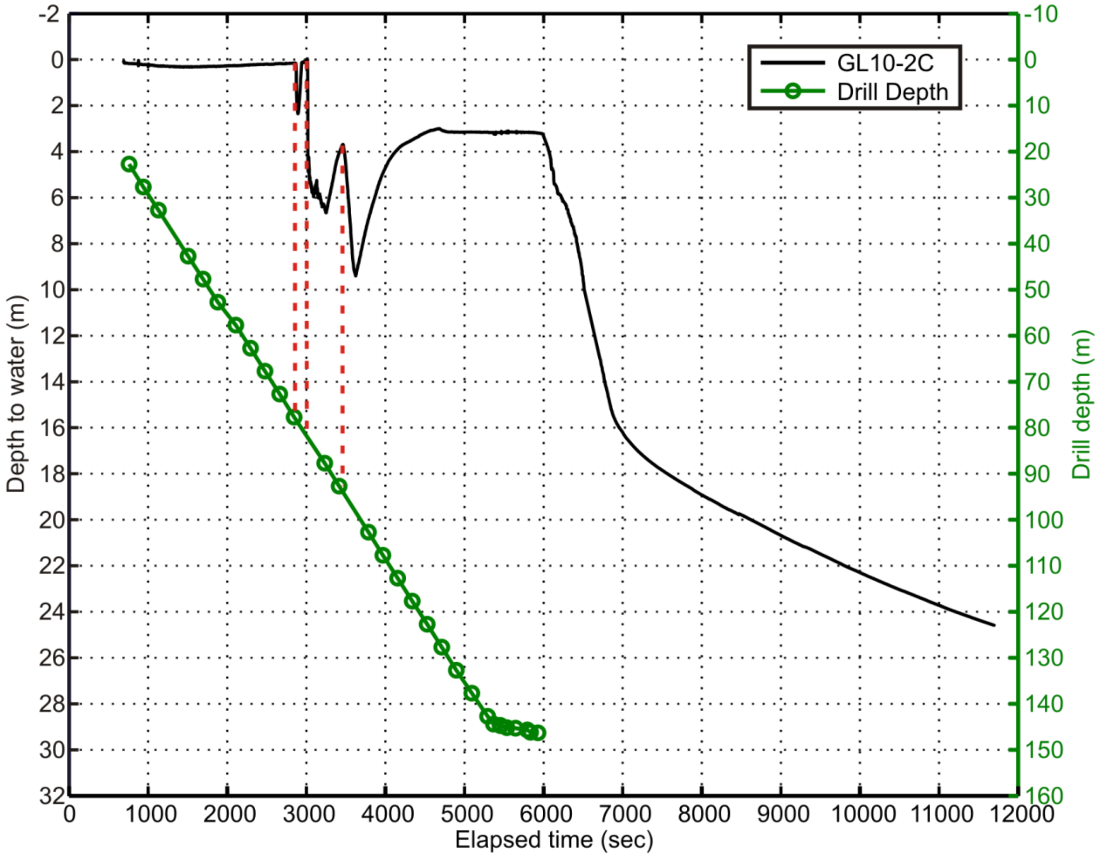

Figure A-2: Drilling breakthrough test in borehole GL10-2C. Black line represents the depth to water in the drill hole, and corresponds to the left-hand y-axis. Green line corresponds to the depth of the drill tip, measured at discrete times as represented by green circles. The drill depth corresponds to the right-hand y-axis. At depths of 79, 81, and 92 m below the ice surface, the drill tip penetrated an englacial hydrologic feature, triggering a water level drop. Englacial feature intersection events are denoted by red, vertical dashed lines. The drill penetrated the basal hydrologic network at a depth of 146.3 m, prompting a long water level decline which continued after the measurements were terminated.

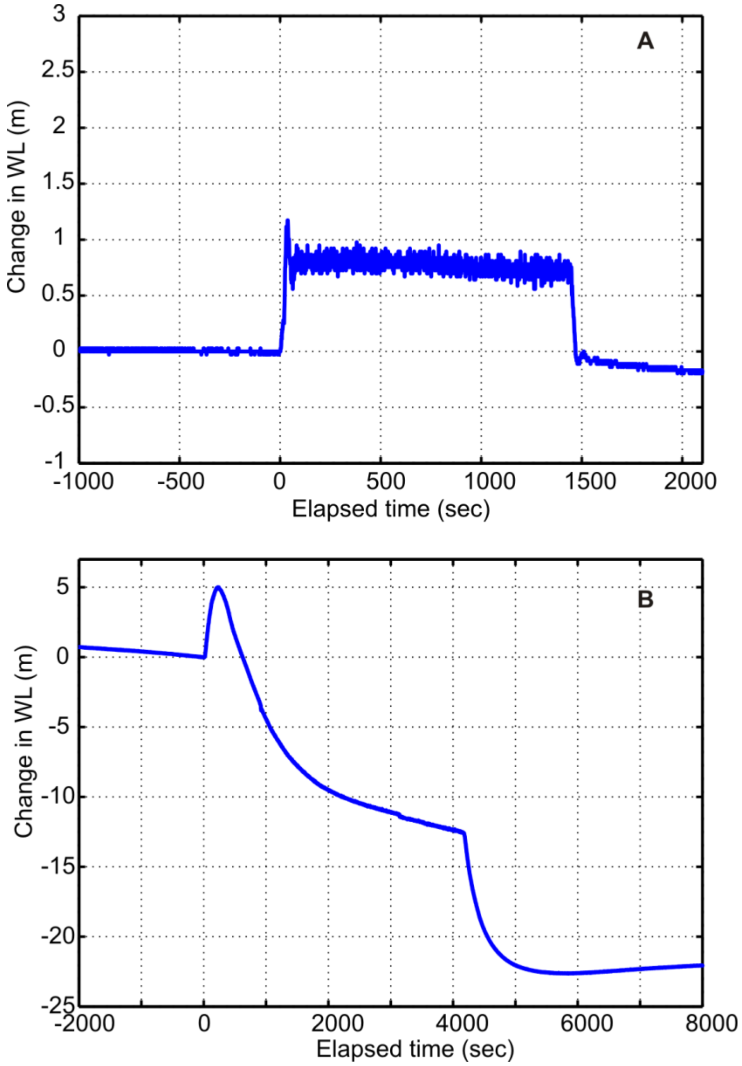

Figure A-3: Pumping test type responses. A) Efficient type response in which borehole water level showed minor rise in water level and stabilization in response to pumping. In this example, borehole GL12-2B received 3.26x10^{-3} m^{3} s^{-1}. Pumping was initiated at time t = 0 s and continued until time t = 1440 s. B) Asymmetric response in which water level exhibited an initially rapid rise, system transmissivity enhancement a forced water level peak, and active recovery while pumping was continued. In this example, borehole GL11-1A received 1.38x10^{-3} m^{3} s^{-1}. Pumping began at time t = 0 s, and continued until t = 4200 s. Note the difference in x- and y-axes between subplots.

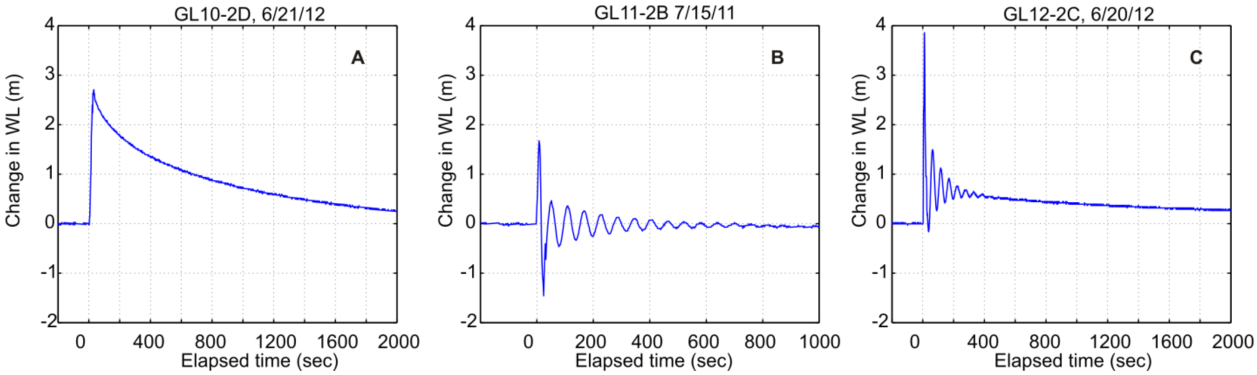

Figure A-4: Slug test type responses indicating (A) overdamped, (B), underdamped, and (C) hybrid type responses. Test borehole and date of slug test are listed above the plots. Note the difference in x-axis.

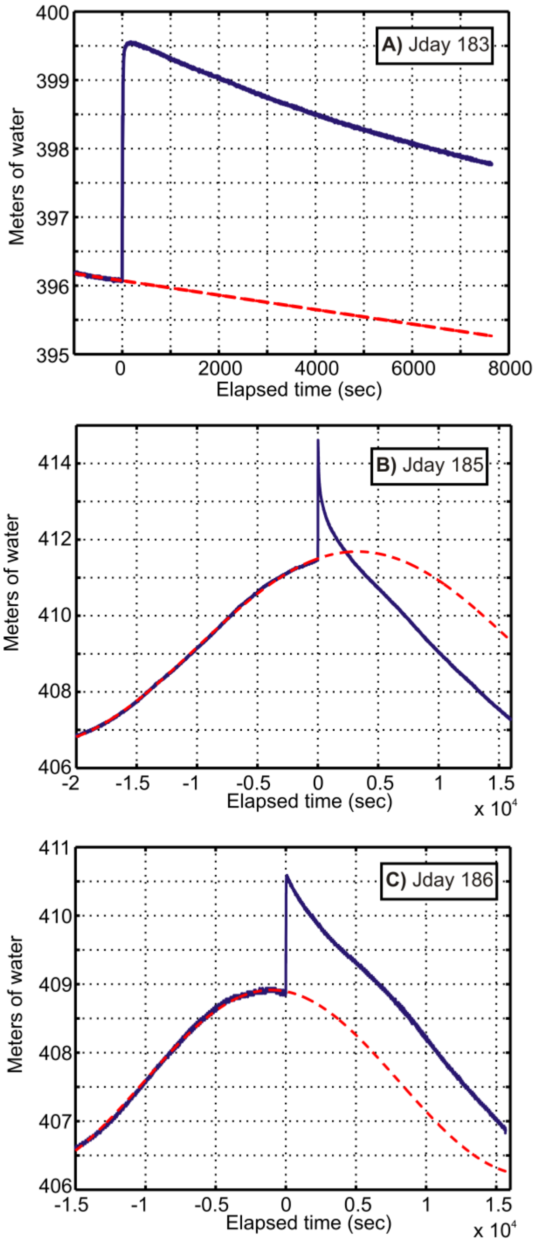

Figure A-5: Time series of slug tests performed in borehole GL11-1A in 2011 on days of year 183, 185, 186. Expected background water level behavior in each subplot is fit to pre-test water levels using a first order fourier fit. The first slug test (A) was performed shortly after drilling was completed, reducing pre-test water level monitoring time. Pre-test water level was highest prior to the slug test performed on day of year (B). Rapid water level recovery followed perturbation and continued beyond expected background trends. The third slug test performed on day of year 186 exhibited behavior similar to that on day 183 (C). Water levels generally following expected background trends indicate an inability of the system to accommodate the added perturbation.

Tables:

Drill Hole	Date	Hole depth (m)	Measured WL decline (m)	Final WL (m)	Final WL (% overburden)	WL decline duration (sec)	Oscillation period (sec)
GL10-1A	6/12/2010	98	0	98	109.9	-	-
GL10-1B	6/13/2010	92.5	0	92.5	109.9	-	-
GL10-1C	6/14/2010	91	0	91	109.9	-	-
GL10-1D	6/14/2010	98.5	15.27	83.23	92.9	>1385	-
GL10-1E	6/16/2010	91.9	9.07	82.83	99.0	316	-
GL10-1F	6/17/2010	102	0	102	109.9	-	-
GL10-2A	6/20/2010	144	0	144	109.9	-	-
GL10-2B	6/21/2010	148.7	24.5	124.2	91.8	>6460	-
GL10-2C	6/23/2010	146.3	21.39	124.91	93.8	>5708	-
GL10-2D	6/23/2010	145.6	24.54	121.06	91.4	>2458	-
GL10-2E	6/25/2010	148.7	32.63	116.07	85.8	7139	-
GL10-3A	6/30/2010	577.3**	-	-	-	-	-
GL10-3B	7/2/2010	700.4**	-	-	-	-	-
GL11-1A	7/2/2011	457	55.6	401.4	96.5	1090	-
GL11-1B	7/4/2011	466	71.9	394.1	92.9	<89	-
GL11-1C	7/6/2011	460	75.4	384.6	91.9	70	45.1
GL11-2A	7/13/2011	254.5**	-	-	-	-	-
GL11-2B	7/14/2011	821	104.7	716.3	95.9	<180	57.8
GL11-2C	7/17/2011	816	124.2	691.8	93.2	245	-
GL11-2D	7/18/2011	815	>40	-	-	-	-
GL12-1A	6/7/2012	116.6	0	116.6	109.9	-	-
GL12-1B	6/7/2012	114.5	0	114.5	109.9	-	-
GL12-2A	6/13/2012	700	72	628	98.6	1040	-
GL12-2B	6/15/2012	715	>40	-	-	-	-
GL12-2C	6/17/2012	695	52.8	642.2	101.5	320	-
GL12-2D	6/20/2012	701	52.1	648.9	101.7	950	-

Table A-1: Drilling breakthrough test results. Asterisks (**) indicate boreholes which were terminated before the ice sheet bed. In boreholes GL11-2D and GL12-2B borehole water level dropped below the sensor which was frozen to the borehole sidewall. Slow draining boreholes (GL10-1D, GL10-2B, GL10-2C, GL10-2D) showed continuing water level decline when the pressure transducer was removed for basal sampling.

			Initial water level				Max head rise		
Test #	Test hole	Ice thickness (m)	Depth to water (m)	% overburden	Pumping rate ($m^3 s^{-1}$)	Duration (min)	(m)	% overburden	Response type
1	GL10-2B	148.7	31.8	0.87	1.26E-03	58	24.5	18.31	II
2	GL10-2B	148.7	34.4	0.85	1.33E-03	106	16.6	12.40	II
3	GL11-1A	457.5	48.4	0.99	1.38E-03	70	5.1	1.24	II
4	GL11-1C	459.5	76.5	0.93	1.38E-03	70	0.6	0.15	I
5	GL12-2B	715	69.7	1.00	1.69E-03	20	0.4	0.06	I
6	GL12-2B	715	69.7	1.00	3.26E-03	24	1.2	0.19	I
7	GL12-2C	695	49.5	1.03	1.89E-03	153	7.2	1.15	II
8	GL12-2C	695	58.0	1.02	4.98E-03	22	10.7	1.71	II
9	GL12-2D	701	54.1	1.03	4.29E-03	635	12.7	2.01	II
10	GL12-2D	701	81.7	0.98	4.98E-03	648	36.3	5.75	II

Table A-2: Summary of pumping test results. Response type I corresponds to small magnitude head rise and water level stabilization in response to pumping. Response type II corresponds to asymmetric type response with larger magnitude head rise and active recovery during pumping.

Test #	Test hole	Injection volume (l)	Response type	Day	Avg period of oscillation (sec)	Adjacent hole response
1	GL10-1D	132	UD/OD	6/14/2010	15.37	-
2	GL10-1D	151	UD/OD	6/15/2010	12.67	-
3	GL10-1C	132	OD	6/15/2010	-	-
4	GL10-1C	132	OD	6/15/2010	-	-
5	GL10-1D	151	OD	6/16/2010	-	-
6	GL10-1E	151	UD	6/16/2010	31.33	GL10-1D
7	GL10-1E	151	UD/OD	6/17/2010	14.38	GL10-1D
8	GL10-1D	151	UD	6/17/2010	23.34	GL10-1E
9	GL10-1E	151	UD	6/17/2010	25.34	GL10-1D
10	GL10-1D	151	UD	6/18/2010	22	GL10-1E
11	GL10-1E	151	UD/OD	6/19/2010	-	GL10-1D
12	GL10-1D	151	UD/OD	6/19/2010	-	GL10-1E
13	GL10-2C	151	OD	6/23/2010	-	GL10-1D
14	GL10-2B	151	UD/OD	6/24/2010	24.32	GL10-2D, GL10-2C
15	GL10-2D	151	UD/OD	6/24/2010	24.27	GL10-2B, GL10-2C
16	GL10-2C	151	OD	6/24/2010	-	GL10-2B, GL10-2D
17	GL10-2C	151	OD	6/25/2010	-	GL10-2B, GL10-2D
18	GL10-2E	151	UD/OD	6/25/2010	24.31	GL10-2D, GL10-2C
19	GL10-2E	151	UD/OD	6/25/2010	23.93	GL10-2D, GL10-2C
20	GL10-2E	151	UD/OD	6/26/2010	24.04	GL10-2D, GL10-2C
21	GL10-2C	151	OD	6/27/2010	-	GL10-2E
22	GL11-1A	151	OD	7/2/2011	-	-
23	GL11-1A	151	OD	7/4/2011	-	-
24	GL11-1B	151	UD	7/4/2011	43.32	-
25	GL11-1B	151	UD	7/5/2011	44.14	-
26	GL11-1B	75	UD	7/5/2011	43.66	-
27	GL11-1B	75	UD	7/5/2011	45.03	-
28	GL11-1A	75	OD	7/5/2011	-	-
29	GL11-1B	151	UD	7/6/2011	38.04	-
30	GL11-1C	151	UD	7/8/2011	48.3	GL11-1B
31	GL11-2B	151	UD	7/15/2011	58.64	-
32	GL11-2B	151	UD	7/15/2011	55.83	-
33	GL11-2D	151	UD	7/18/2011	63.39	-
34	GL12-2B	170	UD	6/15/2012	54	-
35	GL12-2C	170	UD/OD	6/17/2012	42.9	-
36	GL12-2C	170	UD/OD	6/19/2012	47.6	-
37	GL12-2C	170	UD/OD	6/19/2012	48	-
38	GL12-2C	170	UD/OD	6/19/2012	47.9	-

39	GL12-2C	170	UD/OD	6/19/2012	47.8	-
40	GL12-2C	170	UD/OD	6/20/2012	53.4	-
41	GL12-2D	170	OD	6/21/2012	-	GL12-2C

Table A-3: Summary of slug test results. Response type UD = underdamped, OD = overdamped, and UD/OD = hybrid type response.